ALMA MATER STUDIORUM
UNIVERSITÀ DI BOLOGNA

MECHANICAL ENGINEERING BACHELOR THESIS

SHAPE MEMORY ALLOYS

Carlota Galindo Quintas

July 2016

Index

INTRODUCTION

In the past years, the huge advancements of science and technology have increased the demand of what are known as *smart* or *multifunctional* materials. These are lighter and stronger materials with special properties that provide further engineering functionalities. A subgroup of these multifunctional materials are the *active* materials, which exhibit sensing and actuation capabilities. Shape memory materials are a class of active materials, capable to convert a non-mechanical input, in this case a thermal field, into a mechanical output, working as actuators.

Within shape memory materials, we have *Shape Memory Alloys* (SMAs). SMAs have the ability to recover their original shape when the temperature is increased a certain level. During the shape recovery, they are able to develop large forces, fact that makes them exceptional actuators. Moreover, SMAs have a superelastic behavior when activating them at a certain temperature and they are capable to recover very large deformations. In addition, SMAs have demonstrated energy dissipation capabilities, very good corrosion resistance, hysteric damping and good fatigue resistance. SMAs cover a wide range of applications in several industrial sectors and fields: biomedical, aerospace, automotive, oil explotation, structural, etc.

The aim of this study is to experimentally test the thermomechanical properties of SMA spring actuators. The springs used are produced manually in the laboratory by applying specific heat treatments on a SmartFlex® wire. Further tests to analyse the different actuating properties of our spring are performed.

THEORETICAL FUNDAMENTALS OF SHAPE MEMORY ALLOYS

1. Working principle of SMAs

The funcionalities of shape memory alloys (SMAs) arise from the microstructural changes occurring when these materials are subjected to external non-mechanical inputs like magnetic or thermal fields. Thermally responsive SMAs consist of two phases, each with a different crystal structure and therefore different properties. These two phases are: a high temperature phase called *austenite* (A), and a low temperature phase called *martensite* (M). Austenite is generally cubic, while martensite can have a tetragonal, orthorhombic or monoclinic crystal structure. The transformation from one structure to the other, known as martensitic transformation, is reversible solid-solid and diffusionless as it is due to shear lattice distorsion (movement of atoms from their original position). Inside a single crystal, this process takes place along a specific plane which forms the interface between the austenitic and martensitic phases, called the *habit plane* or *lattice invariant plane*, as it does not rotate or deform during the transformation. The martensitic transformation can occur through two different mechanisms: slip or twinning. This second one is the most common mechanism in SMAs and consists on atoms moving through a fraction of an atomic space and results in a relative displacement of atoms that can cause a macroscopic shape change.

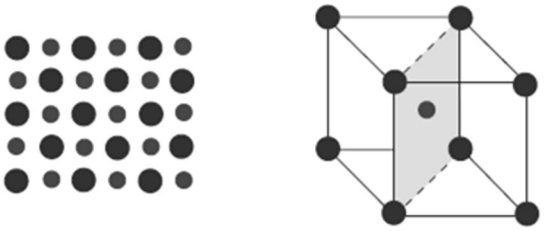

Fig. 1. Cubic crystal structure of austenite

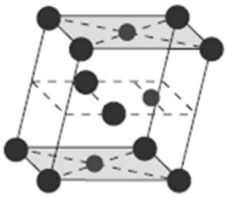

Fig. 2. Monoclinic crystal structure of martensite

Fig. 3. Twinned martensite on the left and detwinned martensite on the right [1]

Due to its non-cubic structure, each of the crystals of the martensitic phase can have a different orientation, called *variant*. Thus, there are "self-accomodated martensite variants" (also referred to as *twinned martensite* M^t) and "single variant martensite" (also referred to as *detwinned martensite* M^d), where a specific variant is dominant. Under no-load conditions, martensite in SMAs is self-accomodated. The reversible phase transformation from martensite to austenite and viceversa is the responsible of the unique behaviour of SMAs.

The process of transition from austenite to martensite (twinned) is named *forward transformation* and is due to cooling under free-stress conditions. Similarly, the phase transformation from martensite (twinned) to austenite is called *reverse transformation* and occurs when the material is heated in the absence on an applied load. There is no associated shape change in both processes. There exist four characteristic temperatures in these transitions. Under zero load, forward transformation starts at the *martensitic start temperature* (M_s) and finishes at the *martensitic finish temperature* (M_f); while reverse transformation begins at the *austenitic start temperature* (A_s) and ends when the material reaches the *austenitic finish temperature* (A_f).

In addition to austenite and martensite, in some cases an additional phase is present during cooling: the R-phase. This phase has a trigonal crystal structure and its presence depends on the composition of the alloy, the thermal history and the manufacturing process. Thus, in these cases, the forward transformation has two stages: transformation from austenite to R-phase and transformation from R-phase to martensite.

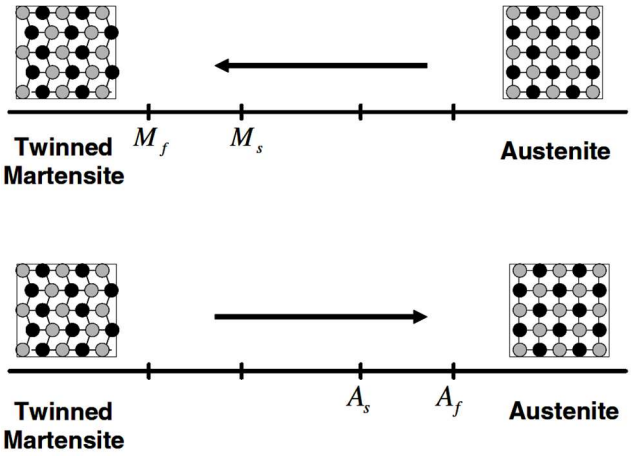

Fig. 4. Temperature-induced phase transformation of SMAs under zero-load [1]

If the material is subjected to a mechanical load at low temperature (in the twinned martensitic phase), detwinned martensite is obtained with the result of a macroscopic shape change. The deformed configuration remains when the load is released. Two characteristic stress levels can be observed in this process: the *detwinning start stress* σ_s, which is the minimum stress required to initiate detwinning, and the *detwinning finish stress* σ_f, level of stress at which detwinning is complete.

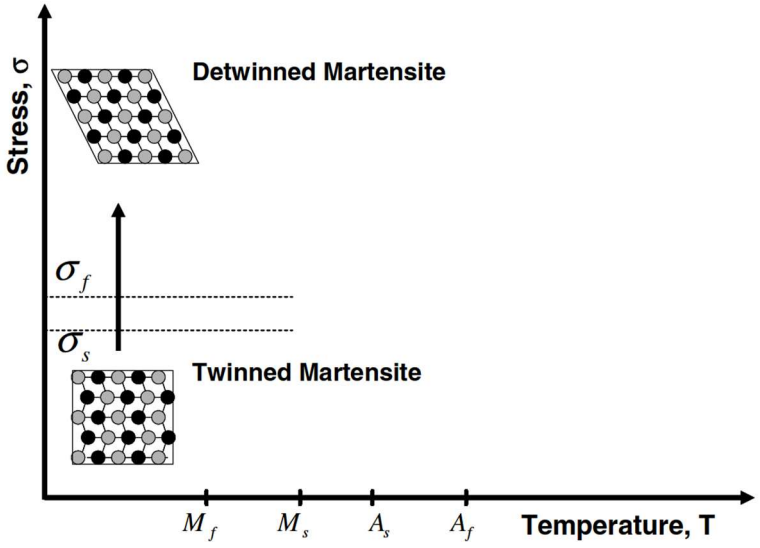

Fig. 5. Detwinning process of SMAs with an applied stress [1]

The temperature-induced phase transformation and the detwinning process are the basis to demonstrate two interesting phenomenon of SMAs: *Shape Memory Effect* (SME) and *Pseudoelastic Effect* or *Superelasticity* (SE).

1.1 Shape Memory Effect

As mentioned before, SMAs possess the ability to return to a predetermined shape when heated above their austenite finish temperature A_f. This capacity constitutes the principle of the Shape Memory Effect phenomenon. The process starts under zero-stress conditions having self-

accommodated or twinned martensite. If low levels of stress are applied, the martensitic variants favourably align themselves and the response obtained looks like a classic elastic deformation. With higher loads, the detwinning process begins resulting in macroscopic strains and shape changes (around 6-8% of strain). Once unloaded, the material does not completely return to its original state but there is some residual strain which cannot be recovered (around 4-6% of strain, depending on the level of stress reached). With heating above A_f, the detwinned martensite is transformed into stable austenitic phase which results in complete shape recovery. Finally, if the material is cooled below M_f under zero-load, austenite transforms back to twinned martensite.

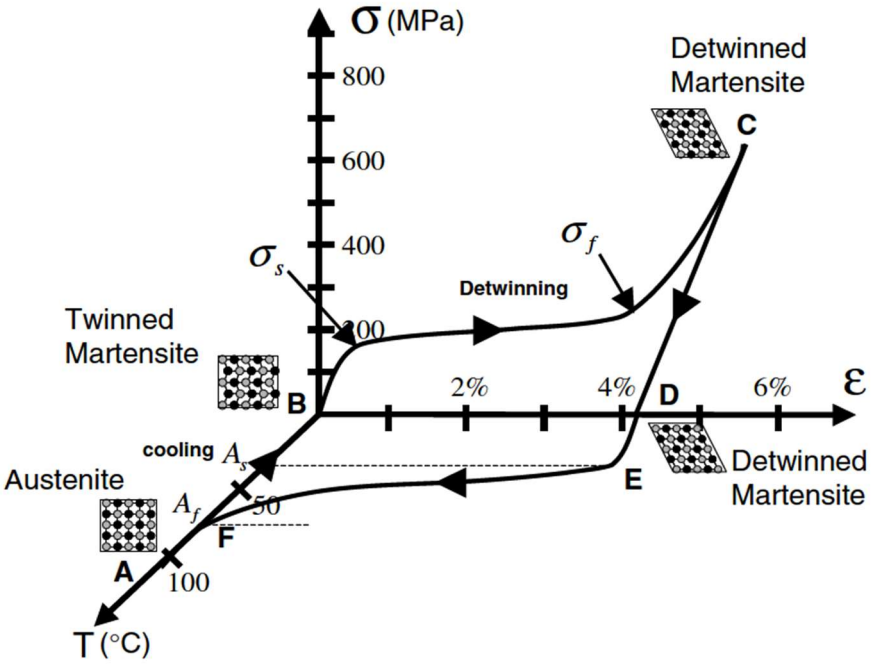

Fig. 6. Temperature-stress-strain chart of a typical NiTi SMA undergoing the SME [1]

An application of the SME effect phenomenon consists in a SMA working as an actuator. If a constant mechanical load greater than σ_s when cooling in the austenitic phase, a direct transformation to detwinned martensite is obtained, producing a shape change. If the load is maintained and the material is reheated above A_f, the original shape is recovered. The result is an actuating mechanism which is able to deliver a mechanical output, from a non-mechanical input (a raise in temperature).

It is possible to observe that the transformation temperatures strongly depend on the level of stress applied, in a way that they increase with increasing load. Consequently, the transformation regions “detwinned martensite to austenite”, and vice versa, have positive slope in the stress-temperature chart. Thus, the tranformation temperatures at a certain stress level σ, $\sigma > \sigma_s$, are named M_s^σ, M_f^σ, A_s^σ and A_f^σ.

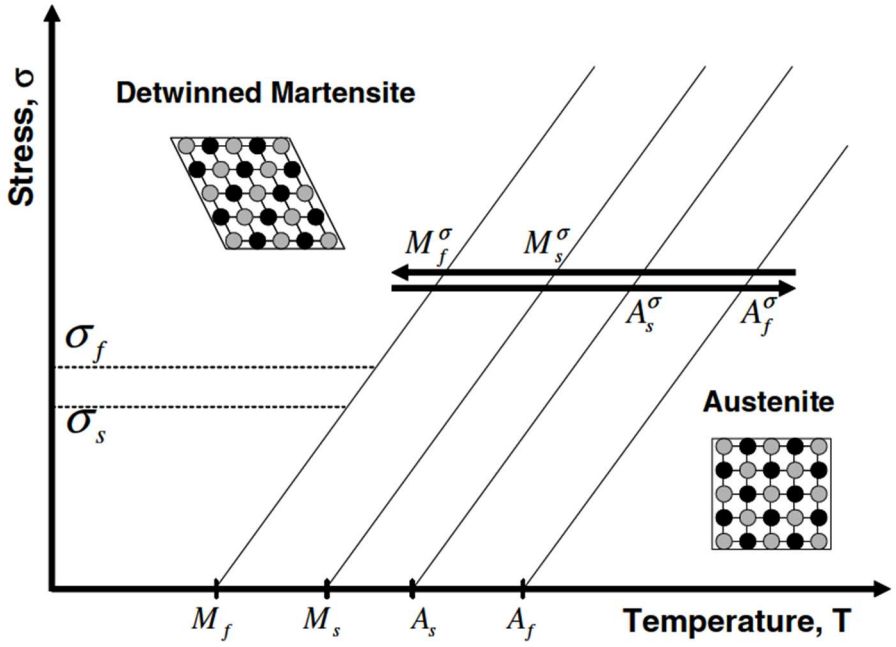

Fig. 7. SME in the presence of applied load [1]

1.2 Pseudoelasticity

Martensitic transformations in a SMA can also occur due to loading-unloading in the austenitic phase. If a sufficiently high mechanical load is applied to the material at a temperature above A_f, fully detwinned martensite is created from austenite and macroscopic levels of strain can be observed. When unloading, the SMA comes back to its original shape. This behavior is known as *pseudoelastic effect* or *superelasticity*. Thus, there exist four characteristic stress levels in this process: the stress levels at which the martensitic transformation initiates and completes during loading, σ^{M_s} and σ^{M_f}, and similarly, during unloading, the stress levels at which the austenitic transformation begins and ends, σ^{A_s} and σ^{A_f}. If the pseudoelasticity effect takes place at a temperature higher than M_s but below A_f, there is only partial shape recovery.

The thermomechanical loading path of the pseudoelastic effect starts by subjecting the material to moderate external loads at a temperature above A_f. The response looks like a classic elastic deformation of a metal. Upon higher loads, at some critical stress σ^{M_s}, begins to transform to detwinned martensite, commonly referred as *stress-induced martensite* (SIM), to differentiate it from the martensite formed by twinning in the SME. This transformation results in a macroscopic shape change of about 6-8% of strain. When the transformation is complete, continuing loading causes elastic deformation of the SIM and even higher loads may result in plastic deformation and some strain cannot be recovered. Upon unloading, the SIM comes back to a point where it is thermodynamically stable and as the load continues decreasing it starts to transform back to austenite. Similarly to the martensitic transformation, this last path is associated to large macroscopic shape changes (in this case, shortening). Finally, the elastic unloading of austenite occurs.

There are some noted features in a superelastic response (ASTM standards):

- Upper Plateau Stress (UPS): Stress at 3% of strain during loading of the material.

- Lower Plateau Stress (LPS): Stress at 2.5% of strain during unloading of the material after loading it to 6% of strain.
- Residual Elongation (El_r): The difference between strain levels at a stress of 7 MPa during loading and unloading.

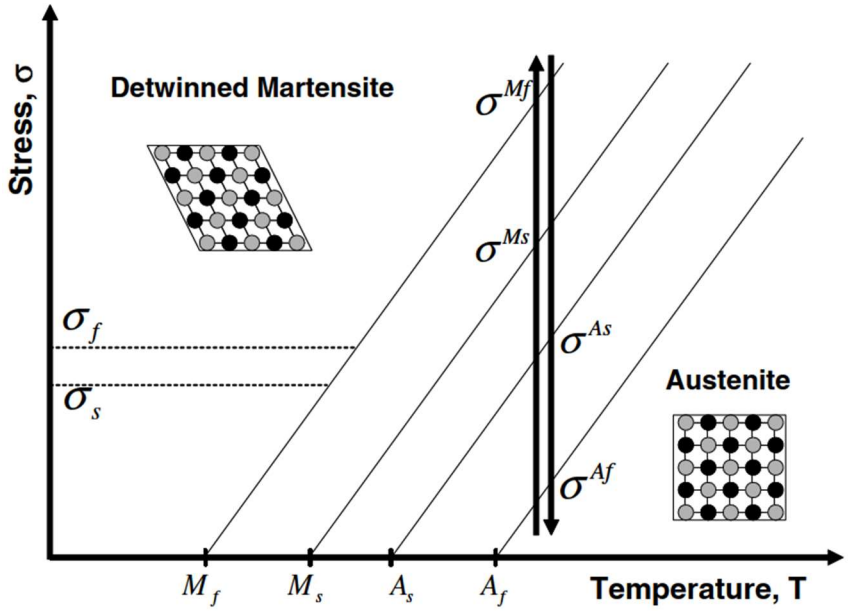

Fig. 8. A pseudoelastic loading path [1]

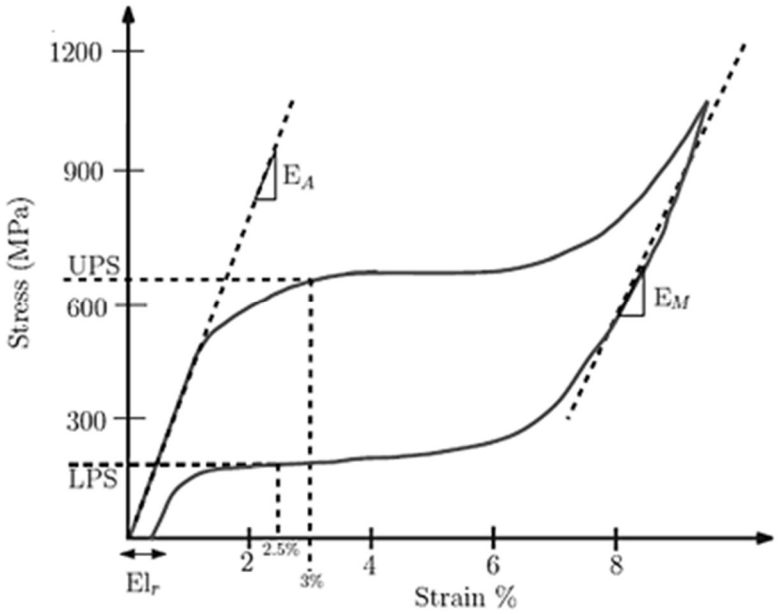

Fig. 9. Stress-strain chart of a superelastic response [1]

1.3 Cyclic behavior of SMAs

When a SMA is subjected to a cyclic thermal load it can exhibit repeateble shape changes under zero-load. This is known as the *two-way shape memory effect* (TWSME). The process of loading the material repeatedly following a cyclic thermomechanical loading path is named *training*. Training for a large number or cycles causes permanent changes in the microstructure. In a cyclic thermal loading, some small unrecoverable strain remains after each thermal cycle is completed. The additional permanent strain associated with each consecutive cycles begins to decrease until it practically ceases to further accumulate and, at this point, the hysteretic response of the material stabilizes. This strain is known as *saturation strain*.

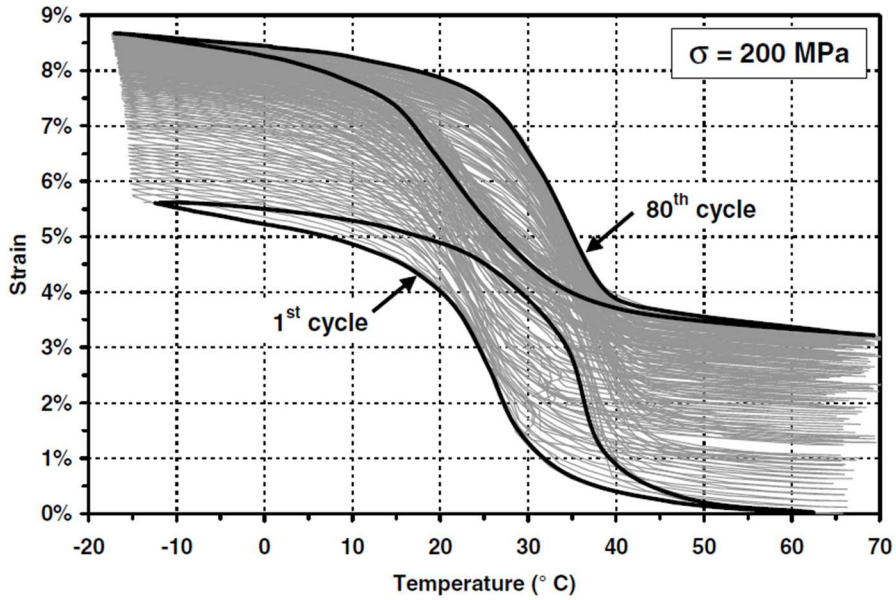

Fig. 10. Training at constant load of 200 MPa [1]

2. Manufacturing process of SMAs

The manufacturing process of SMA consists on several steps and all of them are crucial and have a large impact on the final properties of the desired product. Regarding the primary manufacturing techniques, casting or powder metallurgy processes can be used. In the case of NiTi SMAs, which would be our main objective, casting is the most popular technique with two principal methods: *Vacuum Induction Melting* (VIM) and *Vacuum Arc Remelting* (VAR). Melting is commonly followed by a hot working process (extrusion or forging) and several cold working processes (as annealing and surface treatments).

2.1 Melting process of SMAs

The control of the melting process in SMAs has become a very important matter in the manufacturing of these material as its impact is huge regarding the functionalities of the final product. An small change in the chemical composition affects substantially the transformation temperatures of NiTi alloys. In addition, homogeinity of the final product impacts directly in the microscopic structure (grain size distribution and impurities concentration). Concerning this last issue, contaminants concentration, the main impurities are carbon, which has high affinity with titanium and has a large effect on transition temperatures and fatigue properties; and oxygen, which forms carbides and oxides with titanium. There are two main commercially-used methods to melt Nitinol: Vacuum Induction Melting (VIM) and Vacuum Arc Remelting (VAR). No clear advantages of one over the other exist but it is known that VIM is the easier for controlling chemical composition and VAR is better for reducing carbon. It is also important to point out that titanium is a extremely reactive element with carbon and oxygen. Thus, the melting process of Nitinol must be carry out in inert or high-vacuum furnaces.

2.1.1 Vacuum Induction Melting (VIM)

VIM process consists on melting Ni pellets and Ti rods housed together in a graphite crucible in vacuum conditions. The melt is achieved by the use of currents generated by electromagnetic induction and the electrodynamic forces ensure a good homogeinity of the mixture. Several functional characteristics as better electrical properties and good resistance against thermal cracking are also obtained with this method. The main problem of this technique is the high carbon contamination due to the use of a graphite crucible, which can be reduced by the utilization of low porosity graphite and crucibles with lower contact area.

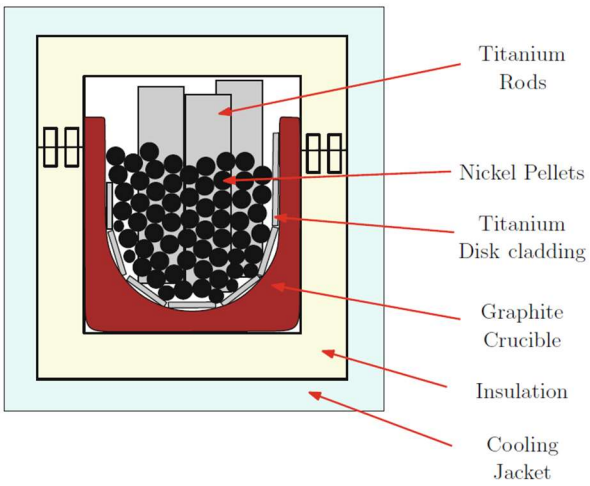

Fig. 11. Schematic disposition of VIM [2]

2.1.2 Vacuum Arc Remelting (VAR)

In case of VAR, the procedure is similar to VIM but with the difference of materials being placed into a consumable electrode and the melting is done in a water-cooled copper crucible. This leads to less contamination but, in order to obtain a good homogeinity, the melting process on the ingots has to be repeated several times.

The most common complete melting process consists on VIM and VAR associated: the VIM process is followed by VAR or multiple VARs.

2.1.3 Other melting processes: *Electron Beam* (EB) and *Plasma Arc Melting* (PAM)

These processes are useful for the manufacturing of other types of SMAs, as FeSMA, but in the case of NiTi, even provinding a high purity of the product, the lack of homogeinity and the expensive costs of the process make these two methods non-applicable in industrial production. However, in the EB process, the use of high vacuum environments and water-cooled copper crucibles leads to a very low level of carbon contamination.

2.2 Post-treatments of SMAs

In the industry, the control of the melting process is not enough to obtain the desired product. Several post-treatments as hot or cold working, joining, heat and surface treatments are neccesary in order to fulfill the requirements regarding the final properties of the material.

2.2.1 Hot and cold working

Once the melting process is completed, a hot working step is applied in order to reduce the size of the initial ingot, to establish the homogeinity and to adjust grain size. Moreover, hot working offers the capacity to obtain a suitable shape of the ingot: bars, composites or tubes. The process is performed in a range of temperatures from 800ºC to 950ºC. The next stage is a series of cold working processes with intermediate heat treatments in a range of temperatures 500-800ºC. It is a known fact that the ductility of NiTi allows 40-45% of cold working but, due to the high resistance to deformation of these materials, machining is difficult and tool wear becomes a very important issue to take into account when using conventional techniques. Thus, other cold

working mechanisms as *laser/plasma cutting, electric discharge machining* (EDM) and *water jet machining* are more useful and offer excellent size control and tolerance.

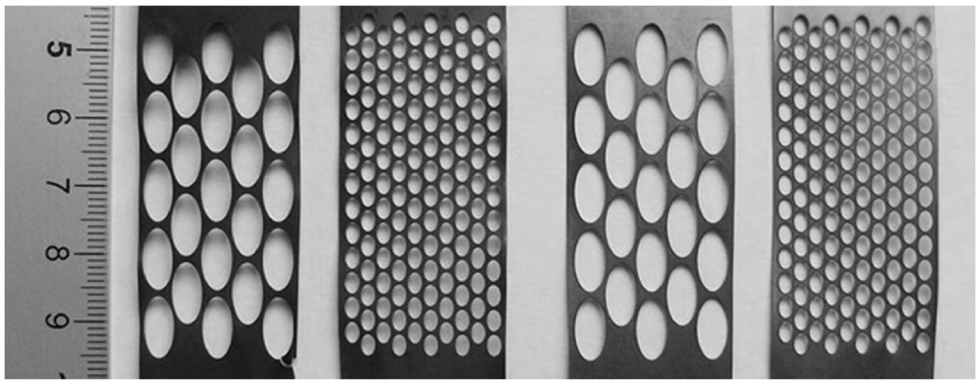

Fig. 12. Example of laser cutting on NiTiCu and NiTi [3]

2.2.2 Joining

Regarding the issue of "connecting" SMA components, it is known the fact that it is difficult to join/attach NiTi elements as the melting of a part of the simple may cause changes in the characteristic properties, affecting both SME and pseudoelastic effect. Therefore, the most reliable methods to achieve this goal are mechanical: crimping, swaging or staking. Nevertheless, in the past decades, traditional joining techniques as welding, soldering or adhesive bonding of SMA are being developed.

Joining NiTi to itself using a carbon dioxide laser has a successful result with its functional properties being intact. On the other hand, connecting SMA with other materials as stainless Steel (SS) is a challenge using traditional joining methods as welding due to the disparity of their chemical and physical properties. A process achieving good results is the *laser welding* which provides good precision over heat input, what decreases heat affected surface.

2.2.3 Surface treatments

In order to avoid Ni reaction/oxidation, a common surface treatment in NiTi SMA is the coating of the material with a pure titanium dioxide layer, which is accomplished by thermal oxidation in an environment with low levels of oxygen.

The type of surface treatment has a direct impact on fatigue, corrosion and other characteristic properties. Thus, depending on the application, many surface procedures can be chosen: *oxide surface, mechanically polishing, chemical etching, sandblasted surface, electropolishing, coatings or platings.*

3. Characterization of SMA

The characterization of SMA provides a better understanding of the material behavior and allows to derive the different quantitantive material properties, mainly in three thermomechanical fields: temperature, stress and strain. This process is esential for a proper explotaition and implementation of SMA materials in specific engineering applications. As many other types of materials, SMA are tested by means of subjecting specimens to different thermal or mechanical inputs while their response is being monitored. However, because of the unique behavior of SMA,

special considerations must be taken into account as the effects of training or the influence of mechanical and thermal loading rates.

Regarding the design of SMA specimens used in testing, the most common type of loading applied is tensile axial loading. Therefore, the most frequently tested are wire specimens as they develop relatively high tensile forces using a compact configuration. Wire specimens turn to be also very convenient for testing as they already arrive from the manufacturer in form of a coil wire and only need to be cut. On the other hand, as the cross section remains constant along the whole length of the specimen, excessive concentration of stress at the grips may occurr. When SMAs are received in a plate form, the most useful configuration is the 'dogbone'. The machining of these specimens is commonly performed by methods as wáter jet cutting and electrical discharge machining (EDM). In case of shear or multiaxial loading testing, specimens in form of tubes are used.

In the next paragraphs, the different experiments carried out in the characterization process are described.

3.1 Calorimetric analysis

This first analysis is the most fundamental step in the characterization of SMAs and it consists on the **determination of the zero-stress phase transformation temperatures (M_s, M_f, A_s, A_f)**, as they provide information about what phase is present in the alloy at any stress and temperature level and without this knowledge it is imposible to configure any additional experiment. The most popular test used for this aim is the ***Differential Scanning Calorimetry*** (DSC), where the difference in heat flow needed to increase the temperature of a sample and a reference is measured. In the thermogram showing the variation of heat flow versus temperature obtained, two **peaks** can be observed. These peaks are characteristic of any first order phase transformation like melting of ice (solid-liquid) or boiling water (liquid-gas), but being in this case solid-solid transformations. Associated to the transformation from martensite to austenite there is an endothermic peak due to the excess of heat that needs to be supplied to mantain a constant heating rate. The peak present in the transformation from austenite to martensite is exothermic as in this case, to keep a constant heating rate some heat must be released. To determine the transformation temperatures from this thermogram tangent lines to the start and finish of each peak and also to the baseline heat flows are constructed. The intersection of this lines provides a value for each of the start and finish transformation temperatures. For each transformation it is also possible to identify a peak temperature (the maximum temperature reached during each transition).

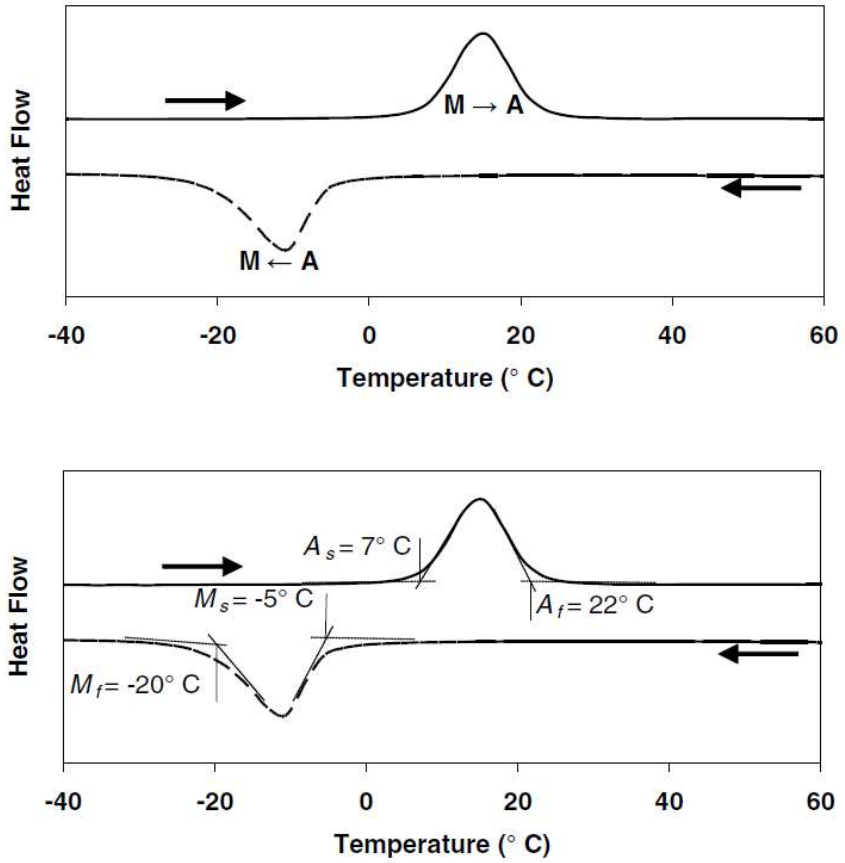

Fig. 13. DSC thermogram and determination of the zero-stress transformation temperatures using tangent lines [1]

It should be noted that some materials show an R-phase. The transformation to R-phase in thermograms can be confused with the austenitic of martensitic transformations due to the peaks exhibited are not clear. During cooling, two exothermic transitions can be detected: austenite→R-phase and R-phase→martensite.

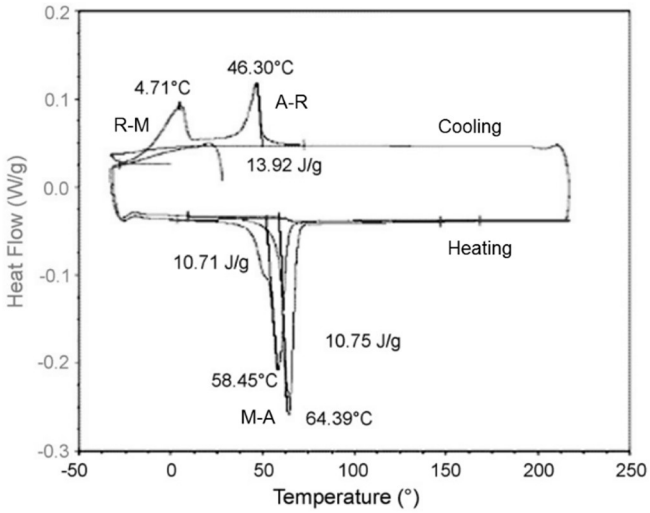

Fig. 14. DSC thermogram of a SMA exhibiting an R-phase [7]

The procedure for the determination of the four zero-stress transformation temperatures by means of the DSC method is described in the ASTM standard F2004-05 “Standard Test Method for Transformation Temperature of Nickel-Titanium Alloys by Thermal Analysis”.

3.1.1 Alternative methods for the determination of the zero-stress transformation temperatures

When the material is subjected to cyclic loading, the peaks observed in the thermogram of the DSC disappear and there is the need to use other characterization methods.

3.1.1.1 Electrical resistivity measurements

Some authors as Uchil et al. have shown that the electrical resistivity measurements method is a very useful technique to identify the four zero-stress transformation temperatures of a SMA specimen when they are not detectable from the calorimetric analysis. It can be observed that electrical resistivity increases during reverse transformation (M→A), and decreases during forward transformation (A→M). In addition, if the R-phase is present in the alloy, resistivity approaches to a maximum value.

The procedure of this method consists on measuring the variation of electrical resistivity with temperature. Specimens are heated and cooled in a thermostatic chamber at constant rate. A current is forced to circulate through the sample, whose value has to be small enough in order not to influence the specimen’s temperature. Temperature and voltage values are collected (a signal amplifier can be used to amplify the voltage values acquired). The electrical resistivity can be obtained as $\rho = \frac{V \cdot A}{I \cdot L}$, being A and L the cross section and the length of the wire, respectively. With these values, the resistivity-temperature curved is monitored.

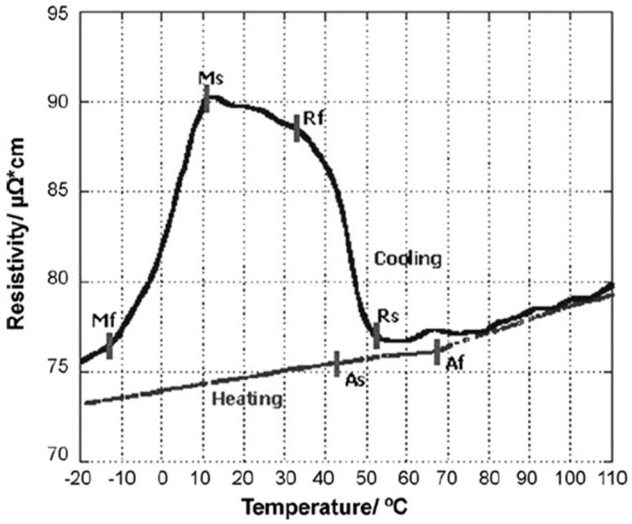

Fig. 15. Electrical resistivity vs. Temperature diagram of a NiTi alloy [7]

The typical resistivity-temperature curve during heating shows a linear variation with two small changes in slopes corresponding to the austenitic start and finish temperatures. During cooling, due to the presence of the R-phase, the curve has a ‘cap’ shape with a maximum where the R-phase and martensitic start and finish temperatures can be identified.

3.1.1.2 Bend and Free Recovery method

The Bend and Free Recovery method is a technique to determine the transformation temperatures of NiTi alloys and it consists on measuring the strain recovered during transformation. It is based on the Shape Memory Effect. The procedure comprises the following steps: cooling the specimen to fully martensitic state, bending the specimen and heating it to fully austenitic state. The deformation recovered during heating versus the temperature is measured. These steps are extensively described in the ASTM standard F2082-15 "Standard Test Method for Determination of Transformation Temperature of Nickel-Titanium Shape Memory Alloys by Bend and Free Recovery". From this standard, two different apparatus can be used: LVDT (linear variable differential transducer) or RVDT (rotary variable differential transducer).

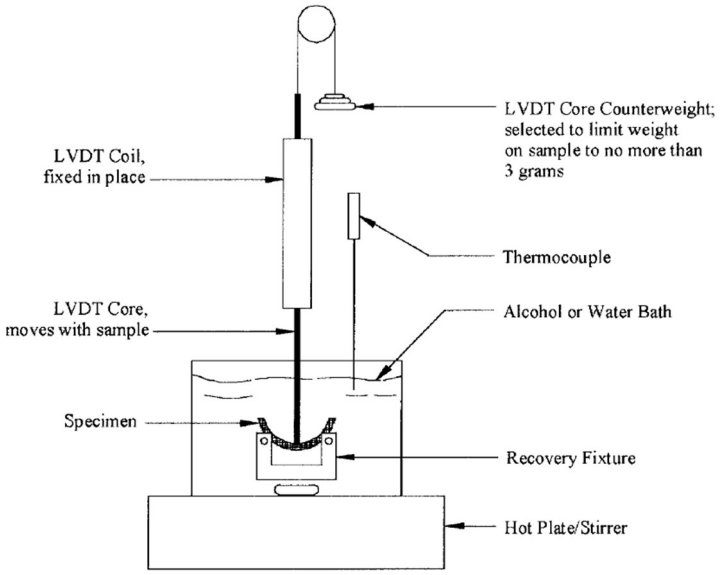

Fig. 16. Graphical representation of the Bend and Free Recovery method set-up using a LVDT (standard f2082)

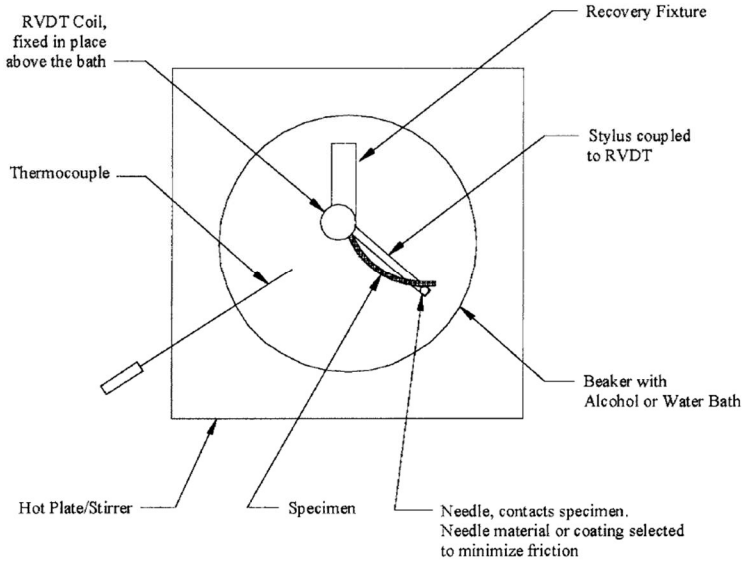

Fig. 17. Graphical representation of the Bend and Free Recovery method set-up using a RVDT [5]

Transformation temperatures are determined from the displacement-temperature diagram by the tangent line method. If the transformation occurs in one stage (no R-phase), the tangent line to the middle part must be drawn tangent to the steepest portion of the curve. If the R-phase is present, the transition takes place in two stages, and the lines must be drawn tangent to the steepest portions of both stages.

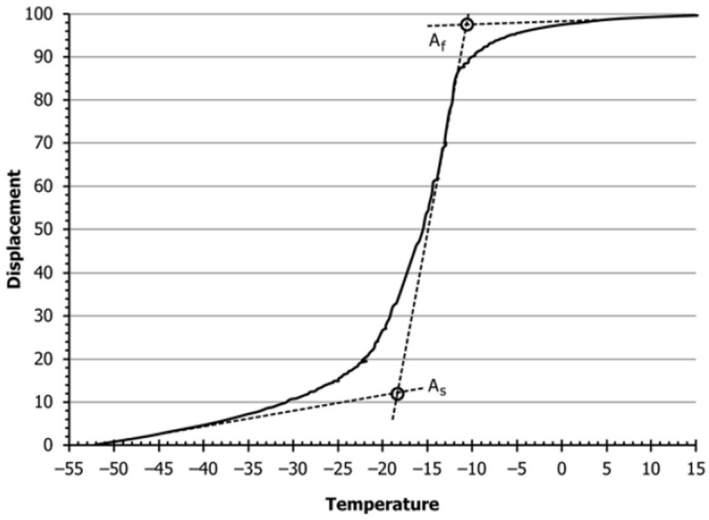

Fig. 18. Displacement-temperature diagram of the reverse transformation (without R-phase) and determination of the transformation temperatures of austenite [5]

3.2 Thermomechanical characterization

To characterize the mechanical properties of SMAs, several loading paths are applied while different parameters associated with the phase transformations are monitored and recorded. As it is mentioned before, this chapter will be focused on three thermomechanical fields: stress, strain and temperature. In a standard test on a SMA, two of the variables are defined; stress and temperature or strain and temperature, and the variation of the third one is measured; strain or stress respectively.

In order to study the thermomechanical properties of SMAs, we need to have a knowledge about which mechanical parameters should be determined. These parameters can be divided in:

- *Thermoelastic properties*: they provide an understanding about material behavior when transformation is not occurring.
- *Properties associated with phase transformations*: these variables describe when the phase transformations start and end depending on the current state (stress and temperature) and loading history of the material.

3.2.1 Thermoelastic properties

Considering in the first place the **pseudoelastic effect**, the material is loaded at a **constant temperature** above A_f (stable austenitic phase) and shows an elastic behavior represented by the **Young modulus of austenite (E^A)**. When continuing loading, austenite transforms into martensite. Once the transformation is complete and we start unloading, martensite has an elastic response

determined by the **Young Modulus of martensite (E^M)**. These two parameters can be measured in the stress-strain diagram of the pseudoelastic effect by drawing tangent lines to the start of both elastic performance lines; they constitute the slope of these mentioned lines in the stress-strain diagram. These thermoelastic properties can also be determined by loading/unloading the material in fully austenitic and martensitic states at levels of stress sufficiently low to avoid phase transformations.

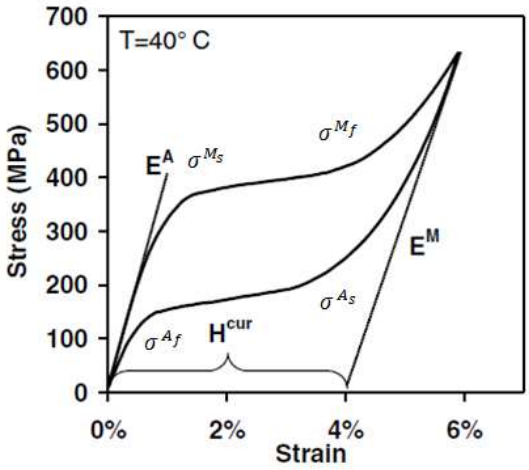

Fig. 19. Pseudoelastic effect stress-strain diagram with identification of the Young moduli of austenite and martensite [1]

From this diagram, the four characteristic transformation stress levels can be estimated. When starting loading, the specimen shows a linear response but at some stress level, σ^{M_s}, austenite begins to transform into martensite. The transformation finishes at a stress level σ^{M_f} and if the stress continues increasing, linear behaviour of martensite is observed. Similarly during unloading, the stress levels σ^{A_s} and σ^{A_f} can be indentified.

By increasing/decreasing temperature under **constant load** and relying on the **shape memory effect** strain-temperature diagram, the **coefficients of thermal expansion of austenite (α^A) and martensite (α^M)** can be obtained. These parameters represent the temperature induced strain behavior in fully austenitic of martensitic states, before the phase transformations start, by defining the slopes of the strain-temperature plot in these two states.

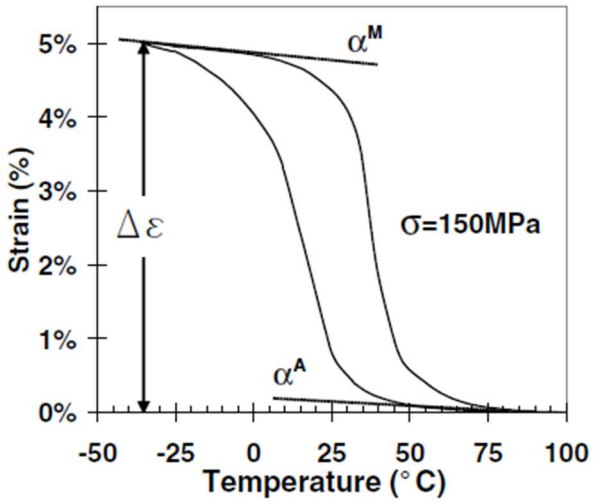

Fig. 20. SME strain-temperature diagram with indentification of the coefficients of thermal expansion of austenite and martensite [1]

Another important information is the elastic limit of the material, represented in this case by two parameters: the yield stress of austenite (σ_Y^A) and martensite (σ_Y^M).

3.2.2 Properties associated to phase transformations

Finally, it is necessary to determine the **properties required to construct the phase diagram**, which mainly include the stress and temperature parameters present in phase transformations. The aim is to set **transformation regions** or boundaries in the stress-temperature diagram in order to define where the phase transformations start and end. These transformation surfaces are delimited by their points of intersection with the x-axis, which are the zero-stress transformation temperatures, and the slopes of these surfaces at some stress level, known as *stress influence coefficients*. There exist up to 4 slopes, but it is considered that each pair of slopes belonging to each transformation region ($A \rightarrow M$ and $M \rightarrow A$) are equal. Therefore, we have two stress influence coefficients: C^M and C^A, respectively.

With the four zero-stress transformation temperatures and the two stress influence coefficients, both transformation surfaces are already defined, but it is also useful to determine the stress levels at which the detwinning process of martensite starts and ends (σ_s, σ_f).

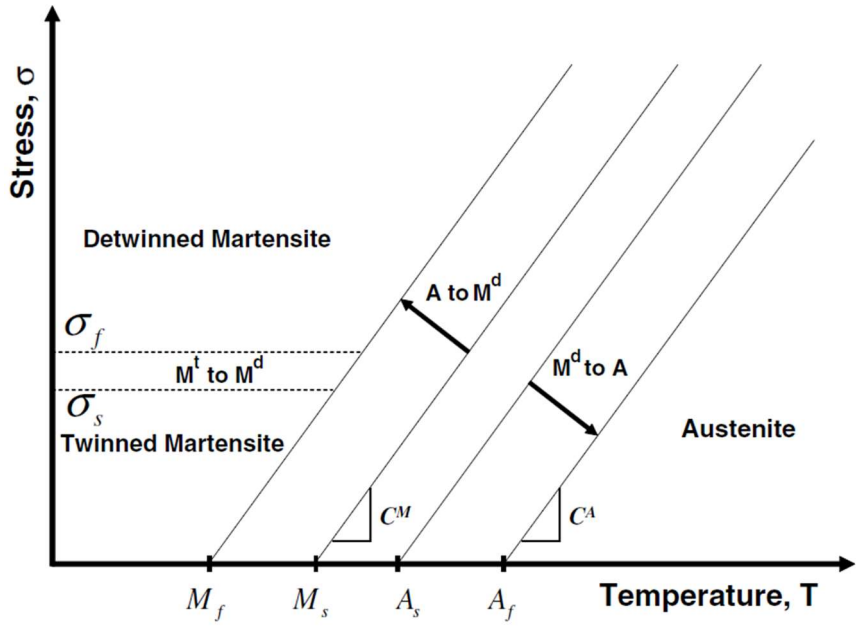

Fig. 21. Schematic representation of a phase diagram and indentification of the material properties previously mentioned [1]

3.2.3 Experimental characterization process and construction of the phase diagram

The first experiment that needs to be carried out is a monotonic **loading/unloading of the specimen** in two different states: pure martensite ($T < M_f$) and pure austenite ($T > A_f$). By testing the material below M_f and above A_f we obtain important information about the mechanical properties of martensite and SME behavior, and the mechanical properties of austenite and pseudoelasticity behavior, respectively. Therefore, this first experiment is divided in two parts:

- **Testing at a constant temperature $T < M_f$**: The test starts with the specimen in fully martensitic state at a temperature below M_f to ensure martensite is the only stable phase. The sample is loaded until detwinning process is complete and to a maximum stress level. This maximum stress is not set a priori, but chosen while the experiment is taking place by noting detwinning is complete. Then, the specimen is unloaded and the temperature is increased above A_f while monitoring the strain recovery. SME behavior is observed.

  The results of this test are shown in a stress-strain diagram and the thermomechanical properties of the martensite phase can be obtained. For the detwinning start and finish stresses, they can be approximated by drawing a tangent line to the detwinning curve. Its intersection with the tangent lines to the fully twinned and fully detwinned plots gives us the points of σ_s and σ_f.

  Even if temperature is not plotted in this diagram, it is possible to observe the SME strain recovered when the sample is heated up to austenitic state completely unloaded. It can also be observed that not all the deformation recovers, but there is some residual strain which indicates that the material is not showing a stable behavior and training is required.

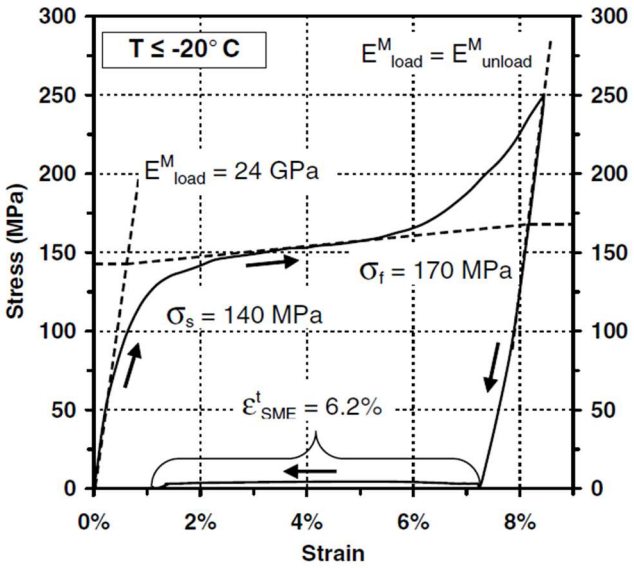

Fig. 22. Loading/unloading at a temperature below M_f and subsequent heating until austenitic state is reached [1]

- **Testing at a constant temperature $T > A_f$**: In this test the specimen is loaded and unloaded at a temperature above A_f and nearly total pseudoelastic effect can be observed. From the stress-strain diagram we can calculate the Young modulus of austenite and also the Young modulus of martensite. In this case, E^M is significantly higher than the value obtain in the previous test. This fact may be due to the existence of some austenite that has not transformed to detwinned martensite at the end of loading. From this diagram, two other properties can be identified: the upper plateau stress (stress at 3% strain during loading) and the lower plateau stress (stress at 2.5% strain during unloading).

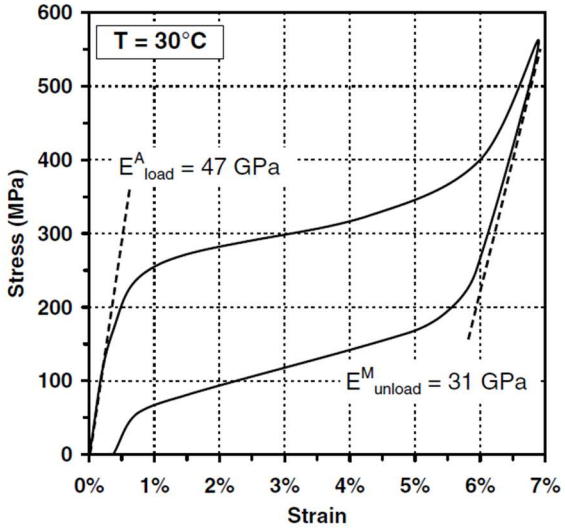

Fig. 23. Loading/unloading at a temperature above A_f [1]

Finally, it can also be useful for future applications the determination of the yield stresses of martensite and austenite. In order to determine the martensitic yield stress σ_Y^M, the SME specimen is used and it is easily identified as its value is clearly higher than the detwinning start

and finish stresses. In relation to the yield stress of austenite σ_Y^A, it is necessary that the test is performed at a temperature above A_f so that the austenitic phase is stable.

Regarding the construction of the phase diagram, two sets of points are necessary to determine the transformation surfaces. The first one is constituted by the four zero-stress transformation temperatures obtained by the DSC test. The second one is acquired by performing a non-zero SME test, also called ***isobaric testing***. The first step of this test is to heat the specimen above A_f and stress it to a **constant stress level**. Next, austenite transforms into martensite while the load is mantained by decreasing the temperature. Lastly, the sample is heated up again until reverse transformation is completed and the strain is recovered. From the results of this test, the four transformation temperatures at a given stress level (M_s^σ, M_f^σ, A_s^σ, A_f^σ) are obtained by tangent lines to the strain-temperature plot. With these two set os points, the slopes of the two transformation regions can be sketched.

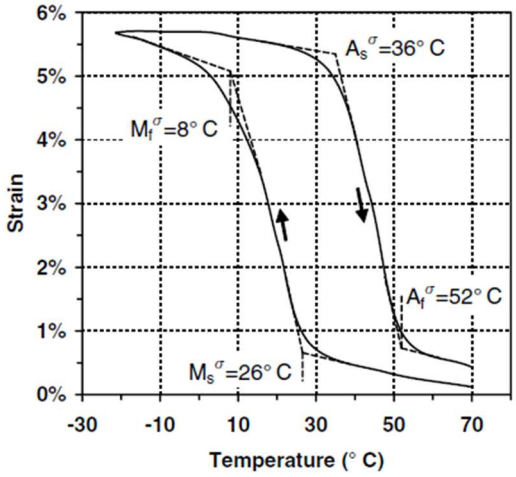

Fig. 24. Isobaric testing plot ($\sigma = 200\ MPa$) and estimation of the non-zero stress transformation temperatures [1]

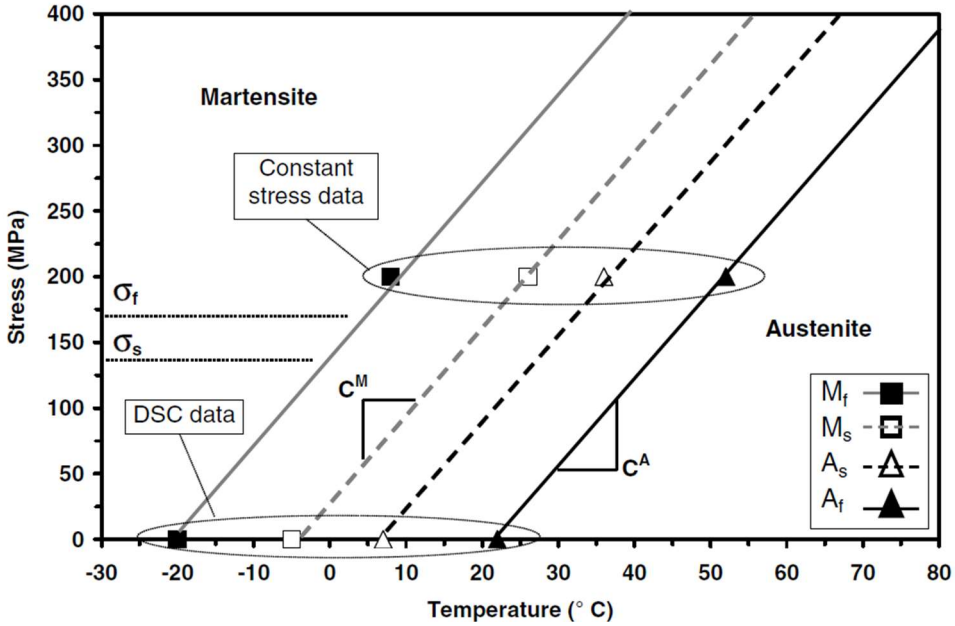

Fig. 25. Construction of the phase diagram with DSC data and data from the isobaric testing [1]

This phase diagram is not accurate enough to calibrate a model, but it can be useful for planning the training process.

3.3 Electrical characterization

SMA actuation is based on the SME, as this effect can be used for generating force and/or motion. The required heating power to activate the SME can be provided indirectly to the material by means of variation of the ambient temperature, or directly by Joule effect (electrical heating).

The variation of the current through an actuating wire versus different variables can be obtained through what can be called *one-shot* test. The procedure consists on clamping the tested wire on its top end with a constant weight clamped at its bottom end. At the bottom side of the weight, a laser sensor is placed which is able to measure current, applied load, stroke and time of actuation.

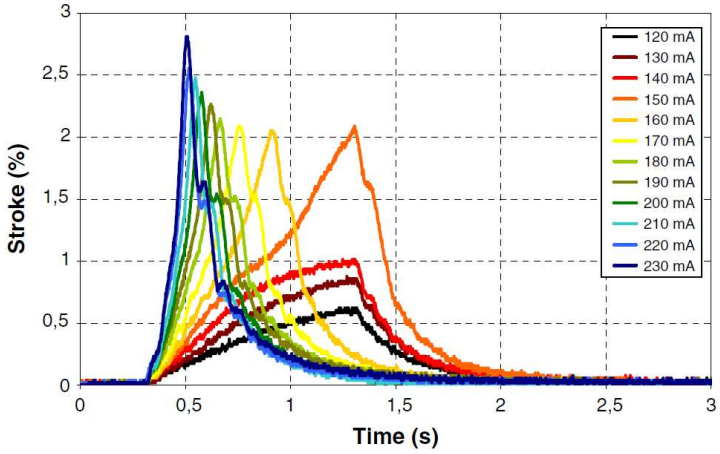

Fig. 26. Actuation times and strokes for a SmartFlex® NiTi wire using different heating currents [21]

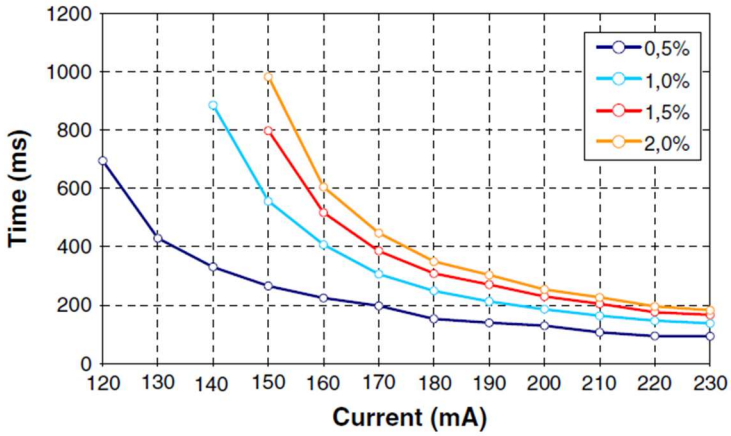

Fig. 27. Actuation times and currents for a SmartFlex® NiTi wire as a function of different strokes [21]

3.4 Effects of training

In order to determine the effects of cyclic loading on the response of SMAs, specimens are subjected to several transformation cycles. If the application of the SMA is working as an actuator, a common method is to apply to the specimen multiple thermal cycles under constant stress (training). The aim of training is to obtained a **stabilized thermomechanical response**. Therefore, the load applied should exceed or be equal to the maximum value expected in the application.

Once the material has been trained and its response is stabilized, some of the tests of the characterization process described before should be performed again, as some material properties may have changed. Regarding the DSC results, training eliminates the peaks observed during heating and cooling and thus, another method to determine the four zero-stress transformation temperatures must be used after cylic loading. In addition, the new phase diagram of the trained material has to be constructed. To this aim, the four phase transformation temperatures at different stress levels (e.g. from 2.5 MPa to 200 MPa in increments of ~50 MPa) need to be obtained by performing several isobaric test. These four temperatures can be estimated by sketching tangent lines in the strain-temperature diagram. By placing these sets of points and extrapolating the transformation surfaces, the estimated phase diagram of the trained specimen is achieved.

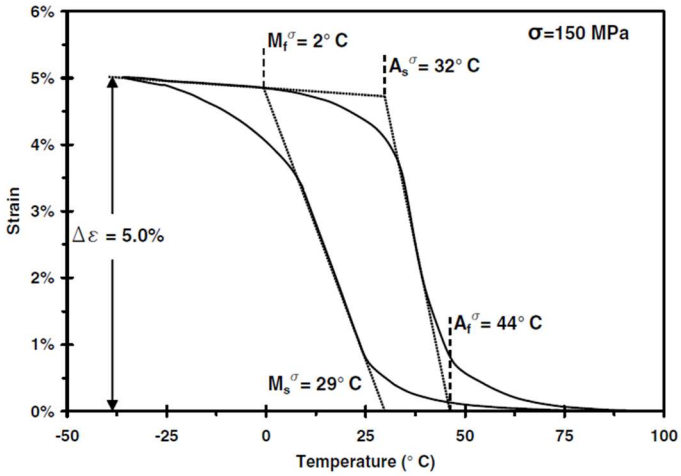

Fig. 28. Example of the estimation of the four non-zero stress transformation temperatures from the results of the isobaric test at a stress level of $\sigma = 150\ MPa$. [1]

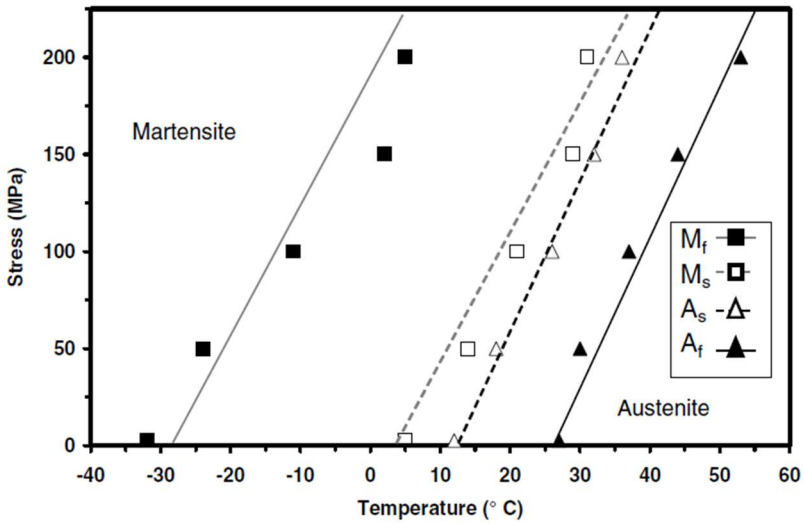

Fig. 29. Experimentally derived phase diagram of a trained specimen [1]

3.5 Importance of mechanical and thermal loading rates

From the results of the DSC analysis, we can derive that forward transformation ($A \rightarrow M$) is exothermic and reverse transformation ($M \rightarrow A$) is endothermic. Regarding pseudoelastic testing, these experiments are performed, in ideal conditions, at constant temperature. In reality, if loading occurs slowly, the heat generated during the transformation into martensite can be dissipated due to conductive and convective processes. On the other hand, if loading is fast this additional heat from the exothermic transformation will be added to the material and the temperature will be increased. Then, the isothermal assumptions are violated. In conclusion: thermal effects due to loading are of great importance, specially at high rates. For isothermal loading at any temperature, suggested rates would be $\sim 0.01 - 0.05$ % strain/sec. Concerning the detwinning transformation, some studies have shown that it is independent from the strain rate.

Instead of using prescribed strain rates or displacements, force control can be selected, which consists on setting an ending force value. However, this method in 'flat' pseudoelastic loading/unloading may lead to problems as a concrete constant load level is suitable in the elastic behavior but generates very high strain rates during the stress-induced transformation.

3.6 Fatigue characterization

For a good design of SMA actuators, it is necessary an exhaustive knowledge of the fatigue behavior of the material. Two types of fatigue can be observed in SMA. **Pure mechanical fatigue** is described as the behavior of the alloy when subjected to cyclic mechanical loading under constant temperature. The other type of fatigue in SMA is called "**thermomechanical" or "functional"** as their actuation is based on thermal activation.

3.6.1 Mechanical fatigue characterization

In order to determine the mechanical fatigue properties of SMAs (specifically NiTi wires) in their martensite and austenite phases, two methods have become the stardard: ***chuck-to-chuck method*** and ***machined block method.*** In both procedures, the wire is subjected to cyclic mechanical loading at different speeds and up to different strain levels at a temperature higher that A_f (fully austenitic state). The pseudoelastic effect is observed. The number of cycles is evaluated; the test ends when the wire breaks or when a prescribed number of cycles is achieved without failure.

The chuck-to-chuck method set-up consists on clamping the wire at both ends forming a ellipse-like curvature and both chucks actuate at the same speed. Another alternative set-up is made of one chuck, where one end of the wire is constraint, and a bushing system, where the other end of the wire moves freely. During the test, the wire specimen is inmersed in a fluid bath in order to eliminate any increase in temperature due to heat generated during exothermic transformation into stress-induced martensite (SIM).

Fig. 30. Chuck-to-chuck method set-up [22]

The diameter of the wire tested and the radius of the curvature determine the value of the strain applied: $R = \frac{r}{\varepsilon} \cdot 100\ [\%]$, where r is the diameter of the wire R the radius of curvature of the neutral axis of the wire and ε the desired strain. Once we determied the curvature radius needed to apply the desired strain, the chuck-to-chuck distance (C) and the length of the wire (L) are calculated (in these calculations, the additional length of the wire inserted into each chuck is not considered):

$$C = \frac{R}{0.417}$$

$$L = 2.19C$$

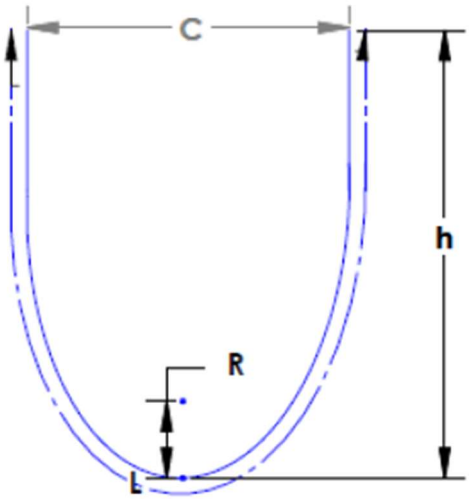

Fig. 31. Chuck-to-chuck method calculations [22]

These calculations where developed by Clarke and Bates of Hunter Spring Company around 1940 and for strains larger than 1% suffer a lost of precision.

The chuck-to-chuck machine includes a break detection sensor. If breakage of the wire does not occur in the center of the test specimen, the actual strain at failure must be calculated from the initial desired strain multiplied by a correction factor. This strain correction factor depends on the difference in length between the two portions of the specimen after breakage.

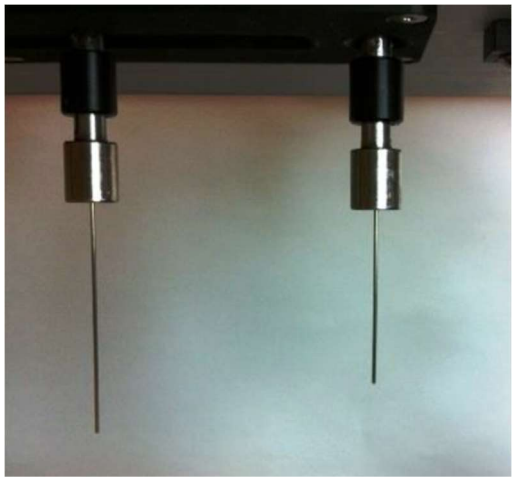

Fig. 32. Uneven failure of the wire in the chuck-to-chuck method [22]

$Difference \quad \frac{L_2-L_1}{2L} \cdot 100\ [\%]$, being L_1 and L_2 the lengths of the two portions of the wire after failure.

Length Difference (%)	Strain Correction Factor (%)
1.0	0.1
2.0	0.3
3.0	0.7
4.0	1.2
5.0	1.7
6.0	2.5
7.0	3.4
8.0	4.4
9.0	5.6
10.0	6.7
15.0	14.4
20.0	24.3

Fig. 33. Strain correction factor depending of the length difference (a comparison of zero mean…)

Regarding the machined block method, its set-up is formed by a polymer block where a groove is machined. The tested wire is inserted in this groove with enough clearance so that all effects due to friction are avoided. A transparent plastic cover is placed on the block in order to retain the specimen during the coure of the test. The wire forms now a curvature of 90º whose radius depends on the desired applied strain (as before: $R = \frac{r}{\varepsilon} \cdot 100\ [\%]$). Therefore, the strain is controlled by the shape of the groove, and speed is set on a motor control. The detection of breakage is performed by a laser counter. As in the chuck-to-chuck method, the test parts are inmersed in a temperature-controlled fluid bath.

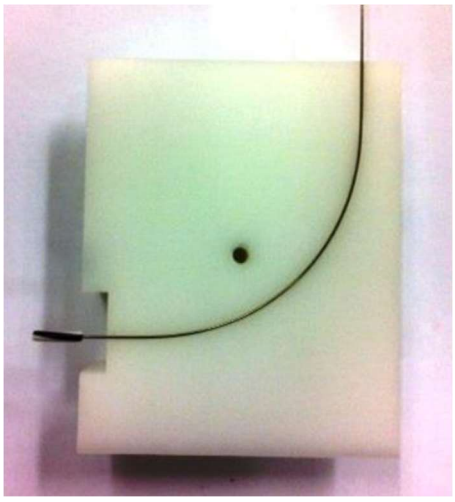

Fig. 34. Wire specimen inserted in a machined block [22]

Fig. 35. Machined block method complete set-up [22]

3.6.2 Functional fatigue characterization

In order to characterize functional fatigue, the tests to be carried out consist, generally, on loading the sample and subject it to thermal cyclic loading by changing the supplied current (Joule effect). This experiment can be performed with four different loading conditions: constant stress, constant strain, constant stress with limited maximum strain and linear stress-strain cycle (only the first three will be described in this paper).

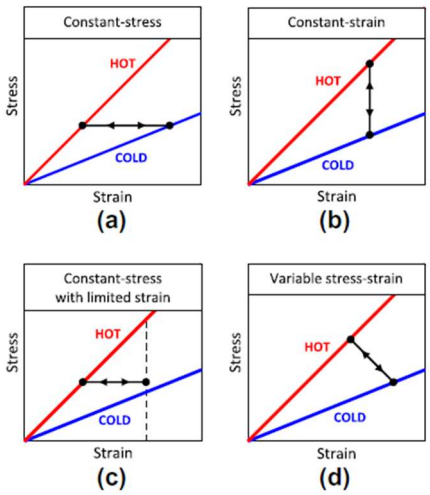

Fig. 36. Tests proposedto characterize SMA wires under functional fatigue: (a) constant stress; (b) constant strain; (c) constant stress with limited maximum strain; (d) linear stress-strain cycle [11]

In order to perform these tests, the machine shown in the following figure can be built. Essentially, it consists on a C-shape alluminium chassis. The top end of the SMA wire is clamped to the upper part of the chassis, and the bottom end is loaded or constraint using a certain mechanism. The heating is carried out through Joule effect and the electric current is provided by an electronic power board. The cooling is performed by an electronically-controlled variable-speed fan.

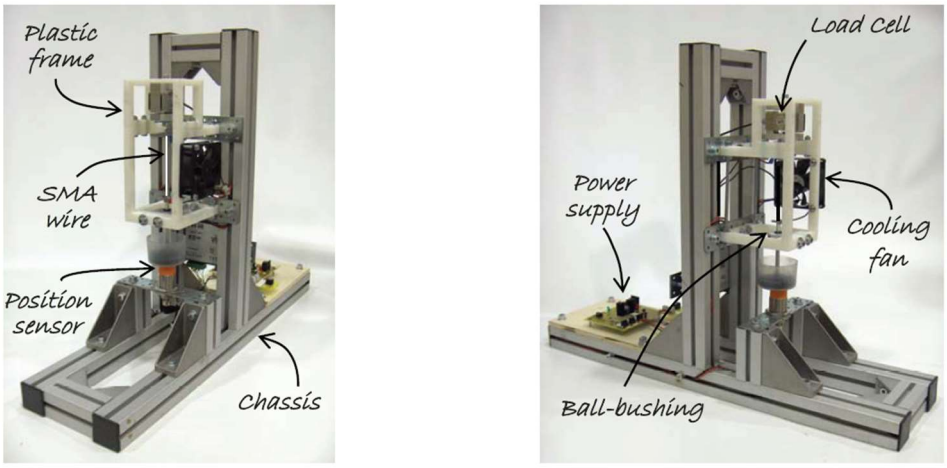

Fig. 37. Set-up used in the experiments for functional fatigue characterization [12]

For the execution of the constant stress test, a loading basket is attached to the wire. In the case of the constant-strain test, the lower end of the rod is locked. Finally, in order to perform the constant stress with limited maximum strain test, the loading basket is included as well as a polymer spacer is placed on top of the displacement sensor working as a hard stop.

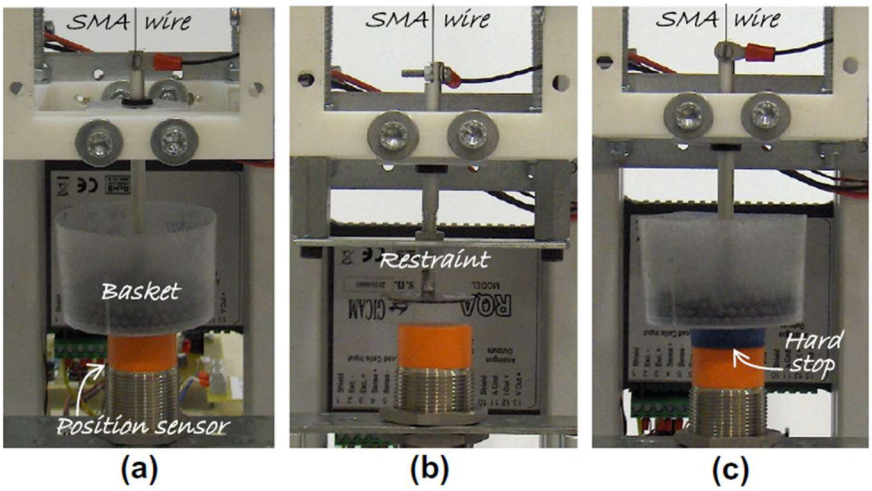

Fig. 38. Loading devices used to apply the three loading conditions: (a) constant stress; (b) constant strain; (c) constant stress with limited maximum strain [11]

Regarding the results of these experiments and in the case of constant stress tests, the aim is to identify the number of cycles to failure for a specific applied stress (Woehler's strength-life curve). The tests are performed at different stress levels and finish when fracture of the sample occurs or after a prescribed number of cycles without failure.

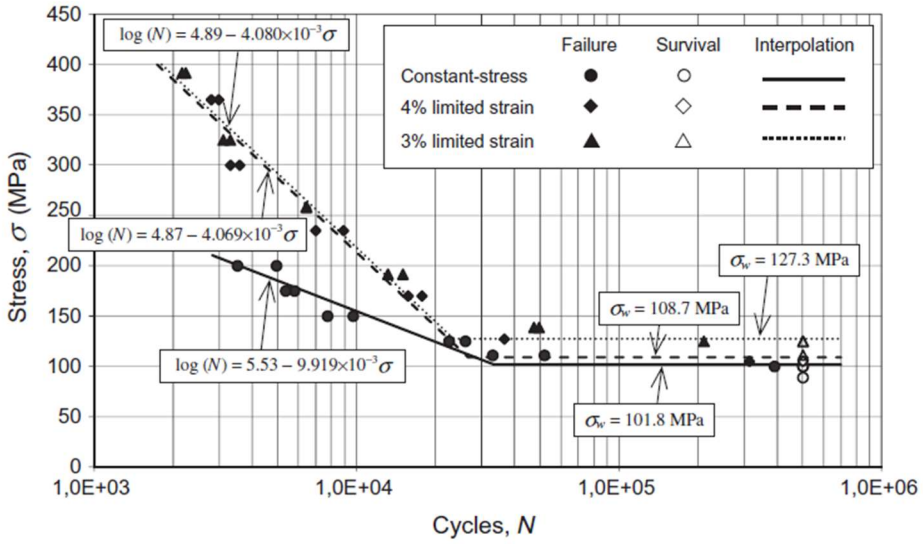

Fig. 39. Woehler's diagram containing the results of a constrant stress test and two constant stress with limited maximum strain to 3% and 4% tests [11]

From this graph, it can be observed that putting a limit to the maximum strain is extremely beneficial with regard to the functional fatigue behavior of the specimen.

Concerning the data obtained from the constant strain tests, a diagram showing the applied strain with respect to the number of cycles to failure can be plotted.

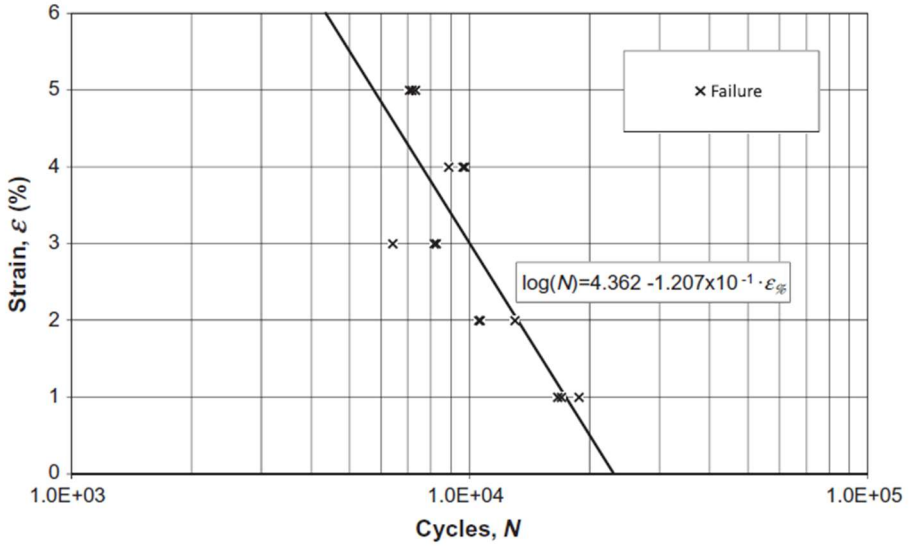

Fig. 40. Woehler's diagram containing the results of the constant strain test [11]

4. Design of SMA spring actuators

In order to design SMA actuators, it is necessary to define three main characteristics: the temperature profile, the load levels and/or the displacement outputs. There exist three different setups for a spring (or wire) actuator: controlling the load, controlling the displacement, or

controlling both load and displacement simultaneously. Two main keys are involved in the design of a 'two-state' actuator:

- Highest temperature applied: The maximum temperature of the application must be sufficiently higher to ensure that the actuator is in fully austenitic state when loaded. If it is not high enough, stress-induce martensite (SIM) transformation will occur. In other words, the component should be heated enough so that the upper plateau stress (UPS) excedes the maximum load applied.

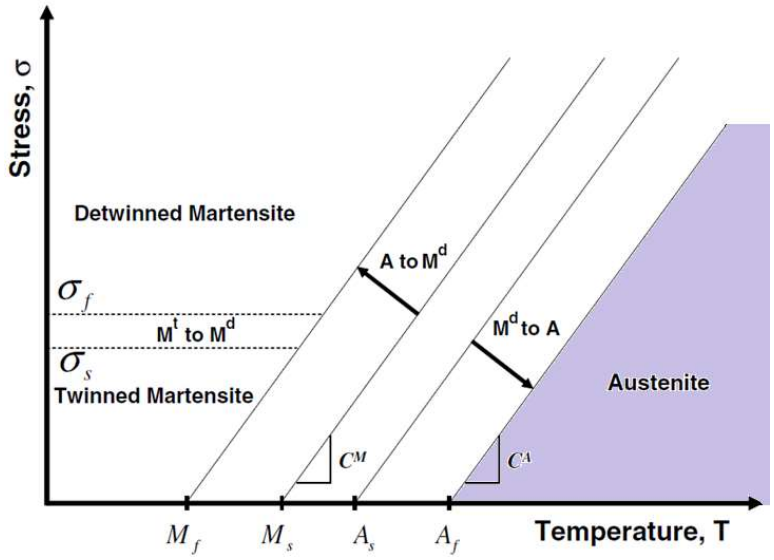

Fig. 41. Area where the maximum stress and maximum temperature must be

- 'Stroke limiter': It is useful to use a 'stroke limiter' or 'hard stop' in order to be able to limit the elogation of the spring at low temperature ($T < M_f$) and not reach the elogation response to the load. Commonly, in springs this strain is limited to 1.5%, what allows these components to not be affected by cyclic loading and last 'infinite' cycles.

4.1 Modes of operation

The two main modes of operation of spring actuators are:

CONSTANT FORCE MODE

The SMA spring exerts a constant force while its length varies with temperature.

Being in its martensitic state ($T < M_f$), the spring is subjected to a external constant load (e.g. a weight) and it deforms until state B. When the temperature increases above A_f, some strain is recovered reaching an intermediate point between the initial configuration A, where the spring was totally compressed, and the deformed state B. During this movement, the spring works as a thermal actuator lifting the load. By cooling, the spring returns to the state of free elongation under external load in martensitic phase (D). The net stroke obtained in this mechanism is the difference between the extended length in the cold state and the hot state. The 'stroke limiter' mentioned before is commonly used when the spring is reaching state B, so this deformation is controlled. As usual, the variation of the elongation of the spring with the force applied has a linear behavior, in both austenitic and martensitic phases.

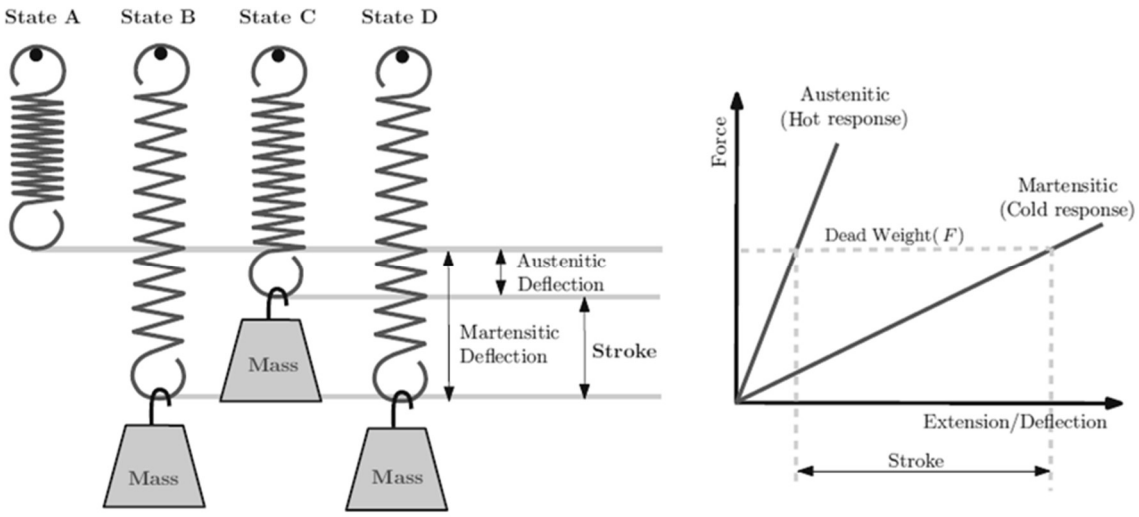

Fig. 42. Spring operating in constant force mode [2]

CONSTANT DISPLACEMENT MODE

In this mode of operation, the maximum displacement of the spring is constraint and the force exerted varies with temperature. That is to say, consider a SMA spring in its martensitic state, stressed a certain deformation and clamped so that this displacement is constraint. If the temperature starts to increase, reverse transformation takes places and the spring tries to recover its original form. Due to the constrains, this results in a recovery pulling force exerted by the spring. This force can be varied by changing the operating temperature above A_f.

A third useful mode can also be consider: force and displacement varying simultaneosly with temperature.

EXPERIMENTAL PROCEDURE

In this section, all the procedures and tests carried out in the laboratory will be expounded. Our main objective is to determine the main thermomechanical properties of a SMA spring actuator. In order to achieve this, we have a SMA SmartFlex® wire from the SAES Group, which will be reshaped into several springs. After the reshaping, two test will be carried out to learn some of the mechanical actuating properties of our springs:

- Test 0: Measurement of the residual strain
- Test 1: Measurement of the variation of the force with time for a constant applied current

1. Wire reshaping into a spring

The SMA wire we are provided with is a SmartFlex®04, which is a SAES Getters' product line of shape memory alloy semi-finished components. Our wire has the following thermomechanical properties:

Diameter 400 µm

Maximum force 75 N

Maximum stroke 5%

Suggested operating force 21 N

Suggested operating stroke <3.5%

Transformation temperatures of the wire loaded at different stress levels:

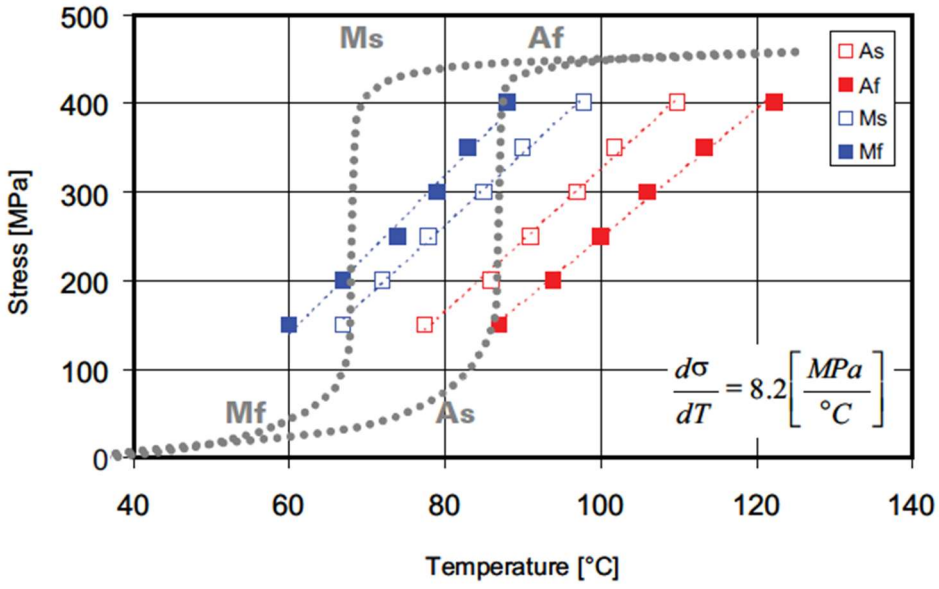

Maximum transformation temperature (activation temperature) $A_f \approx 120^{\circ}C$

Resistivity:

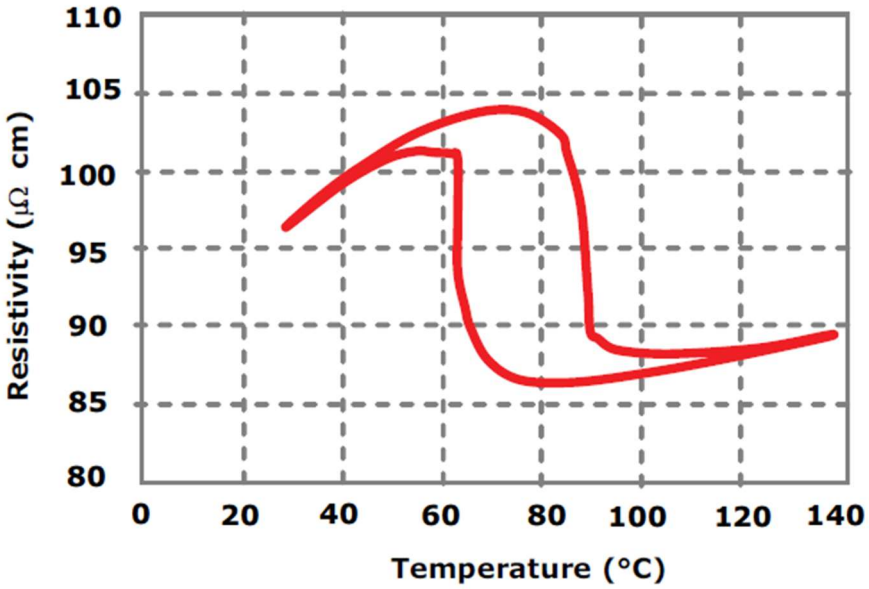

Stroke development with time:

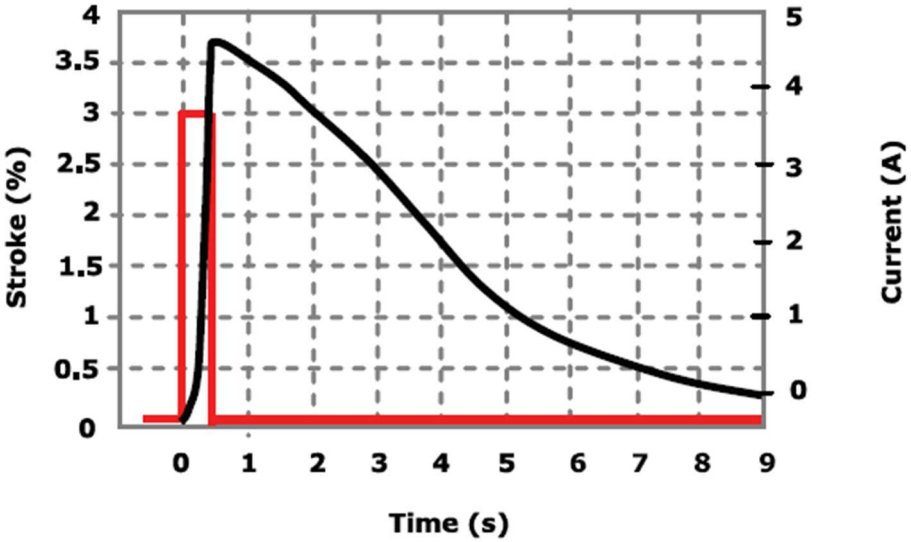

1.1 Experimental set-up

The helicoidal shape of the spring was achieved by means of coiling the wire around a bolt. The ends were clamped between the head of the bolt and a nut + a washer (in one end) and two nuts (in the other end). A turn of the wire was made in between the nuts to make the clamping more secure. A groove of around 45º of inclination was machined on the nuts in order to be able to pass the wire through them. The coiling was made manually. For the last springs being reshaped (3, 4, 5 and 6), a longitudinal hole was made in the bolts, where a thermocouple was placed. This set-up was place in a furnace at temperatures ranging from 400 to 550˚C and the heat treatment time was around 30 minutes. The thermocouple allowed us to measure the temperature inside the bolt during the heat treatment.

Fig. 43. Wire reshaping experimental set-up

Fig. 44. Close-up of the set-up

Fig. 45. Furnace used for the heat treatment

1.2 Heat treatments' results

SPRING 1

The bolt used was an M5.

The spring was put in the furnace at time zero.

Furnace temperatures:

(t=0) $T_{start} = T_{amb}$

(t=30') T = 400°C

(t=34') T = 450°C

(t=38') T = 500°C

This last temperature was mantained for 5'. Then, the bolt was extracted and cooled by water quenching.

SPRING 2

The bolt used was an M5.

The spring was put in the furnace at time zero.

Furnace temperatures:

(t=0) T_{start} = 500°C

(t=9') T = 550°C

This last temperature was mantained for 3'. Then, the bolt was extracted and cooled by water quenching.

This last test was shorter and more efficient, as the furnace was pre-heated when the bolt was introduced.

SPRING 3

The bolt used was an M5.

The spring was put in the furnace at time zero. The temperature of the furnace was T_{oven} = 450°C.

Temperatures recorded by the thermocouple:

(t=1') T = 250°C

(t=2') T = 320°C

(t=3') T = 360°C

(t=5') T = 410°C

(t=8') T = 430° C

(t=10') T = 430°C This temperature is considered as start (then, the temperature oscillates between 430°C and 435°C)

(t=40') T = 430°C

Then, the bolt was extracted and cooled by water quenching.

SPRING 4

The bolt used was an M5.

The spring was put in the furnace at time zero. The temperature of the furnace was T_{oven} = 470°C.

Temperatures recorded by the thermocouple:

(t=2') T = 230°C

(t=7') T = 453°C This temperature is considered as start, the temperature of the furnace was changed to T_{oven} = 450°C

(t=10') T = 462°C

(t=13') T = 470°C

(t=23') T = 460°C

(t=32) T = 452°C

(t=37') T = 452°C

Even if the temperature of the furnace was reduced, the temperature inside the bolt kept increasing, which can be due to the inertial effect.

Then, the bolt was extracted and cooled with air.

SPRING 5

The bolt used was an M5. The spring was put in the furnace at time zero with *spring 4*. Then, the bolt was extracted and cooled by water quenching.

SPRING 6

The bolt used was an M6. The spring was put in the furnace at time zero with *spring 4*. Then, the bolt was extracted and cooled by water quenching.

Fig. 46. Obtained springs after the heat treatment

Regarding the cooling treatments, it must be point out that the water quenching is significantly faster that the air cooling. While with air cooling, around 3 minutes were needed to decrease the temperature from 450 to 110˚C; water quenching took around 18 seconds to cool down the spring from 415 to 38˚C. These results show that water quenching has an importantly higher efficiency.

2. Experimental tests

2.1 Test 0: Measurement of the residual strain

The aim of this preliminary test is to determine the residual strain in the spring after it is subjected to a thermomechanical cycle. The basis of this thermomechanical cycle is the Shape Memory Effect (SME); the spring is stretched under a certain load and then the load is released. By heating it to a temperature above A_f, the shape is recovered but a small deformation remains. This permanent deformation is what we call *residual strain*.

Before performing the test, some useful parameters were estimated. In order to know above which temperature it is necessary to heat the spring, we need to do an estimation of the austenitic finish temperature. From datasheet of the SmartFlex® wire we acquire the phase diagram and with its help we can obtain the transformation temperatures as a function of the applied stress. Considering the fact that in our test the transformation happens after the load is removed, i.e. at zero-stress, the spring is heated to 100-110˚C so that we make sure that the transformation is complete (fig. X.)

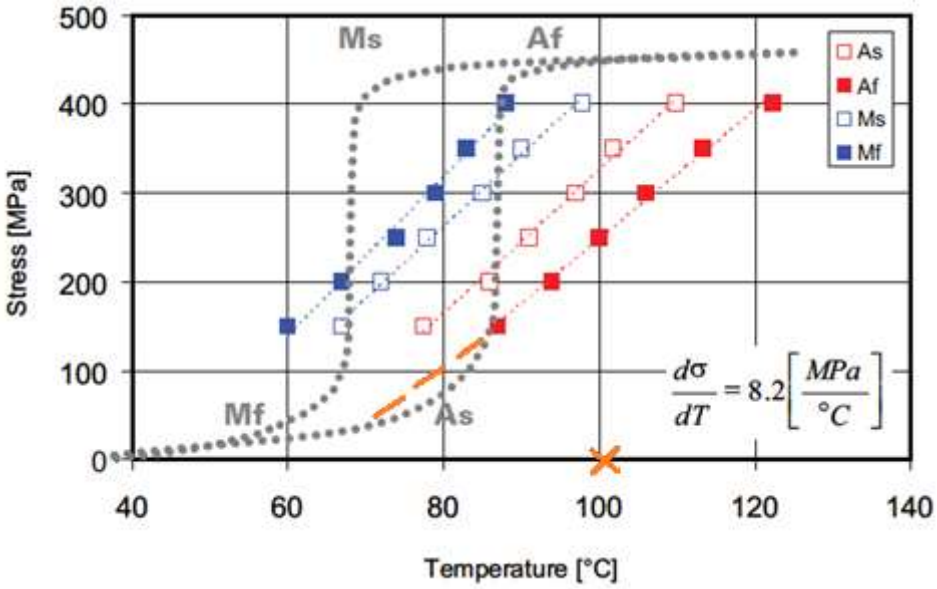

Fig. 47. Estimation of the austenitic finish temperature for the SmartFlex® wire

Other two useful properties to develop the mechanical tests in our springs are the maximum axial force that can be applied and the suggested force. From the datasheet of the wire, we know that:

- Diameter of the wire: $d = 0{,}4\ mm$
- Maximum force: $F_{max} = 75\ N$
- Suggested force: $F_{sug} = 21\ N$

Moreover, measuring with the caliber the external diameter of the springs, we obtain $D_{ext} = 4.95\ mm$, which means that the mean diameter of the spring is $D = 4{,}95 - 0{,}4 = 4{,}55\ mm$.

The normal tension at which a wire is subjected when an axial force F is applied is $\sigma = \frac{F}{\frac{\pi}{4}d^2}$. This normal tension can be translated into tangential tension in the spring by means of $\tau = \frac{\sigma}{\sqrt{3}}$. Finally, we can estimate the axial force it is necessary to apply to the spring in order to get this tangential stress: $F_{spring} = \frac{\pi\tau r^3}{2R}$, being r and R the radius of the wire and the spring, respectively. Following this procedure for the maximum force, we obtain:

$$\sigma_{max} = \frac{F_{max}}{\frac{\pi}{4}d^2} = \frac{75}{\frac{\pi}{4}0{,}4^2} = 596{,}8\ MPa$$

$$\tau_{max} = \frac{\sigma_{max}}{\sqrt{3}} = \frac{596.8}{\sqrt{3}} = 344{,}5\ MPa$$

$$F_{spring}^{max} = \frac{\pi\tau_{max}r^3}{2R} = \frac{\pi \cdot 344.5 \cdot \left(\frac{0.4}{2}\right)^3}{2\left(\frac{4.55}{2}\right)} = 1{,}9\ N = 193\ g$$

Similarly, for the suggested force, we get:

$$\sigma_{sug} = \frac{F_{sug}}{\frac{\pi}{4}d^2} = \frac{21}{\frac{\pi}{4}0{,}4^2} = 167{,}1\ MPa$$

$$\tau_{sug} = \frac{\sigma_{sug}}{\sqrt{3}} = \frac{167{,}1}{\sqrt{3}} = 96{,}5\ MPa$$

$$F_{spring}^{sug} = \frac{\pi \tau_{sug} r^3}{2R} = \frac{\pi \cdot 96{,}5 \cdot \left(\frac{0{,}4}{2}\right)^3}{2\left(\frac{4{,}55}{2}\right)} = 0{,}53\ N = 54\ g$$

The suggested force is then 28% of the maximum force.

To start the test, a preliminary step is done. It consists on heating the spring to 100˚C for 5 minutes in the oven in order to eliminate any possible deformation. The cooling is made by ambient air. Immediately, the test begins with the measure of the initial length of the spring (L0). Then, one of the ends is clamped to a hook made with a metal cable which will be hanging from an "L-shaped" support. On the other end of the spring, a constant weight is attached. The clamping is made with "the bolt-grooved nut system" previously used for the shaping treatment. The load is made with some metal pieces, bolts and nuts found in the laboratory which have been weighted to obtain the desired value. We decided to choose a value of this weight of 64.5 g, between the suggested and the maximum force. With the spring loaded, its new length is measured (L1). After, the load is removed. It can be observed that some of the deformation of the spring is recovered due to its elastic behaviour. The length of the deformed unloaded spring is also measured (L2). Finally, the spring is placed in the oven and heated up to 100˚C during 5 minutes and extracted. The final length is recorded (L3). All the measurements have been taken with a caliber of precision $\pm 0{,}01\ mm$, but as the last decimal position was oscillating at a reatively high speed, the measurements were recorded with a precision of $\pm 0{,}1\ mm$.

This procedure was repeated for 5 cycles with each spring. Four springs were tested: spring 1, spring 3, spring 4, spring 5. The characteristics of the shaping process for each of them are described previously. We decided to use spring 1 as a trial, since its shaping process was the less accurate due to the absence of the thermocouple. Also, the measurements of the length of spring 1 were the less precise because it was not very clear between which specific spires we were measuring. For the tests of spring 3, spring 4 and spring 5 two marks made with teflon were added in order to be more accurate in the measurements. Other remark to be done is that for springs 4 and 5, the temperature of the oven was slightly higher: 110˚C. In addition, in order to improve accuracy, during the test of spring 5, some time was taken before taking the measurement of L1 and after loading. To that aim, 1 minute was counted right after the spring was loaded so that the deformation was stabilized. Regarding the test of spring 3, in the sixth cycle, a load very close to the maximum force was applied: 190 g. The deformation was significantly high and an important residual strain after heating was observed.

Fig. 48. Measurement of the initial length (L0) of spring 1. Close-up to the clamping system on the side of the hook; the end of the wire passes through the groove machined on the nut and compressed but another nut.

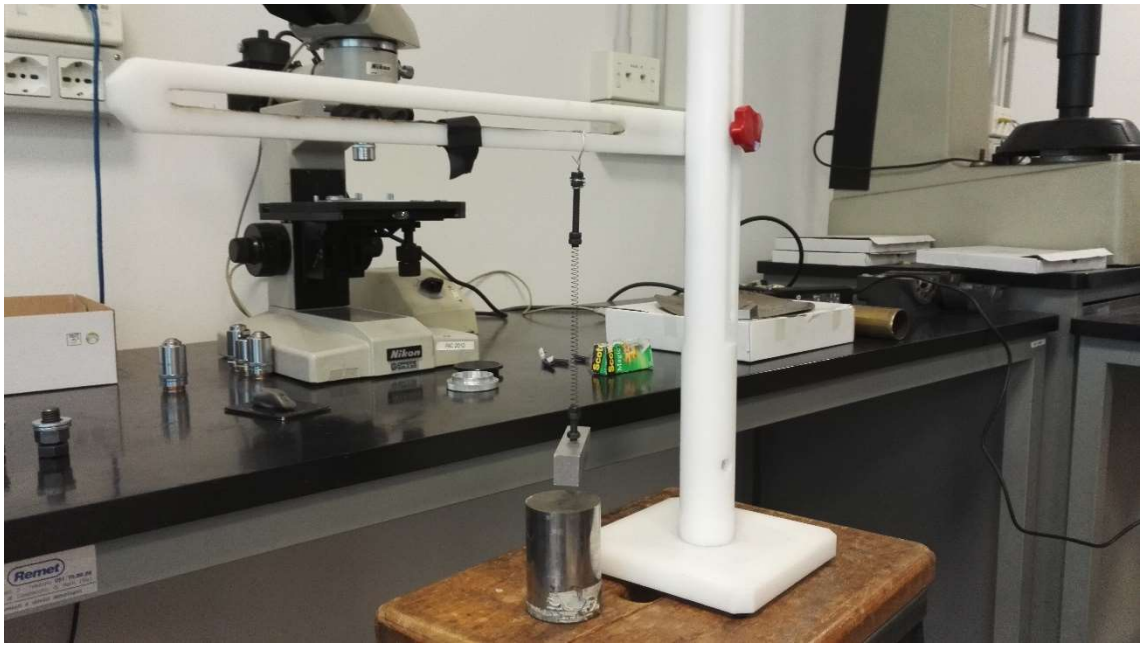

Fig. 49. Spring 1 hanging from the support with the weight attached. Measurement of L1.

Fig. 50. Measurement of L2 of spring 1

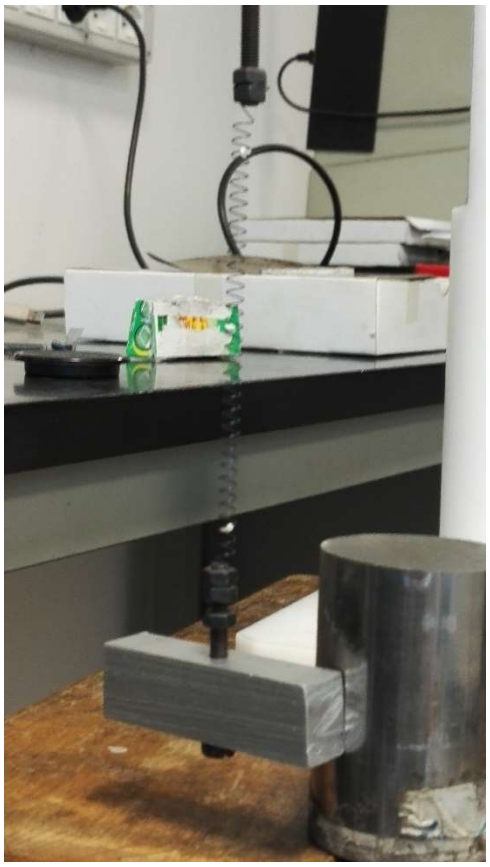

Fig. 51. Spring 3 loaded. The two marks made with teflon can be observed (two white points)

Fig. 52. Spring 3 loaded with the maximum weight. Significant deformation observed.

2.1.1 Results of test 0

The measured lengths for each spring and each thermomechanical cycle are presented in the following charts. Moreover, three different strain levels are calculated:

- $\varepsilon_1 = \frac{L1-L0}{L0} \cdot 100\ (\%)$
- $\varepsilon_2 = \frac{L2-L0}{L0} \cdot 100\ (\%)$
- Residual strain $\varepsilon_3 = \frac{L3-L0}{L0} \cdot 100\ (\%)$

	Cycle	L0 (mm)	Weight (g)	L1 (mm)	ε_1 (%)	L2 (mm)	ε_2 (%)	L3 (mm)	ε_3 (%)
Spring 1	1	31,6	64,5	106,5	237,03	58,0	83,54	30,4	-3,80
	2	30,4	64,5	122,4	302,63	68,7	125,99	29,5	-2,96
Spring 3	1	22,9	64,5	84,4	268,56	47,2	106,11	22,5	-1,75
	2	22,5	64,5	89,5	297,78	52,7	134,22	22,3	-0,89
	3	22,3	64,5	93,0	317,04	55,9	150,67	22,3	0,00
	4	22,3	64,5	91,7	311,21	57,9	159,64	22,3	0,00
	5	22,3	64,5	92,6	315,25	59,1	165,02	22,4	0,45
	6	22,4	190,0	324,2	1347,32	287,0	1181,25	41,0	83,04
Spring 4	1	26,3	64,5	98,3	273,76	57,0	116,73	25,7	-2,28
	2	25,7	64,5	99,9	288,72	60,8	136,58	25,5	-0,78
	3	25,5	64,5	97,9	283,92	58,2	128,24	25,6	0,39
	4	25,6	64,5	97,3	280,08	56,9	122,27	24,7	-3,52
	5	24,7	64,5	97,0	292,71	56,8	129,96	26,5	7,29
Spring 5	1	17,6	64,5	67,2	281,82	41,2	134,09	17,8	1,14
	2	17,8	64,5	67,6	279,78	40,6	128,09	17,5	-1,69
	3	17,5	64,5	69,7	298,29	41,7	138,29	17,7	1,14
	4	17,7	64,5	68,5	287,01	42,1	137,85	17,5	-1,13
	5	17,5	64,5	68,9	293,71	41,9	139,43	17,5	0,00

Table 1. Experimental results of test 0

The row of data in blue corresponds with the loading of spring 3 to the maximum weight.

The number of coils of each spring was also counted, obtaining:

	Number of coils n
Spring 3	27
Spring 4	32
Spring 5	21

Table 2. Number of coils of each tested spring

2.1.2 Conclusions of test 0

The first conclusion that can be noted from this test is the unconsistency of some of the results. From the theoretical fundamentals we know that, when a SMA component is initially subjected to a thermomechanical cycle, not all the deformation is recover but there is a small level of strain that remains. Due to these permanent changes in the microstructure, when the material is subdued to several thermomechanical cycles, some small strain is remaining. This additional strain decreases with each cycle until the total strain stabilizes. In our test, when measuring the final length L3 of our spring, in some cases it is smaller than the initial length, giving a negative residual strain. In order to try to solve these unconsistent results, we placed again the spring in the oven for a couple more minutes, since the reason of these results could be that the spring was not heated enough and therefore, the transformation into austenite is not complete and not all the deformation is recovered. After this adjustment, there were no significant changes in the results. Hence, the error stays in the lack of accuracy of the measurement, specially regarding the

human errors. It also can be pointed out that, theoretically, the strain should increase for each cycle (since 5 cycles are not enough for the response to stabilized) but in our experimental test that increasing tendency is not very clear in some cases.

The results are plotted in the following graphs. It can be observed that the tendency of increasing strain is the most accurate in spring 3.

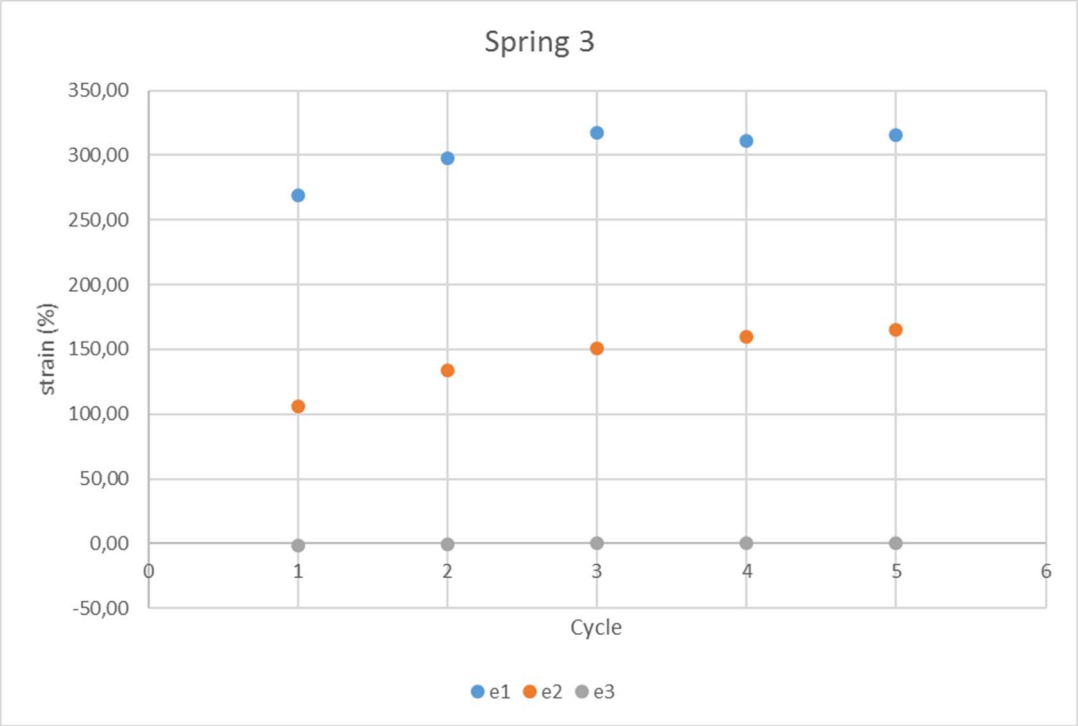

Fig. 53. Variation of the different strains with each cycle in spring 3

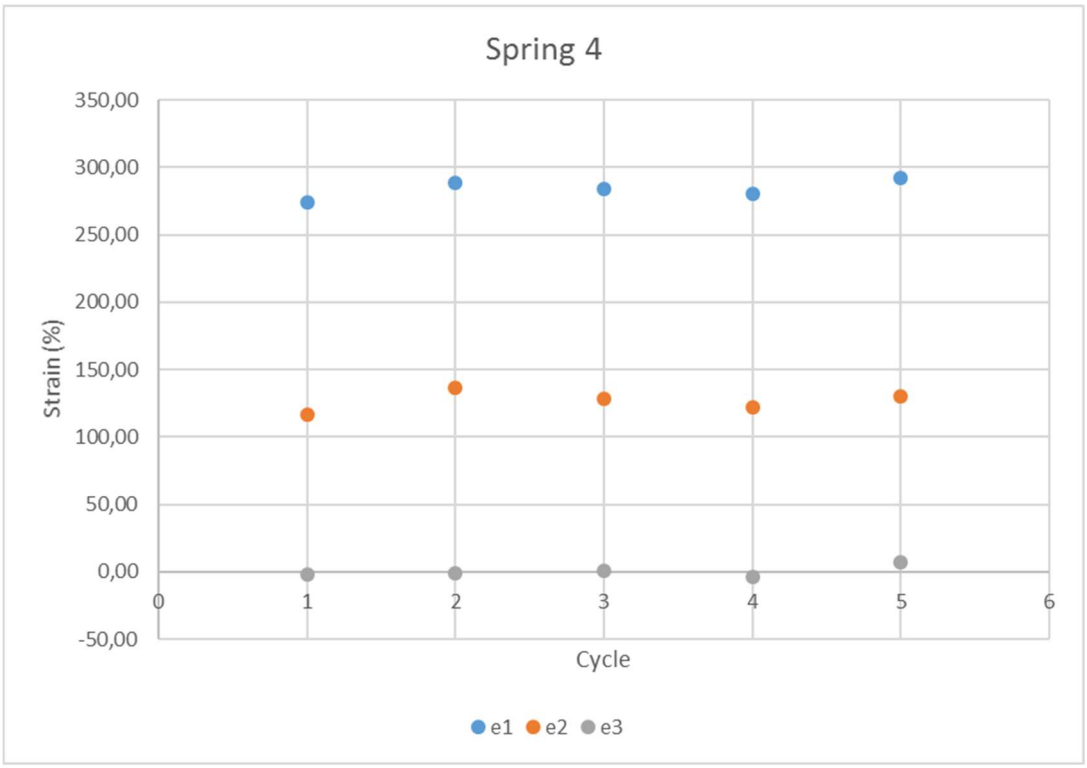

Fig. 54. Variation of the different strains with each cycle in spring 4

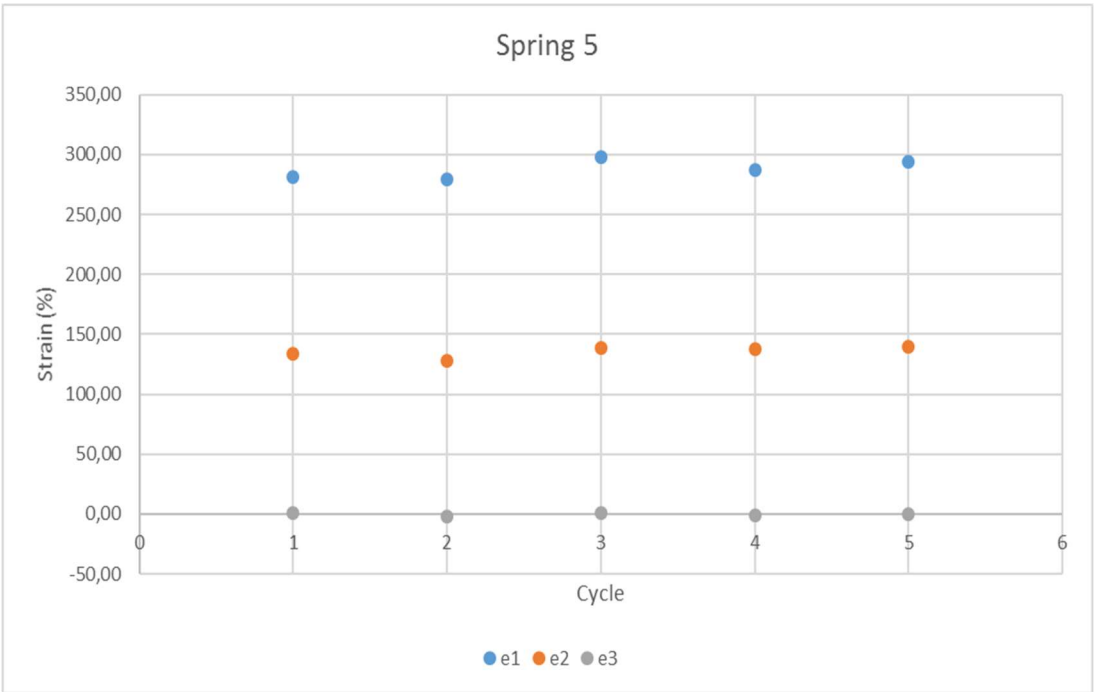

Fig. 55. Variation of the different strains with each cycle in spring 5

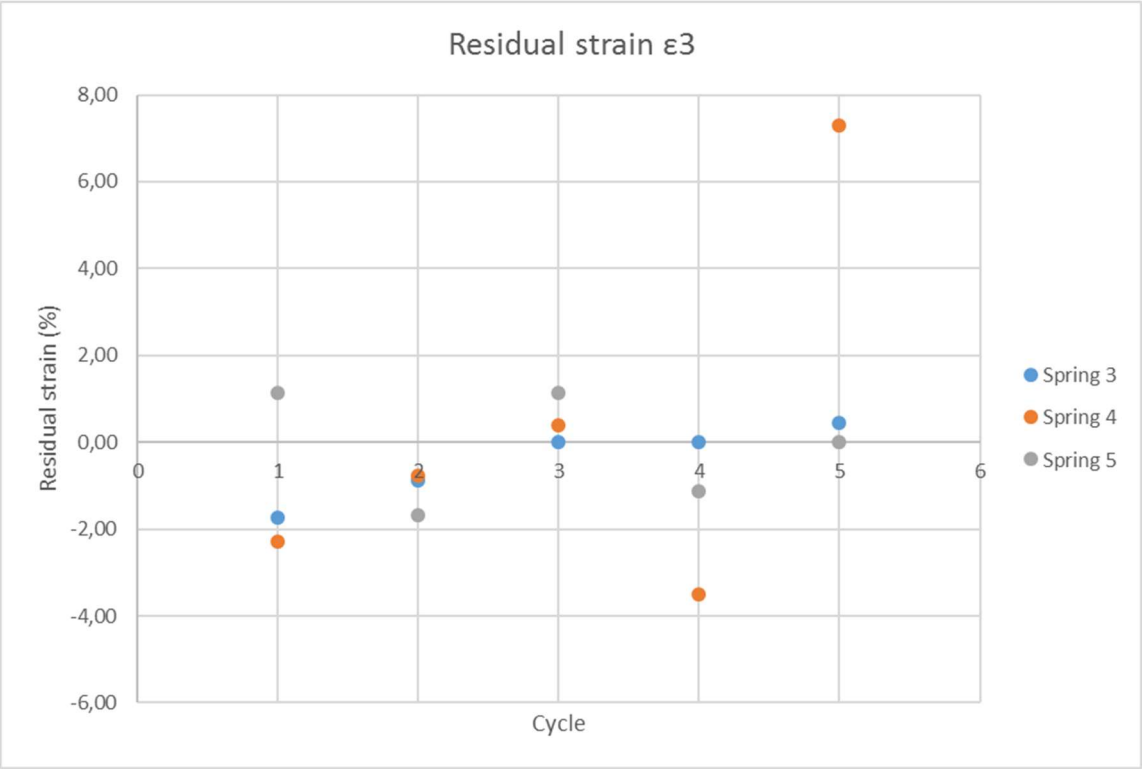

Fig. 56. Variation of the residual strain with each cycle and for each spring

From the obtained data, some other parameters can be extrapolated:

- The constant of the spring, considering the elongation when the load is applied:

$$k_1 = \frac{F}{L1 - L0}$$

  As the length of the spring (number of coils) influences this constant, we calculate also k_1 per coil, dividing by the total number of coils.

- The constant of the spring, considering the elastic recovering when the load is relased:

$$k_2 = \frac{F}{L1 - L2}$$

  This second constant is also divided by the number of spires in order to know the constant per coil.

- The shear modulus and elastic modulus of martensite, G_M and E_M.

  We know that the deflection of the spring (in hot or cold state) is $\delta = \frac{8FD^3n}{Gd^4}$, being F the axial force applied. In our test, this defletion can be calculated as $\delta = L1 - L2$, since it is the elastic recovering when we are in detwinned martensitic state. With these relations, we are able to obtain the shear modulus in the cold state. Knowing that $E = 2G(1 + \upsilon)$, with υ the Poisson's ratio of Nitinol, $\upsilon = 0.3$, we can also determine the elastic modulus in the cold state.

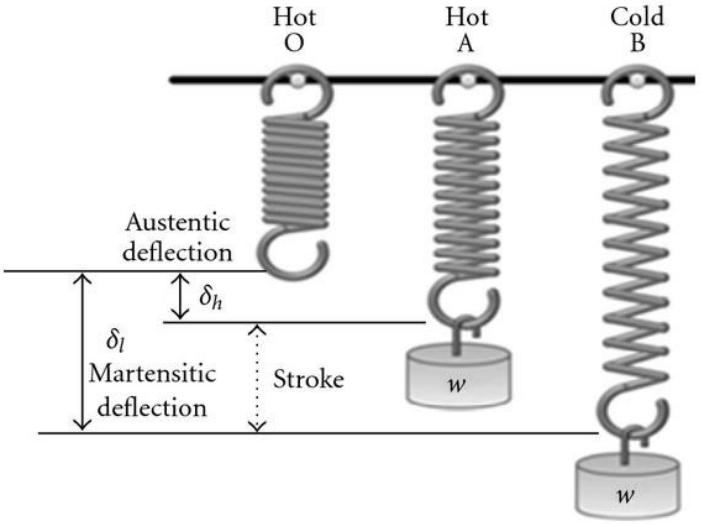

Fig. 57. Deflection of a spring in the martensitic and austenitic states and stroke of the actuator

These calculations are collected in the following chart. When performing the mean value of k_1 for spring 3, the value of 0,01029 N/mm was not considered since it is considerably deviated from the other values; either the value of cycle 6. Regarding the calculation of the elastic modulus of spring 3, the values corresponding to the sixth cycle were not taken into consideration either for the previous reason.

	Cycle	$k_1\ (N/mm)$	$k_1/_{nºcoils}\ (N/mm \cdot coil)$	$k_2\ (N/mm)$	$k_2/_{nºcoils}\ (N/mm \cdot coil)$
Spring 3	1	0,01029	0,00038	0,01701	0,00063
	2	0,00944	0,00035	0,01719	0,00064
	3	0,00895	0,00033	0,01706	0,00063
	4	0,00912	0,00034	0,01872	0,00069
	5	0,00900	0,00033	0,01889	0,00070
	6	0,00618	0,00023	0,05010	0,00186
	Mean	0,00913	0,00034	0,01777	0,00066
Spring 4	1	0,00879	0,00033	0,01532	0,00048
	2	0,00853	0,00032	0,01618	0,00051
	3	0,00874	0,00032	0,01594	0,00050
	4	0,00882	0,00033	0,01566	0,00049
	5	0,00875	0,00032	0,01574	0,00049
	Mean	0,00873	0,00032	0,01577	0,00049
Spring 5	1	0,01276	0,00047	0,02434	0,00116
	2	0,01271	0,00047	0,02344	0,00112
	3	0,01212	0,00045	0,02260	0,00108
	4	0,01246	0,00046	0,02397	0,00114
	5	0,01231	0,00046	0,02344	0,00112
	Mean	0,01247	0,00046	0,02355	0,00112

Table 3. Calculations of the spring constants

	Cycle	F (N)	$\delta\ (mm)$	$G\ (GPa)$	$E\ (GPa)$
Spring 3	1	0,63275	37,2	13,519	35,149
	2	0,63275	36,8	13,666	35,531
	3	0,63275	37,1	13,555	35,243
	4	0,63275	33,8	14,879	38,684
	5	0,63275	33,5	15,012	39,031
	6	1,86390	37,2	39,822	103,538
	Mean			14,126	36,727
Spring 4	1	0,63275	41,3	14,432	37,522
	2	0,63275	39,1	15,244	39,633
	3	0,63275	39,7	15,013	39,034
	4	0,63275	40,4	14,753	38,358
	5	0,63275	40,2	14,826	38,549
	Mean			14,854	38,619
Spring 5	1	0,63275	26,0	15,044	39,114
	2	0,63275	27,0	14,487	37,665
	3	0,63275	28,0	13,969	36,320
	4	0,63275	26,4	14,816	38,521
	5	0,63275	27,0	14,487	37,665
	Mean			14,560	37,857

Table 4. Calculation of the shear and elastic modulus of martensite

From the performed calculations, it can be observed that the higher the number of coils of the spring, the lower the constant k_1. This means that the higher the number of coils, the higher the deformation of the spring when a load is applied. The constant k_2 also decreases when the number of coils is higher, which means that the recovered length when the load is released is increases.

Considering the calculated shear and elastic moduli, the values obtained seem quite accurate since the elastic modulus of martensite in Nitinol must be in the range of 28-40 GPa. Regarding the behavior of the spring 3 in the sixth cycle, when a load closed to the maximum was applied, the calculated shear and elastic moduli significantly vary from the expected result since we were working in a very advanced plastic zone of the spring.

2.2 Test 1: Measurement of the variation of the force with time at constant current and constant strain

The objective of this test is to measure how the force exerted by the spring varies with time when a constant current is applied and the deformation of the spring is also constant.

2.2.1 Experimental set-up

Our set up is composed by the following elements:

- **Testing bench:** It has to directions of displacement; longitudinal and transversal, which are regulated by means of two wheels. The base of the bench has different rails along

its length where one of the clamps of the spring is attached. This element is made with an “L-shaped” metal sheet, fixed to one of the rails with a bolt-nut set.

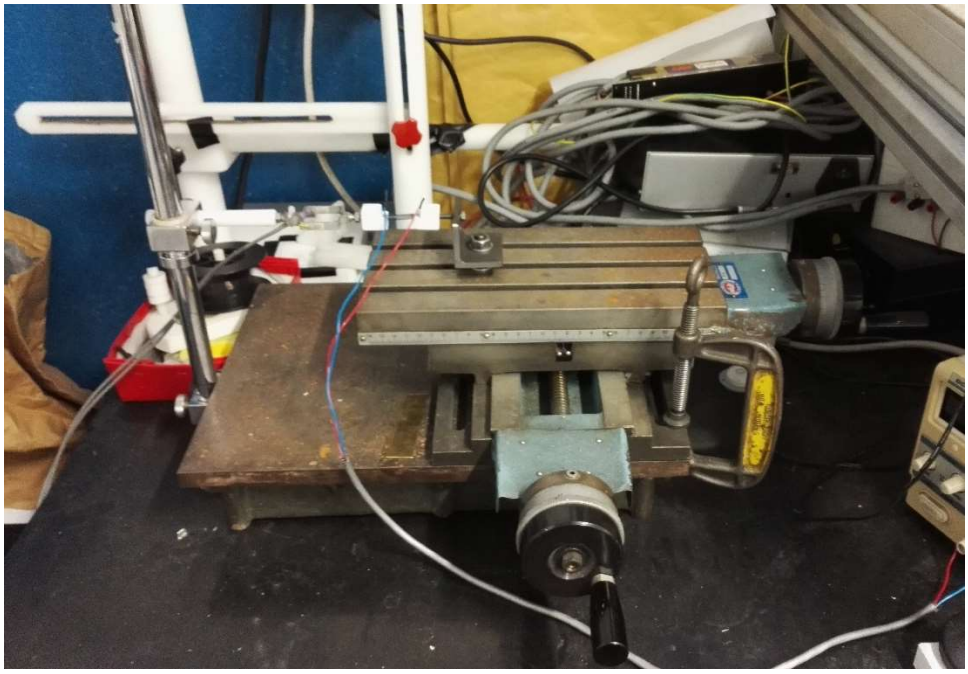

Fig. 58. Testing bench

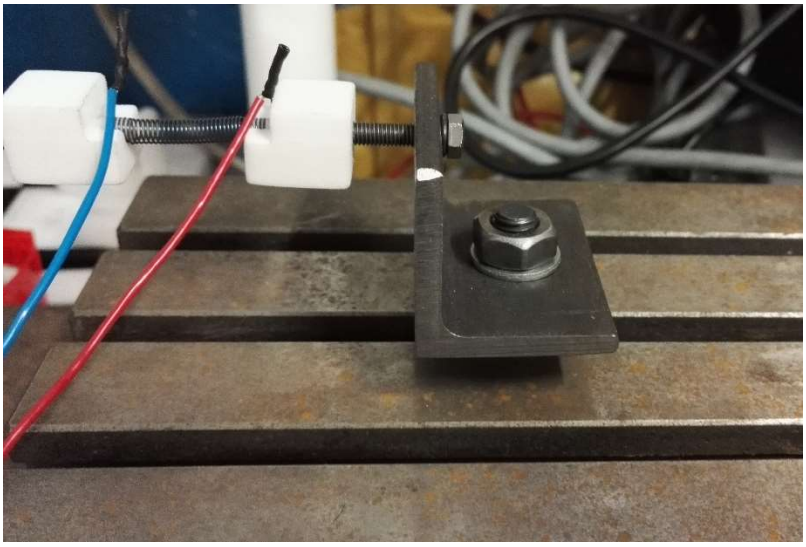

Fig. 59. Close-up of the clamping element to the bench

- Load cell: The load cell holds from a support and is fixed to the other clamp of the spring (Fig. 58). It has extensiometers capable to measure the deformation and, therefore, the force. The values of the deformation are shown in με and monitored by means of an Strain Indicator and Recorded, which is connected to the load cell and to a computer.

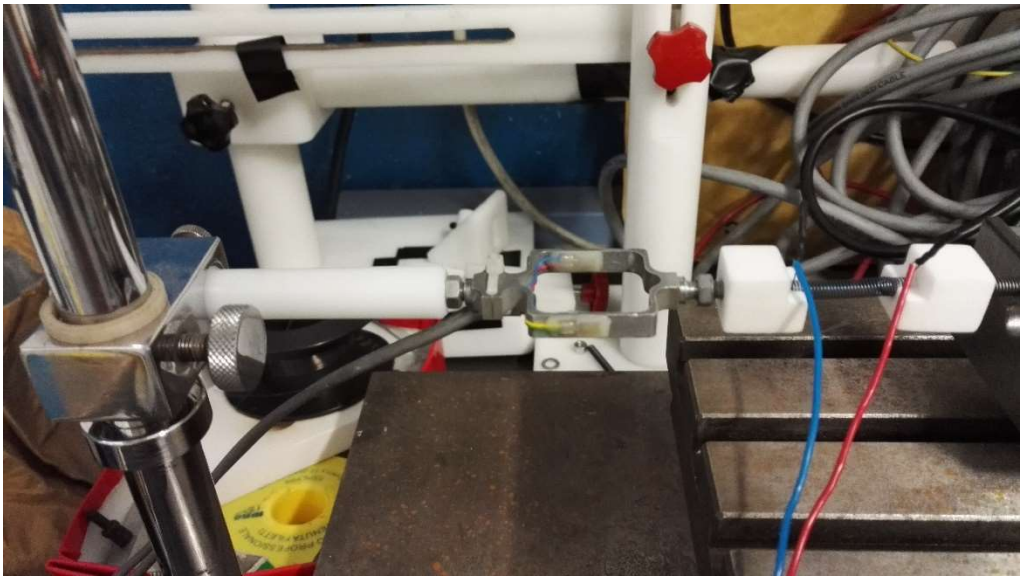

Fig.60. Close-up of the load cell

Fig. 61. Strain Indicator and Recorder

Fig. 62. Command panel of the load cell (experimento anterior)

- Spring clamping system: The clamping system of SMA elements (wires and springs), when performing tests or when applying them to any other application, is very important in order to obtain accurate and consistent results. Due to the fact that the SMA components have to be heated by means of a current up to their austenitic transformation temperature (in our case, up to 100˚C), the material used for the clamping system must be a thermal and electrical insulator. A deficient insulation may lead to a non-uniform heat distribution. Hence, we may have different phases in the several sections of the spring; martensite in the area near the clamping since some of the heat is dispersed through the clamps and thus, the temperature decreases, and austenite is the center part of the spring. Therefore, the material we chose to make both clamps is PTFE (teflon), whose properties are:
    - Melting point: 327˚C
    - Yield strength: 23 MPa
    - Thermal conductivity: $0.25\ W/(m \cdot K)$
    - Electrical conductivity: $10^{-25} - 10^{-23}\ S/m$

  The thermal and electrical conductivity values are low, which means that it will fulfill the function of insulating. In addition, its melting point is high enough for our experiment, since we only need to heat the specimen up to 100-110˚C.

  The design of the clamping system consists on a cubic block with a hole passing through. The hole is threaded in one side and flat on the opposite side. The other component of the clamping system is a bolt. The two elements are made with teflon and the dimension of both, hole and bolt, is M5, which is the size of the bolts we used to shape the springs. The spring is coiled around the bolt and introduced in the flat part of the hole. The upper part of the flat side of the hole is cutted, so that part of the bolt with the spring is exposed and accessible and we are able to do the electrical connection. One of the clamps is connected to the load cell, which is screwed on the threaded part of the hole of the block. The other clamp is attached to the bench by screwing the “L-shaped” metal sheet to the threaded part of the hole of the teflon part.

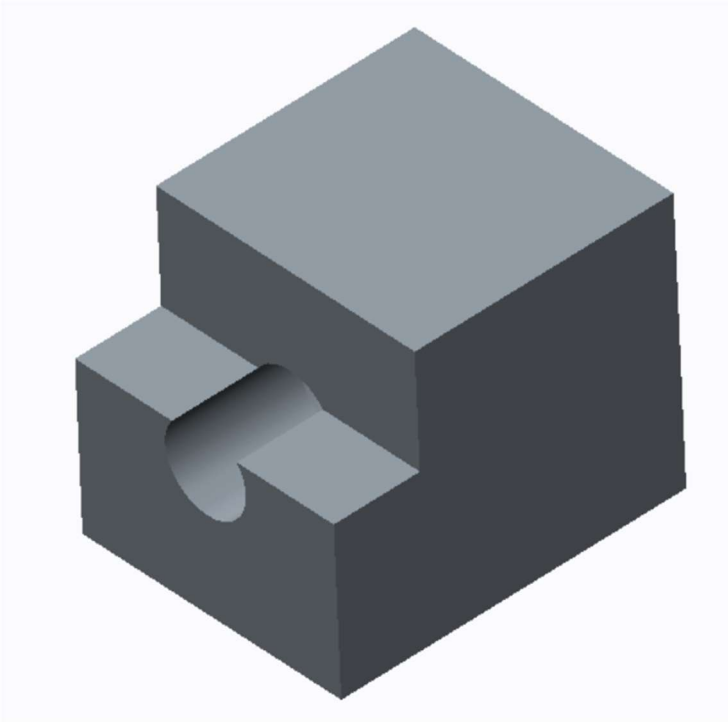

Fig. 63. Clamping system: Creo Parametric model if the teflon block

Fig. 64. Clamping system: Creo Parametric model if the teflon bolt

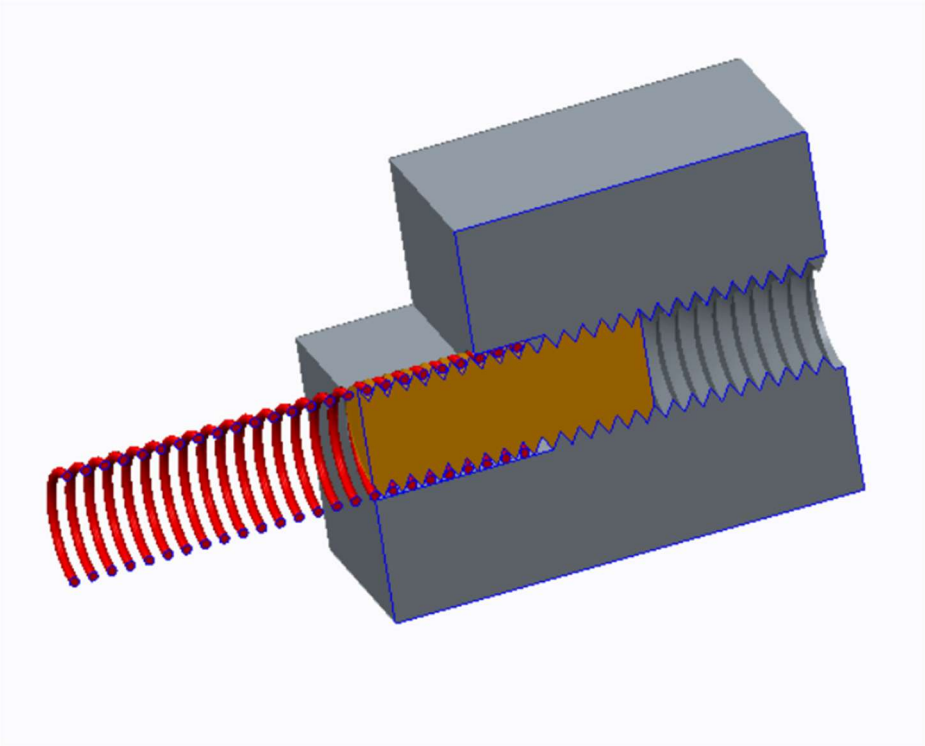

Fig. 65. Clamping system: Creo Parametric model of the assembly

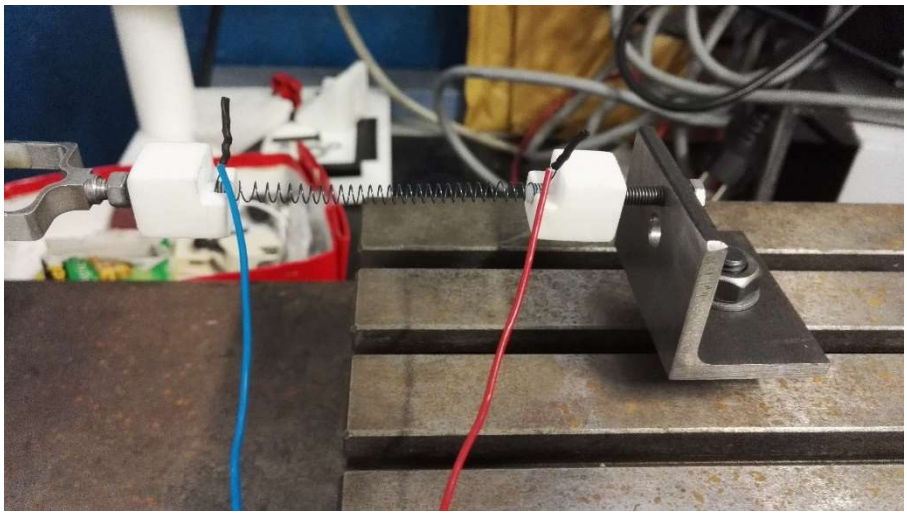

Fig. 66. Close-up of the clamping system

With this clamping system, a significant improvement is achieved, regarding the system used in previous experiments with SMA springs. The clamping system utilized in the prior test was made with a plastic cylindrical piece and a conventional metal bolt. The spring was attached to the bolt with a hook. Due to the high temperature of the spring, the bolt bent, since its yield strength was not high enough at the working temperature. This effect was slightly varying the fixed elongation of the spring.

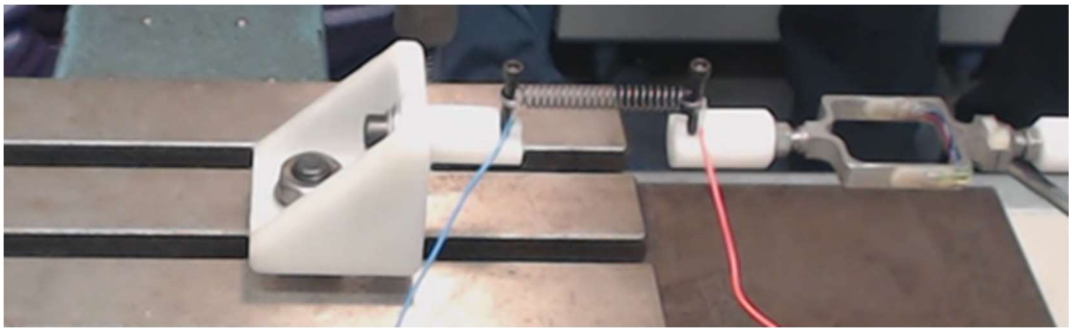

Fig. 66. Clamping system used in previous tests (experimento anterior)

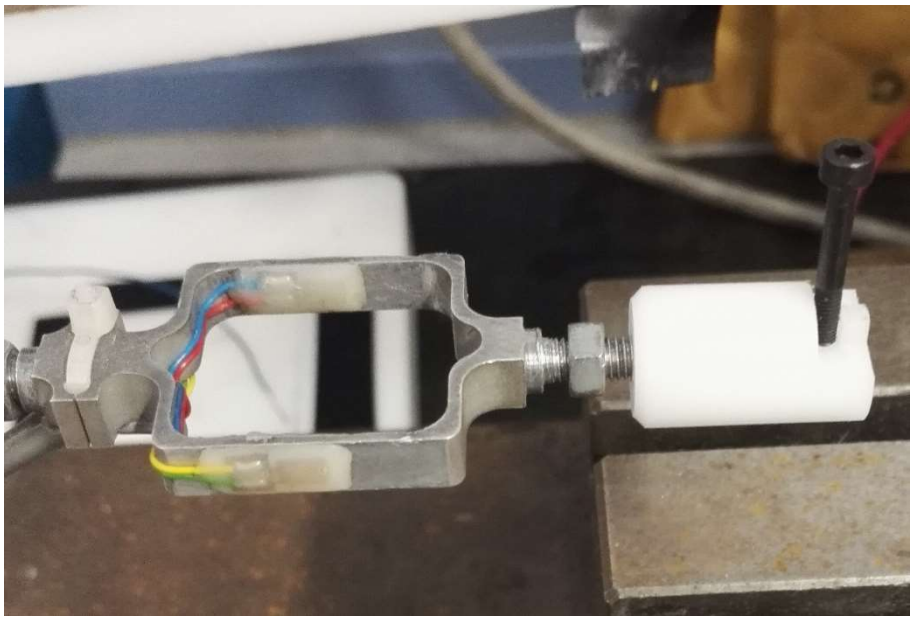

Fig. 67. Close-up to the clamping system used in previous tests

- Power supply: To apply the desired current to the spring. In the power station, we vary the voltage in order to regulated the supplied current.
- Thermocamera: It is used to determine the maximum temperature in the spring during the test, so that we are able to estimate when the austenitic transformation is occurring. In addition, the images recorded with the thermocamera allow us to analyze the distribution of temperature along the spring. When performing the first test, we observed that the maximum temperature was detected in the connections of the spring with the electrical cables and thus, the signal of the maximum temperature displayed by the thermocamera did not correspond to the temperature in the spring, but the temperature in this connections. Hence, to improve the accuracy of the acquired data, we covered with black tape the previously mentioned connections so that these high temperatures were not detected by the thermocamera. Moreover, to obtain a better image, a black panel was placed immediately behind the set-up. The emissivity is set to 0,74.

2.2.2 Calibration of the load cell

The objective of this test is to determine if the load cell is working properly and if the data of the force obtained are consistent. To this aim, the lengths recorded in Test 0 after loading the spring are applied and the deformation values measured with the load cell in με are compared to the weight used in Test 0. In order to do that, the lengths measured in Test 0 must be translated to

actual lengths that we need to stretch the spring in the current set up. This depends on the number of active coils. For this calibration test we use **spring 4** and as initial length we consider the values of the fifth cycle of Test 0. The procedure consists on dividing the length by the number of active spires in Test 0 and multiply this value by the number of active spires in the current set up.

	Nº of spires	*Initial length L0 (mm)*	*L0/nºspires (mm/spire)*
Test 0	32	26,5	0,828
Current set-up	28	23,2	0,828

Table 5. Calculation of the initial length for the experimental set-up of test 1 for spring 4

Knowing that the previous calibration of the load cell follows a linear behavior such that 1000 g = 304 με, the equivalent values of the force in grams obtained for each length are shown in the following table. L1 stands for the values of the length in Test 0, while L1' stands for the equivalent length we need to apply in the current set-up.

L1 (mm)	*mm/ spire*	*L1' (mm)*	*Deformation (με)*	*F (g)*
98,3	3,072	86,0	7	23,0
99,9	3,122	87,4	7	23,0
97,9	3,059	85,7	7	23,0
97,3	3,041	85,1	6	19,7
97,0	3,031	84,9	6	19,7

Table 6. Force values displayed by the load cell for different lengths

It can be noted that the values of the force given by the load cell do not correspond to the weight applied in Test 0 (64,5 g). Therefore, it is necessary to determine the new relation με-g for our experiment. Before that, we checked that the force values obtained with the load cell were following a linear relation with the elongation during the elastic behavior of the spring. We considered the value of L2 of Test 0 for the fifth cycle and increased it progresively up to L1, recording the force levels. We can observed that the displayed values follow a linear tendency and therefore, the load cell is working properly.

	Nº of spires	*L2 (mm)*	*L0/nºspires (mm/spire)*
Test 0	32	56,8	1,775
Current set-up	28	49,7	1,775

Table 7. Calculation of the equivalent length L2 for the experimental set-up of test 1 for spring 4

L (mm)	*Deformation (με)*
49,7	1
59,7	3
69,7	5
79,7	6
84,9	7

Table 8. Values of the force displayed by the load cell for different elongations in the elastic behavior of spring 4

For the new calibration, the load cell was subjected to different weights with known values and the values of the deformation were recorded.

Weight (g)	*Deformation (με)*
64,82	5
101,47	8
106,97	9
117,95	10
189,85	15
298,43	24

Table 9. Calibration of the load cell for spring 4

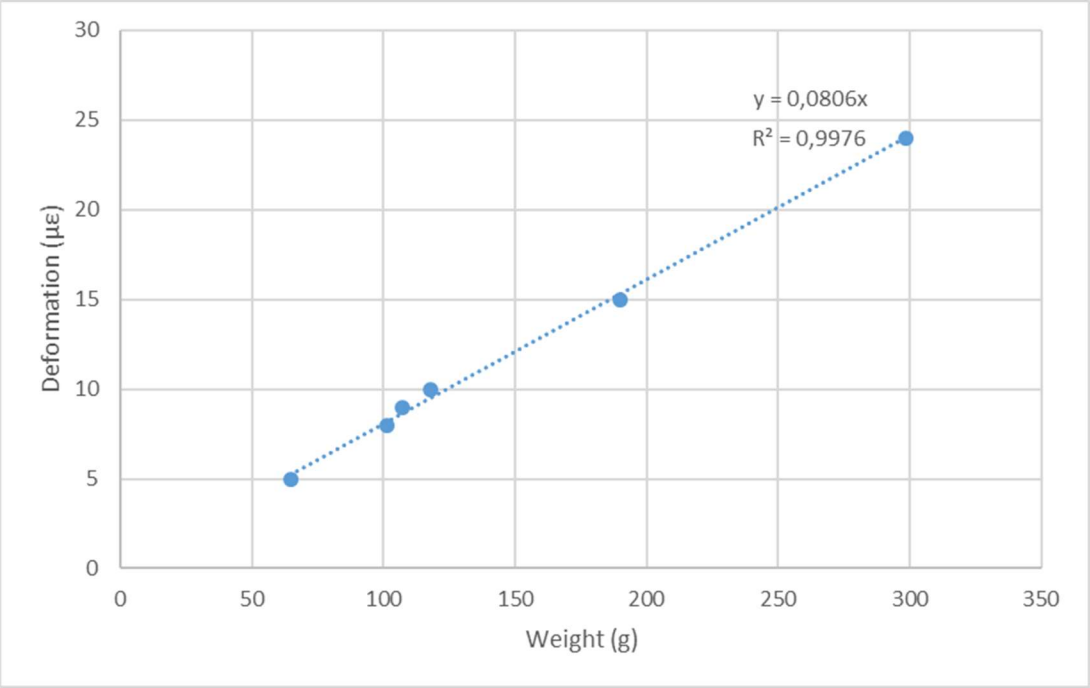

Fig. 68. Calibration of the load cell for spring 4: με-g relation

The calculated calibration of the load cell for our set-up with spring 4 is $Deformation(\mu\varepsilon) = 0{,}0806 \cdot F(g)$.

When performing tests on **spring 5**, the load cell was calibrated again in order to ensure the obtained values of the force were correct. To this purpose, we repeated the last step mentioned before: apply known weights to the load cell and record the values of the deformation.

Weight (g)	*Deformation (με)*
0	-6
64,77	-1
189,77	9
298,37	18
384,37	25

Table 10. Calibration of the load cell for spring 5

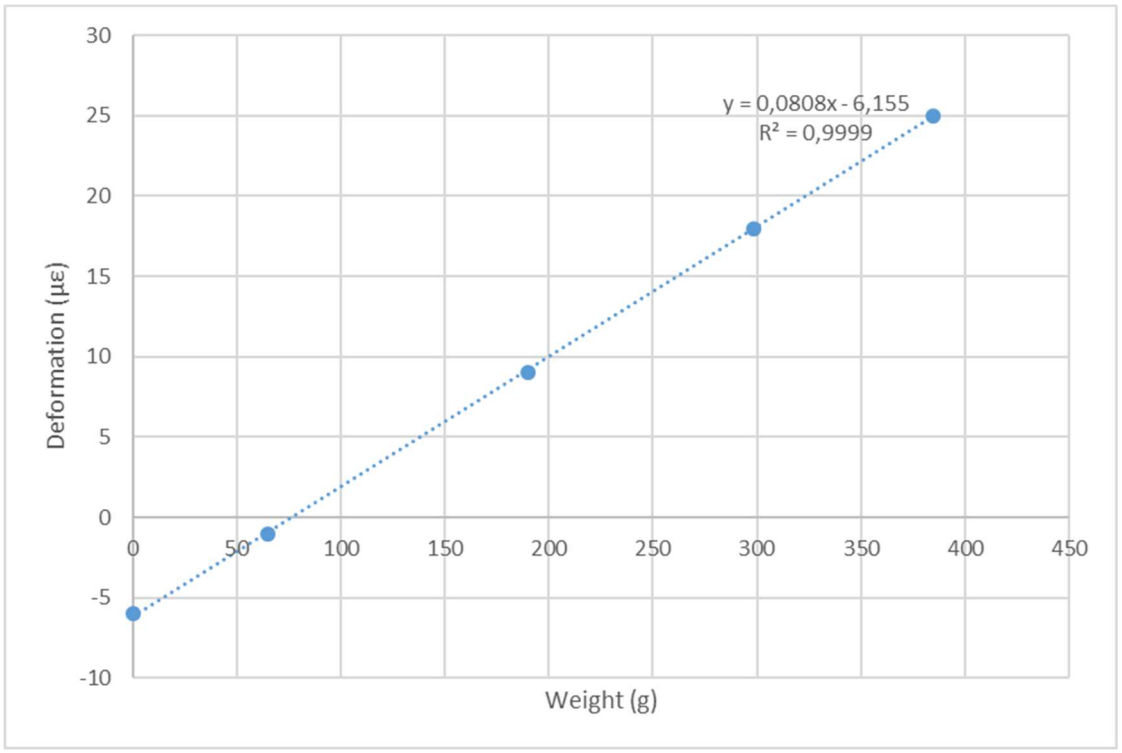

Fig. 69. Calibration of the load cell for spring 5: με-g relation

We can observe that, even if the calibration for spring 5 does not intersect with the (0, 0), the slope of the graph for spring 4 and 5 are very similar (0,0806 and 0,0808; respectively). Since during experiments on spring 5, the load cell was set to zero deformation when elongation of the spring was applied, we can use the same calibration of the load cell in the tests of both springs.

2.2.3 Procedure of test 1

The procedure of this test consists on stretching the spring a certain deformation and clamped it in both ends. A constant current is applied to the spring by means of a power supply. In this power supply we regulate the voltage in order to obtain the desired value of the current. Simultaneosly to switching on the power supply, the evolution of the deformation in the load cell starts to be

recorded. Also the cooling process is recorded, so that we can observed how the deformation in the load cell decreases. To this aim, the power supply in switched off when we notice that the deformation and temperature have reached their maximum value and both are stable. During the cooling process, when we observe that the deformation got to its minimum value and the temperature is low enough, the recording is stopped and the individual test is finished. This procedure is repeated for four different values of the current. In addition, further tests are performed for three elongations of the spring. All this experiments were carried out in springs 4 and 5.

Previously to the start of test 1 and using spring 4, a test to estimate the activation current was performed. The spring was stretched to a length L = 84,9 mm, which corresponds to L1 in the 5th cycle of test 0, and subjected to a current that was increased progresively. Current, voltage, temperature and deformation data were collected in a few points. The temperature recorded was the maximum temperature displayed in the thermocamera, which does not correspond to the temperature of the spring but the temperature in the connections, as mentioned before. The results are collected in the table below.

Current (A)	*Voltage (V)*	*Temperature (˚C)*	*Deformation (με)*
0,42	1,7	38,4	
0,59	2,3	61,5	
0,76	2,9	78,5	6
1	3,8	139	12

Table 11. Preliminary test on spring 4 in order to estimate the activation current

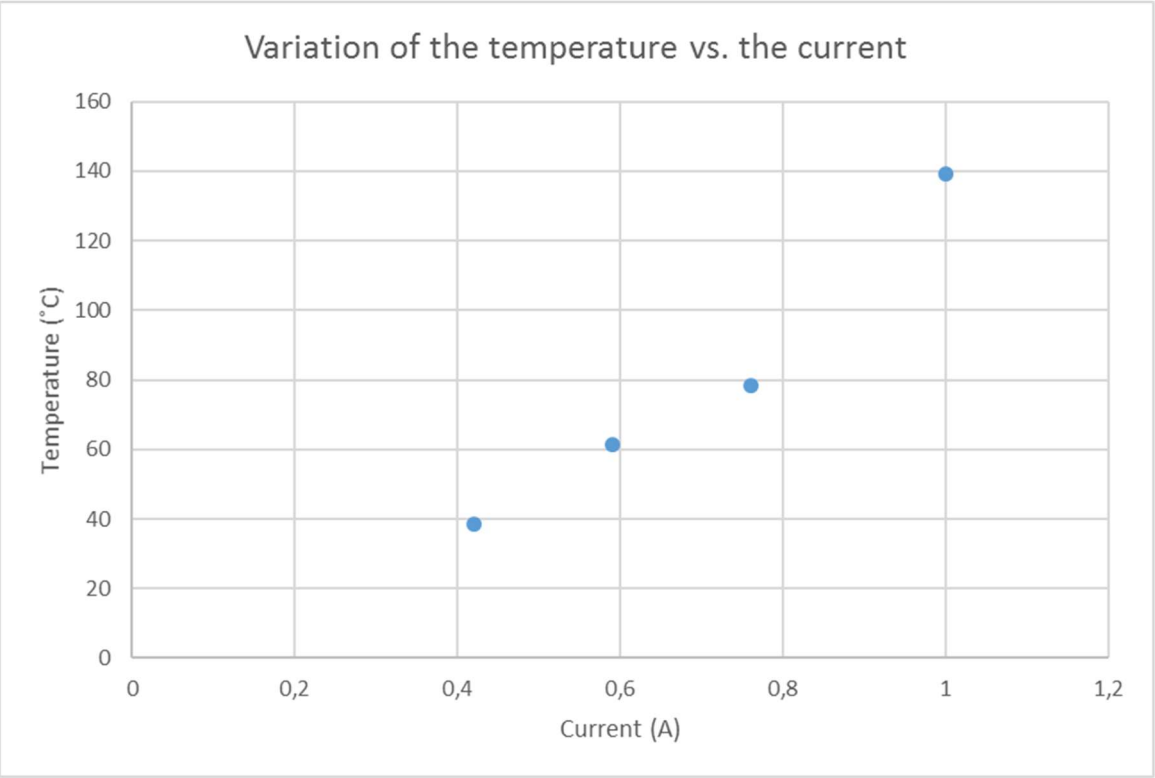

Fig. 70. Graphical representation of the variation of the temperature with the applied current in spring 4

By observing the behavior of the spring, we noted that the shape was recovering when 1 A was applied. Therefore, this is the activation current and further tests will be carried out at currents equal to 1 A and higher.

2.2.4 Results of test 1 for spring 4

Tests on spring 4 were performed for three different elongations: the first one corresponding to the length L1 of test 0, L = 84,9 mm; the second one 4/3 of 84,9 mm, L = 113,2 mm; and the last one, a maximum length set to L = 157,0 mm. The initial length of spring 4 is 23,2 mm.Each of these elongations was tested at four different currents: 1: 1,25; 1,5 and 2 A (except from the length of 157,0 mm that was only tested at 1 and 1,25 A). Smaller strains than the chosen ones are not possible since the load cell is not accurate enough. The results of these experiments are shown next.

TEST 1:

Length (mm)	84,9
Current (A)	1
Voltage (V)	3,8

Maximum deformation, reached at t = 66 s: 9 $\mu\varepsilon$

Maximum force: 111,66 g

The length of the spring corresponds to the length of test 0 when the load is applied (L1) for the fifth cycle.

Cooling was not recorded in this test.

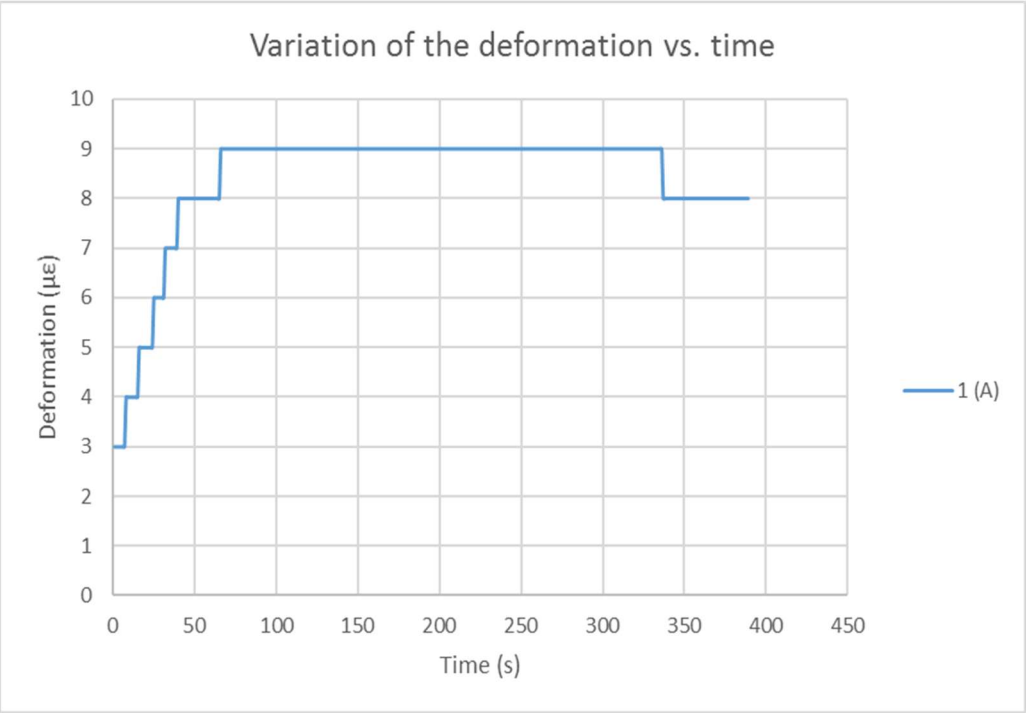

Fig. 71. Test 1: Variation of the deformation with time for a constant current and elongation of spring 4, 1 A and 84,9 mm, respectively.

TEST 2:

Length (mm)	84,9
Current (A)	2
Voltage (V)	8

Maximum deformation, reached at t = 4 s: $11\ \mu\varepsilon$

Maximum force: $136{,}48\ g$

Cooling was not recorded in this test.

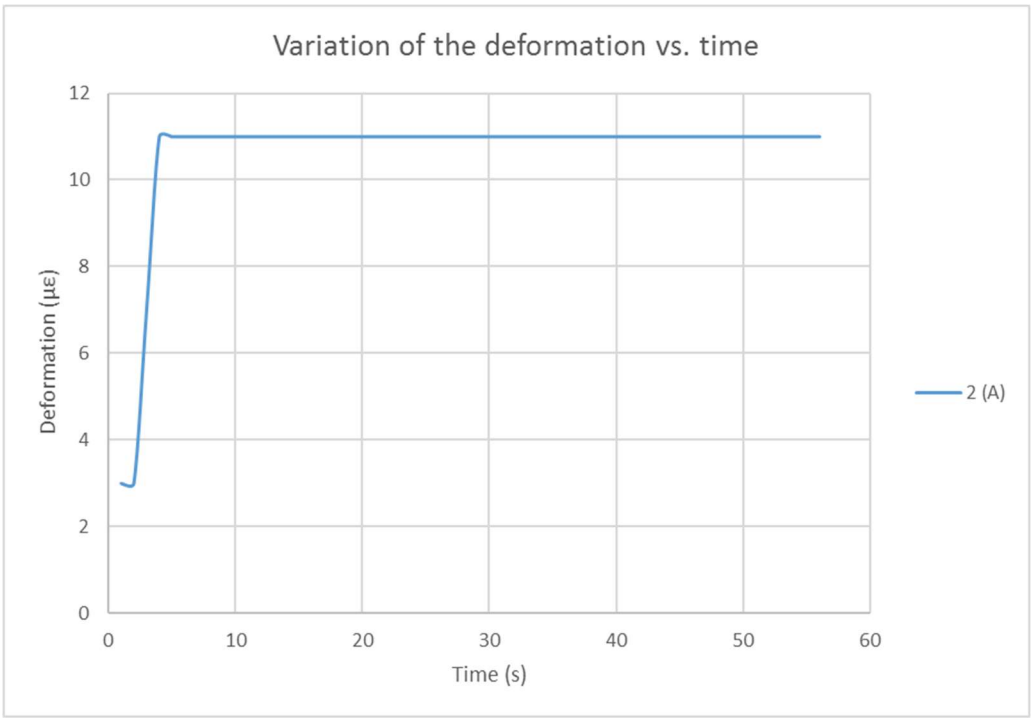

Fig. 72. Test 1: Variation of the deformation with time for a constant current and elongation of spring 4, 2 A and 84,9 mm, respectively.

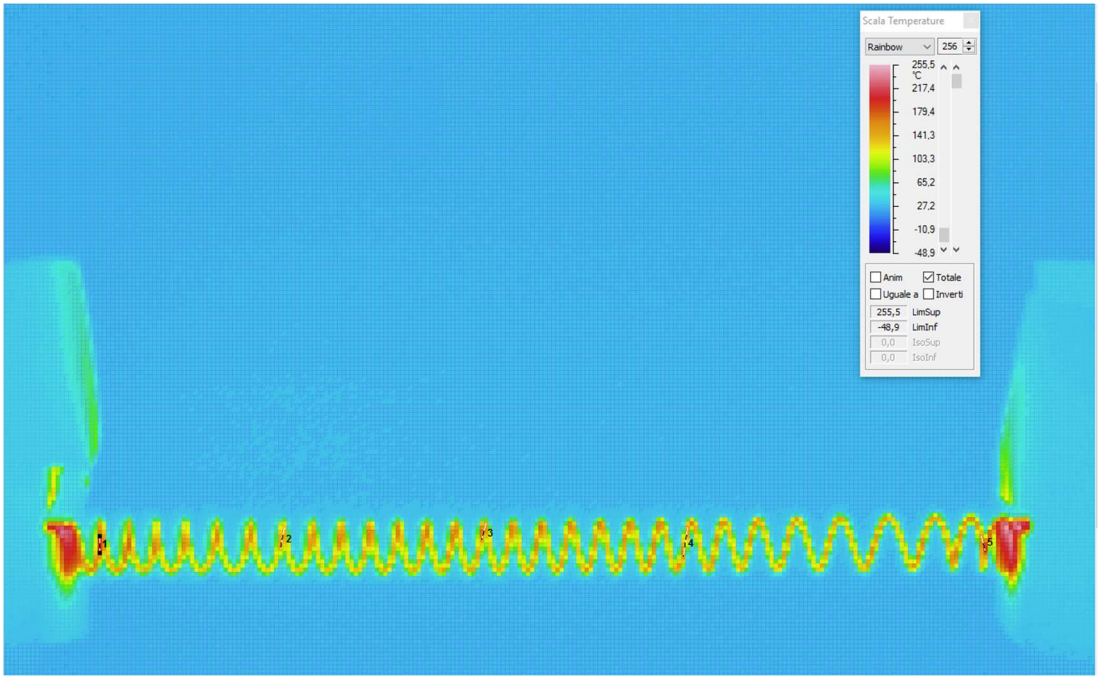

Fig. 73. Thermocamera image of test 2 when spring 4 is in complete austenitic state

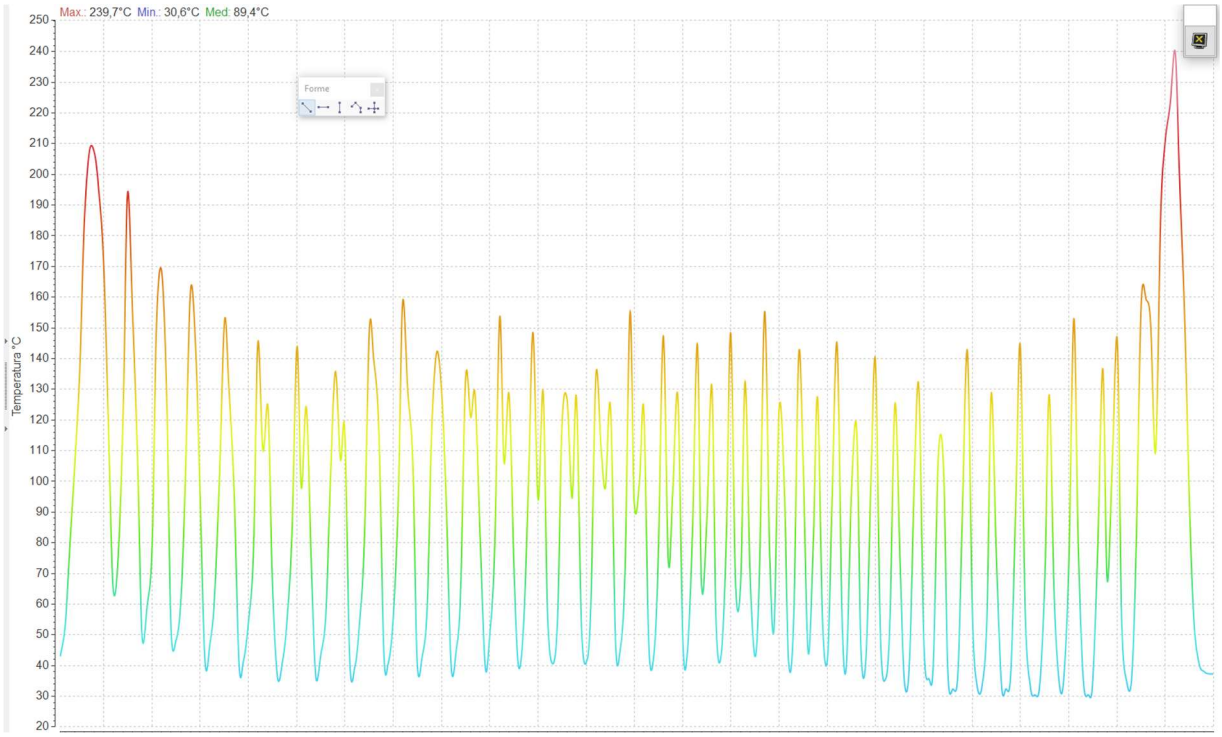

Fig. 74. Variation of the temperature of spring 4 along a longitudinal line for Fig. 73.

Regarding Fig. 73., five segments have been defined in the direction of the coils in different sections of the spring. The values of the maximum temperature along each line given by the thermocamera are shown in the following table.

Line	T_{max} (°C)	*Emissivity*
1	193,7	0,74
2	146,9	0,74
3	162,9	0,74
4	156,3	0,74
5	192,3	0,74

Table 12. Temperature values for Fig.73.

It can be noted that the maximum temperatures registered by the thermocamera are located in the ends of the spring, specially in the left end (line 1). Along the spring, the temperate is relatively uniform.

TEST 3:

Length (mm)	84,9
Current (A)	1,5
Voltage (V)	5,8

Maximum deformation, reached at t = 8 s: $10\ \mu\varepsilon$

Maximum force: $124{,}07\ g$

Cooling starts at t = 48 s

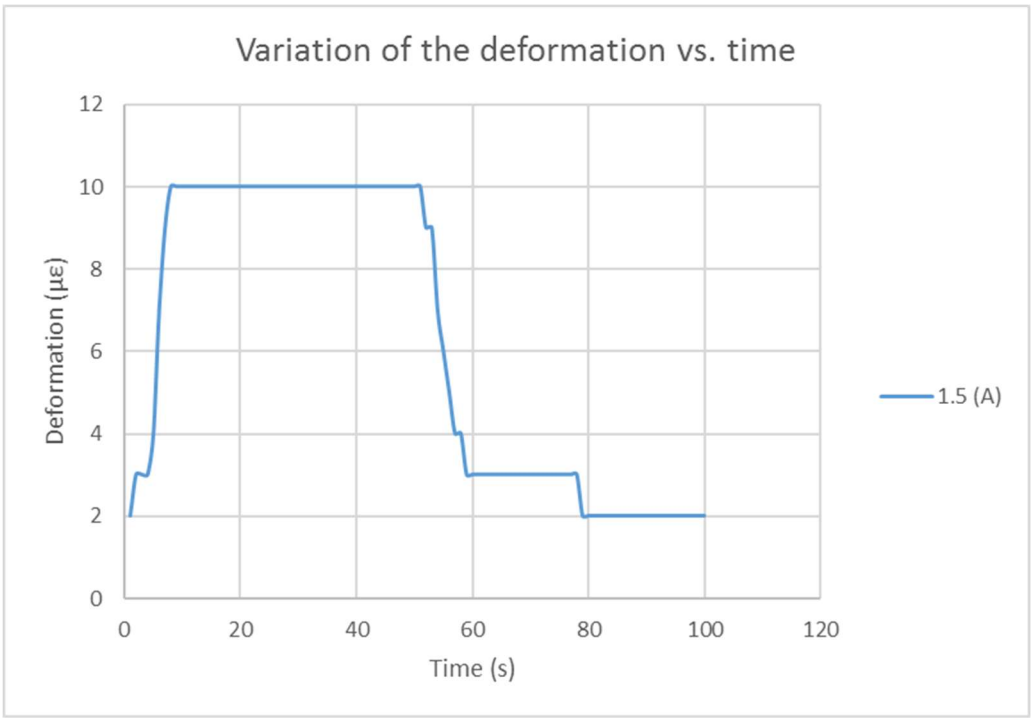

Fig. 75. Test 1: Variation of the deformation with time for a constant current and elongation of spring 4, 1,5 A and 84,9 mm, respectively.

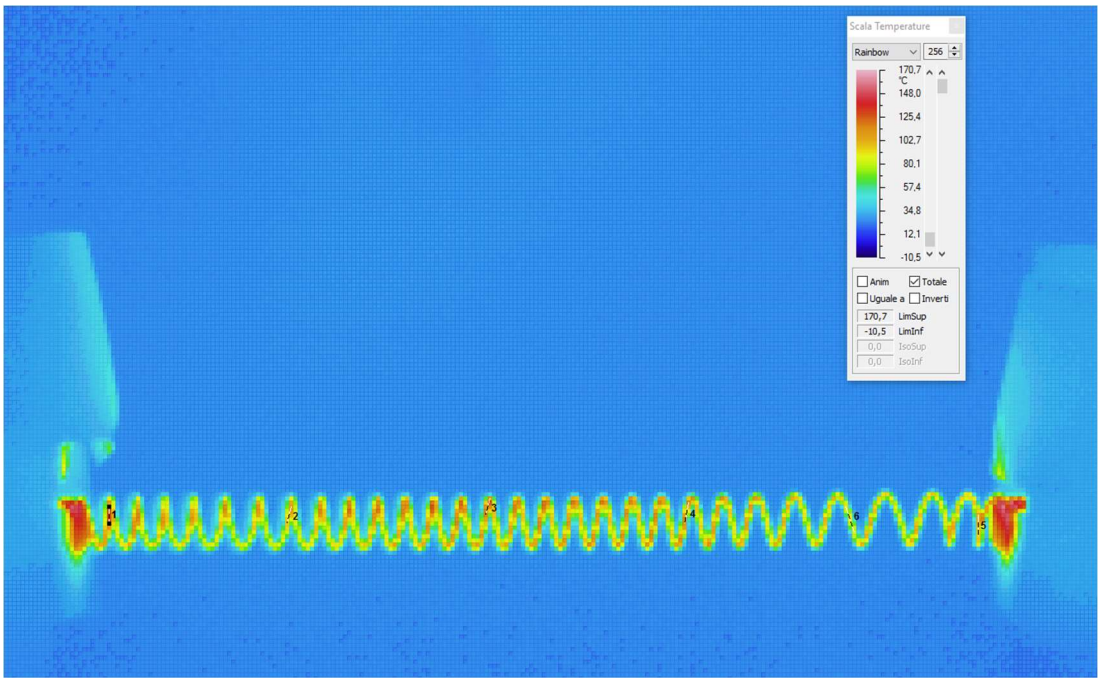

Fig. 76. Thermocamera image of test 3 when spring 4 is in complete austenitic state.

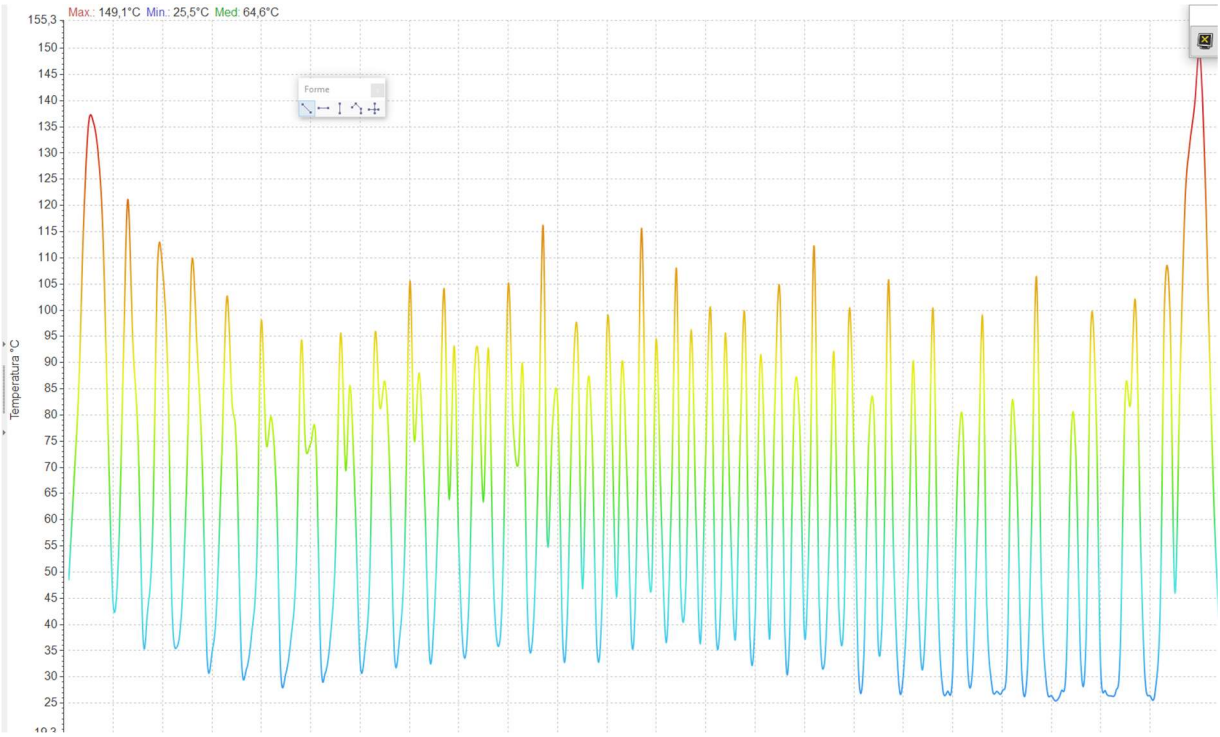

Fig. 76. Variation of the temperature of spring 4 along a longitudinal line for Fig 75.

Line	T_{max} (°C)	*Emissivity*
1	130,2	0,74
2	108,4	0,74
3	126,4	0,74
4	113,6	0,74
5	105,2	0,74
6	92,0	0,74

Table 13. Temperature values for Fig. 75.

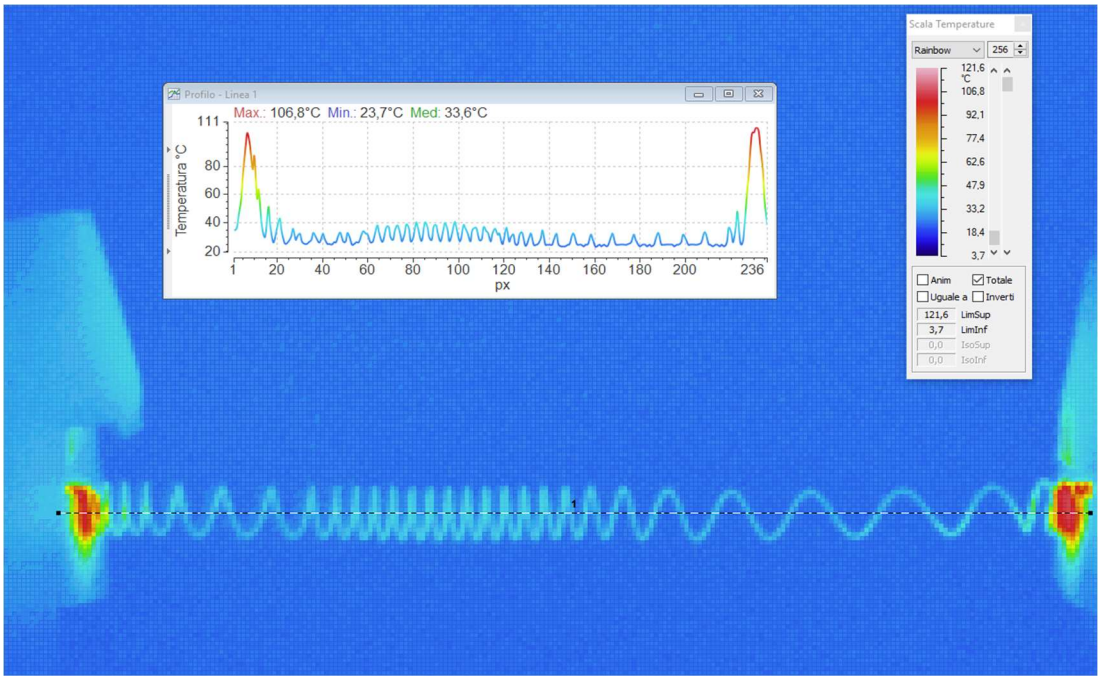

Fig. 77. Cooling of spring 4 in test 3

The maximum values of the temperature are again located in the left end of the spring and they are significantly higher compared to the temperature in the right end. This may be due to a wrong set up of the thermocamera.

TEST 4:

Length (mm)	84,9
Current (A)	1,25
Voltage (V)	4,8

Maximum deformation, reached at t = 20 s: $10\ \mu\varepsilon$

Maximum force: $124{,}07\ g$

Cooling starts at t = 68 s

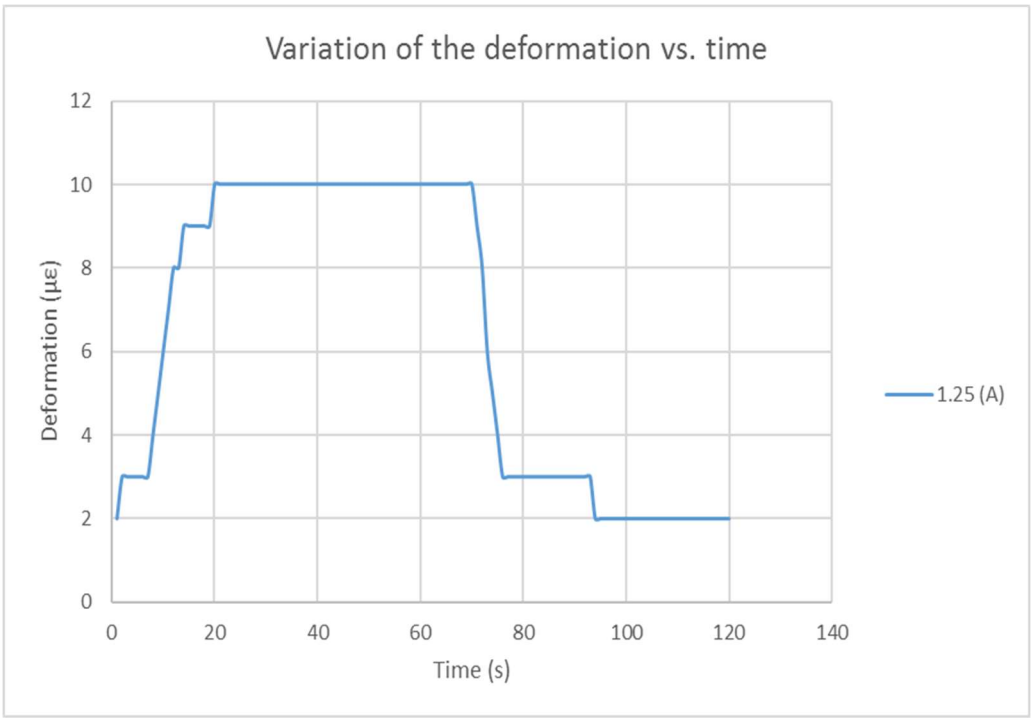

Fig. 78. Variation of the deformation with time for a constant current and elongation of spring 4, 1,25 A and 84,9 mm, respectively.

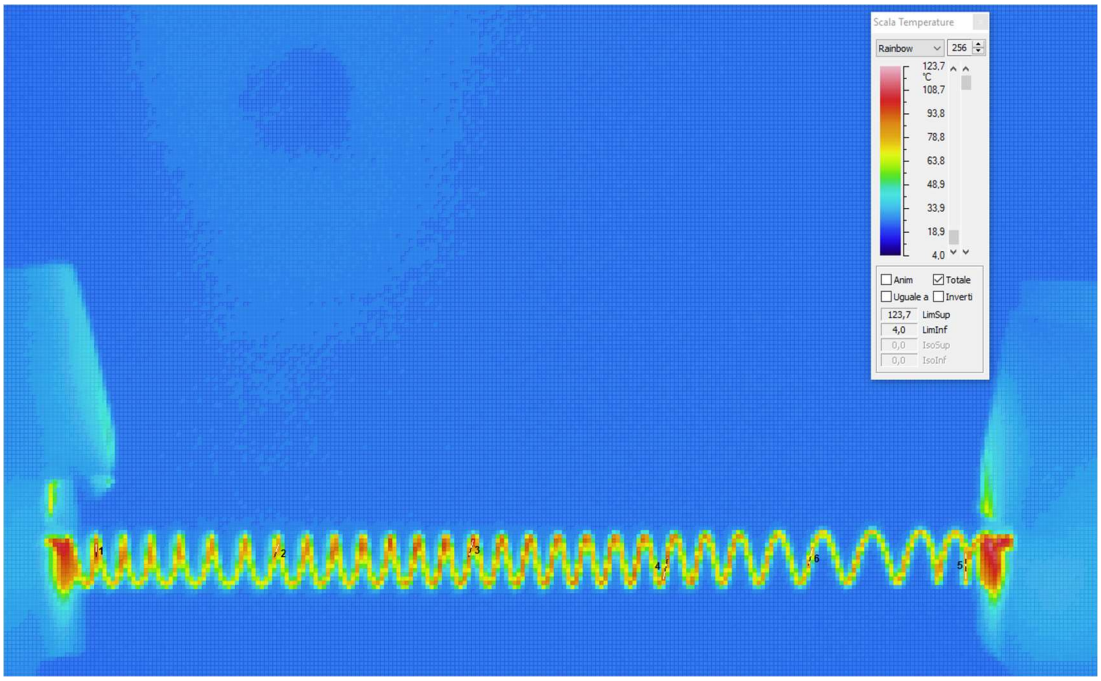

Fig. 79. Thermocamera image of test 4 when spring 4 is in complete austenitic state.

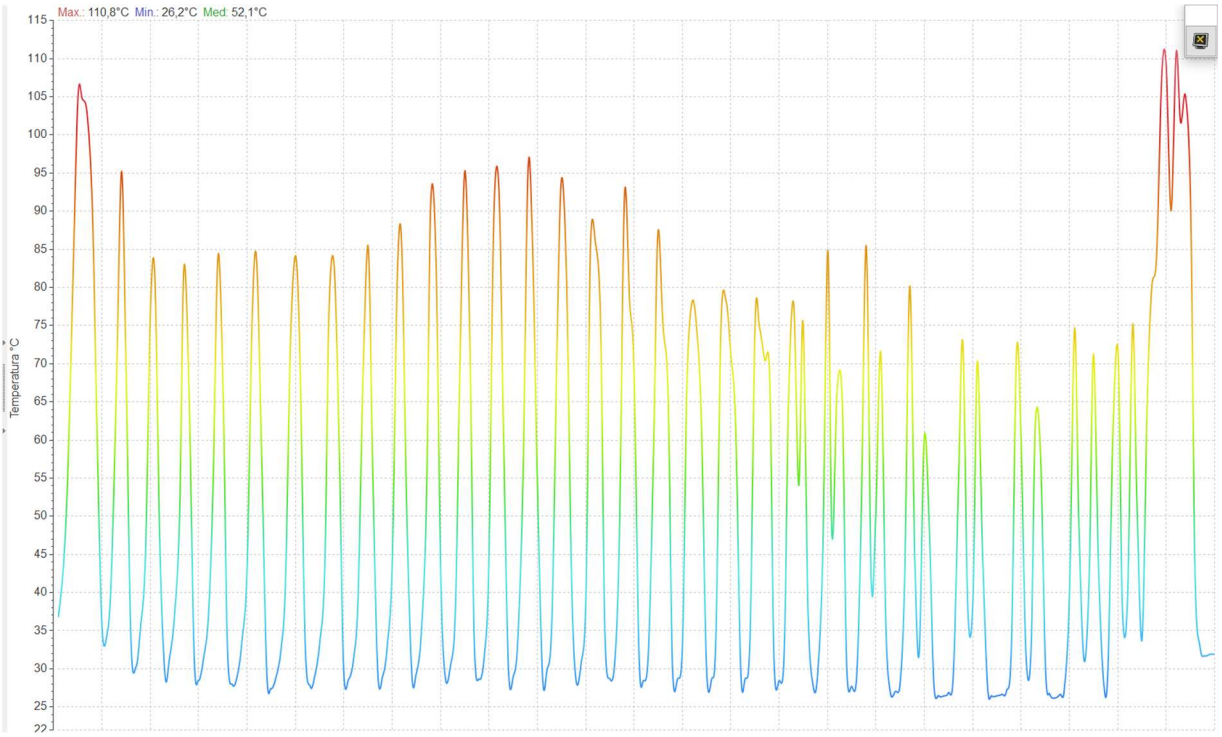

Fig. 80. Variation of the temperature of spring 4 along a longitudinal line for Fig. 79.

Line	T_{max} (°C)	*Emissivity*
1	96,1	0,74
2	82,7	0,74
3	99,9	0,74
4	90,9	0,74
5	81,2	0,74
6	80,7	0,74

Table 14. Temperature values for Fig. 79.

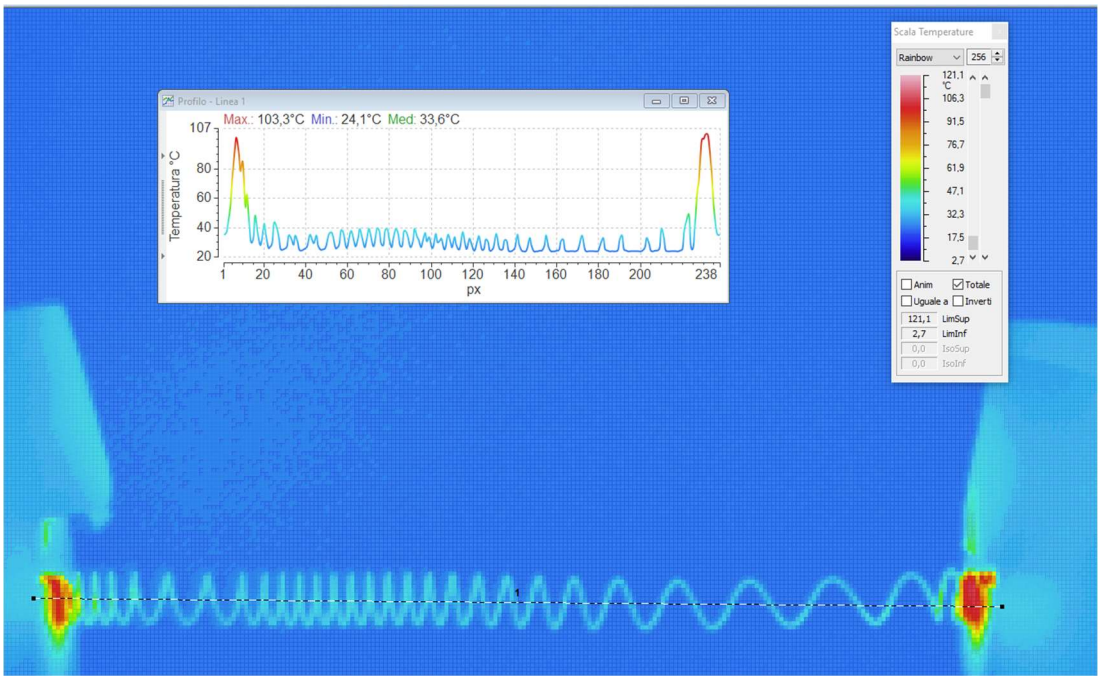

Fig. 81. Cooling of spring 4 in test 4.

From Fig. 81., it can be observed that there is a displacement of the coils to the left part of the spring, while in the right side, the strain is higher. This can be due to a lack of homogeinity in the material because of the shaping process of the spring. Regarding this shaping process, spring 4 was air cooled, which may have affected the level of uniformity of the component.

As expected, comparing the results of the last tests, higher temperatures are reached in the spring when the applied current is higher.

TEST 5:

In these further tests, the thermocamera was not used. Therefore, there are no data about the temperature along the spring.

Length (mm)	113,2
Current (A)	1
Voltage (V)	3,8

Maximum deformation, reached at t = 49 s: $9\ \mu\varepsilon$

Maximum force: $111{,}66\ g$

Cooling starts at t = 107 s

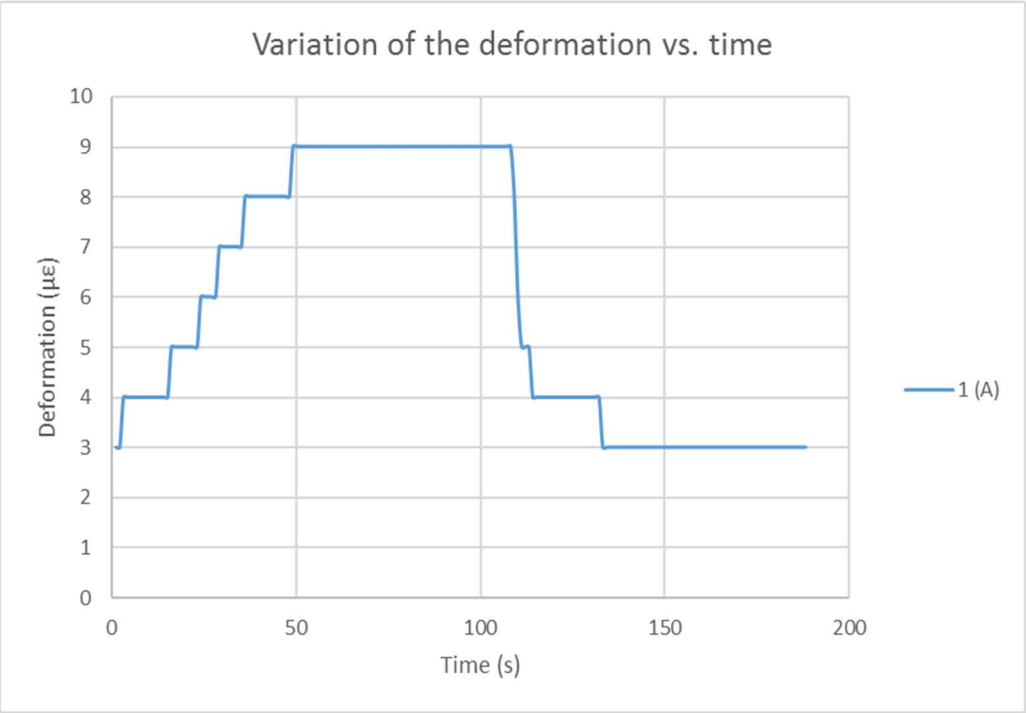

Fig. 82. Variation of the deformation with time for a constant current and elongation of spring 4, 1 A and 113,2 mm, respectively.

TEST 6:

Length (mm)	113,2
Current (A)	1,25
Voltage (V)	4,9

Maximum deformation, reached at t = 18 s: $15\ \mu\varepsilon$

Maximum force: $186{,}10\ g$

Cooling starts at t = 74 s

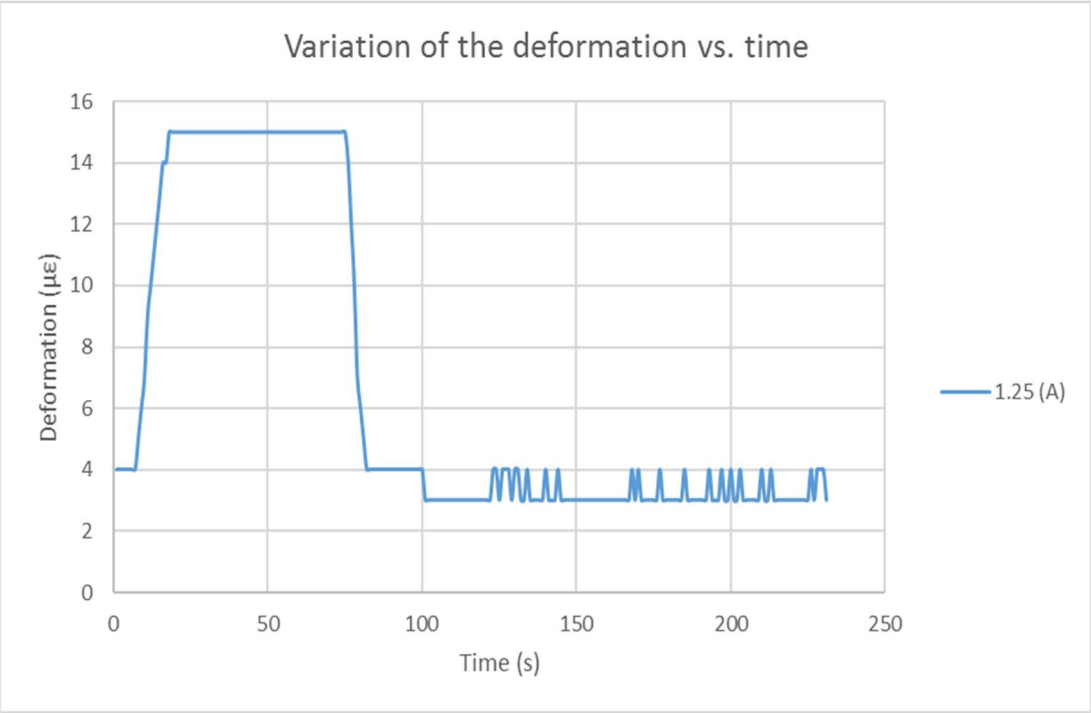

Fig. 83. Variation of the deformation with time for a constant current and elongation of spring 4, 1,25 A and 113,2 mm, respectively.

TEST 7:

Length (mm)	113,2
Current (A)	1,5
Voltage (V)	4,8

Maximum deformation, reached at t = 7 s: $15\ \mu\varepsilon$

Maximum force: $186{,}10\ g$

Cooling starts at t = 51 s

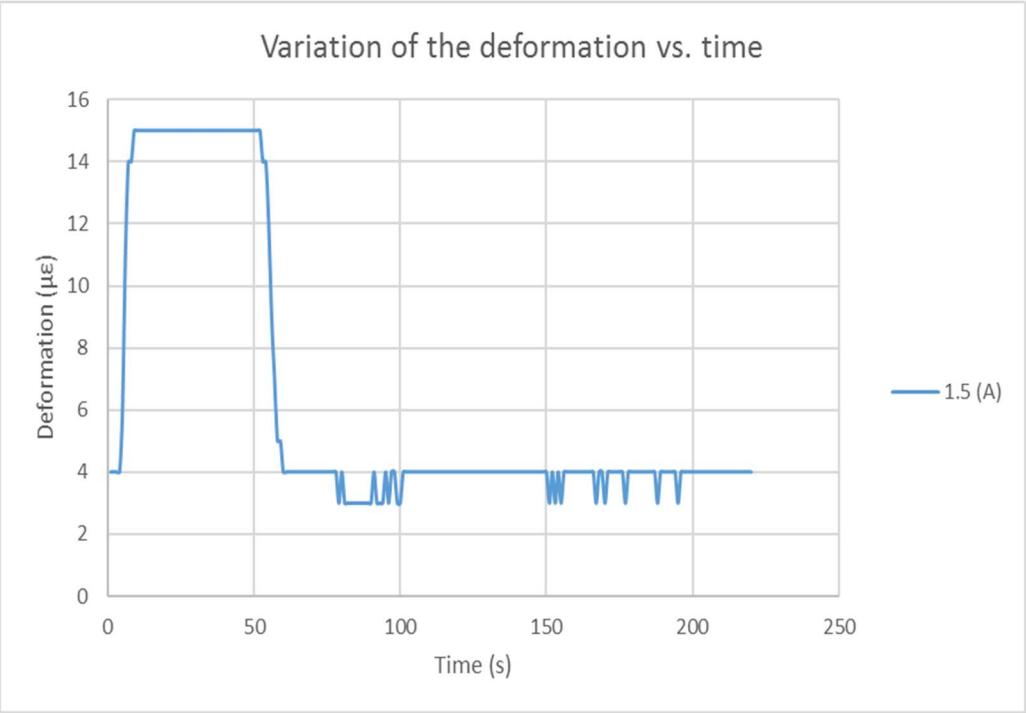

Fig. 84. Variation of the deformation with time for a constant current and elongation of spring 4, 1,5 A and 113,2 mm, respectively.

TEST 8:

Length (mm)	113,2
Current (A)	2
Voltage (V)	8

Maximum deformation, reached at t = 6 s: $15\ \mu\varepsilon$

Maximum force: $186{,}10\ g$

Cooling starts at t = 27 s

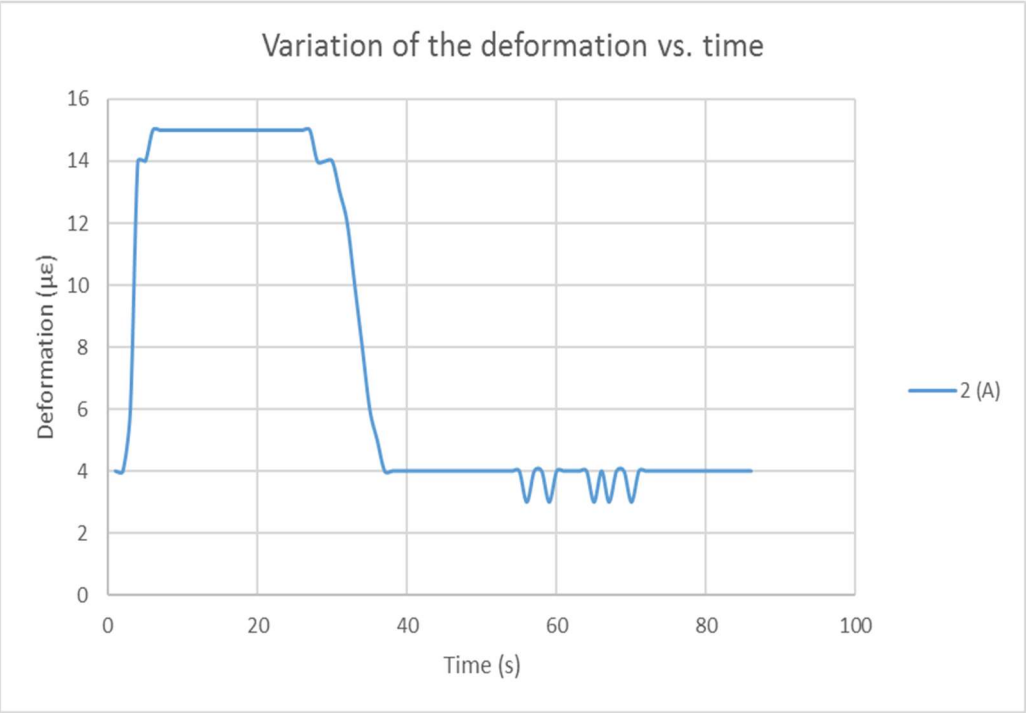

Fig. 85. Variation of the deformation with time for a constant current and elongation of spring 4, 2 A and 113,2 mm, respectively.

TEST 9:

Length (mm)	157,0
Current (A)	1
Voltage (V)	3,8

Maximum deformation, reached at t = 78 s: $11\ \mu\varepsilon$

Maximum force: $136{,}48\ g$

Cooling starts at t = 127 s

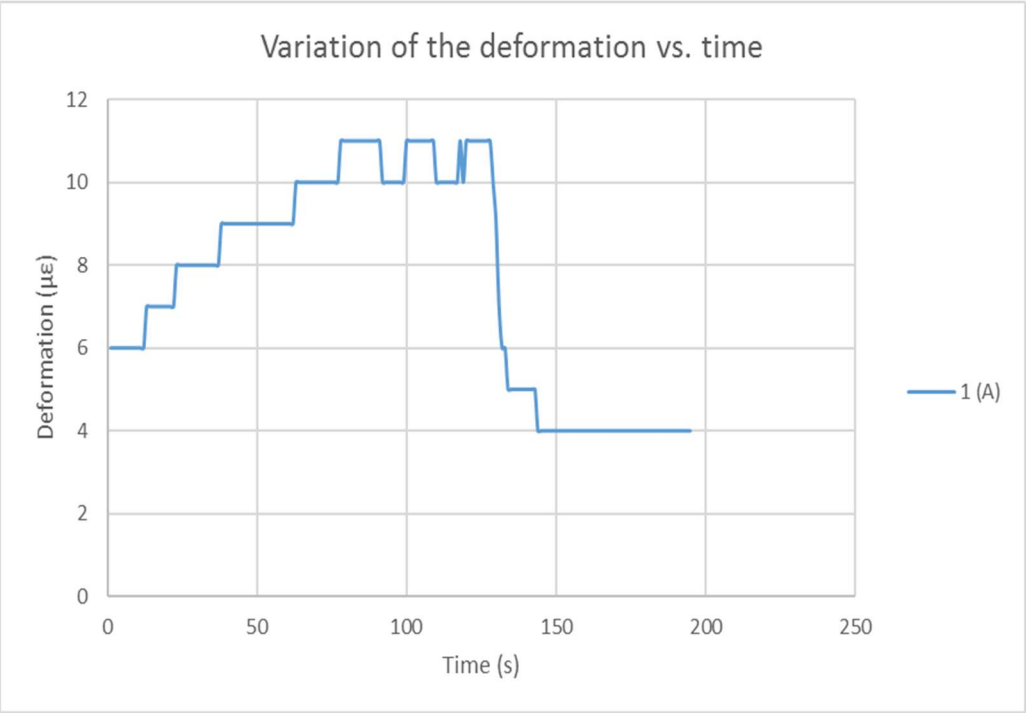

Fig. 86. Variation of the deformation with time for a constant current and elongation of spring 4, 1 A and 157,0 mm, respectively.

TEST 10:

Length (mm)	157,0
Current (A)	1,25
Voltage (V)	4,8

Maximum deformation, reached at t = 24 s: $19\ \mu\varepsilon$

Maximum force: $235{,}73\ g$

Cooling starts at t = 54 s

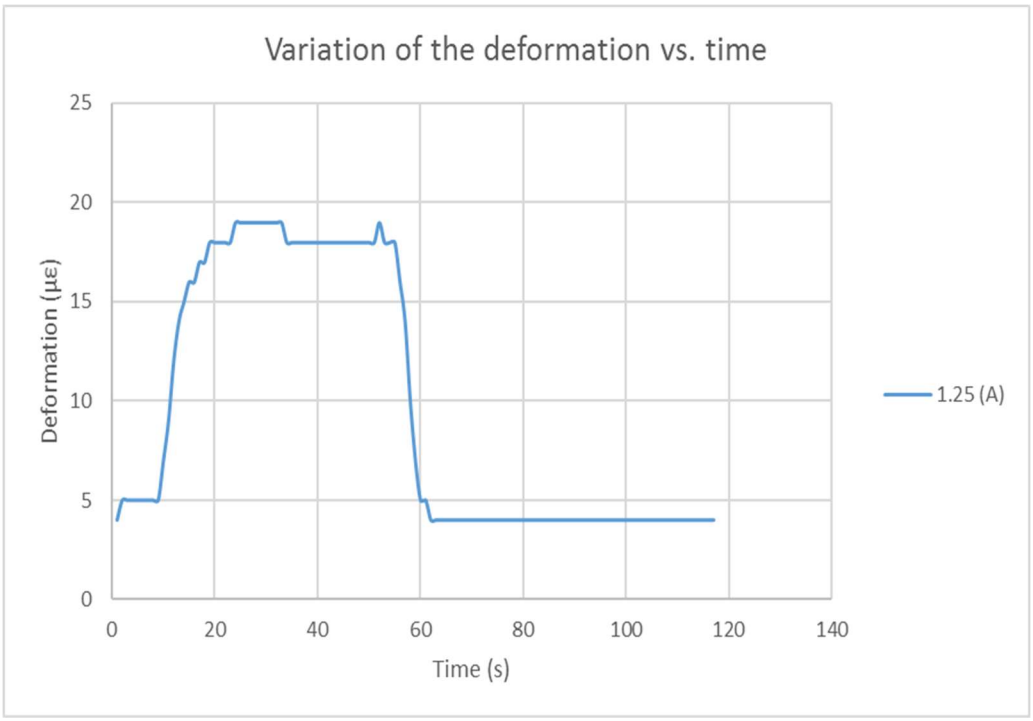

Fig. 87. Variation of the deformation with time for a constant current and elongation of spring 4, 1,25 A and 157,0 mm, respectively.

2.2.5 Conclusions of test 1 for spring 4

A collection of the results of test 1 for spring 4 are shown in the following graphs. These graphs have been made filtering the data and not considering the plateaus, so that there are no rough steps and the plots are more representative.

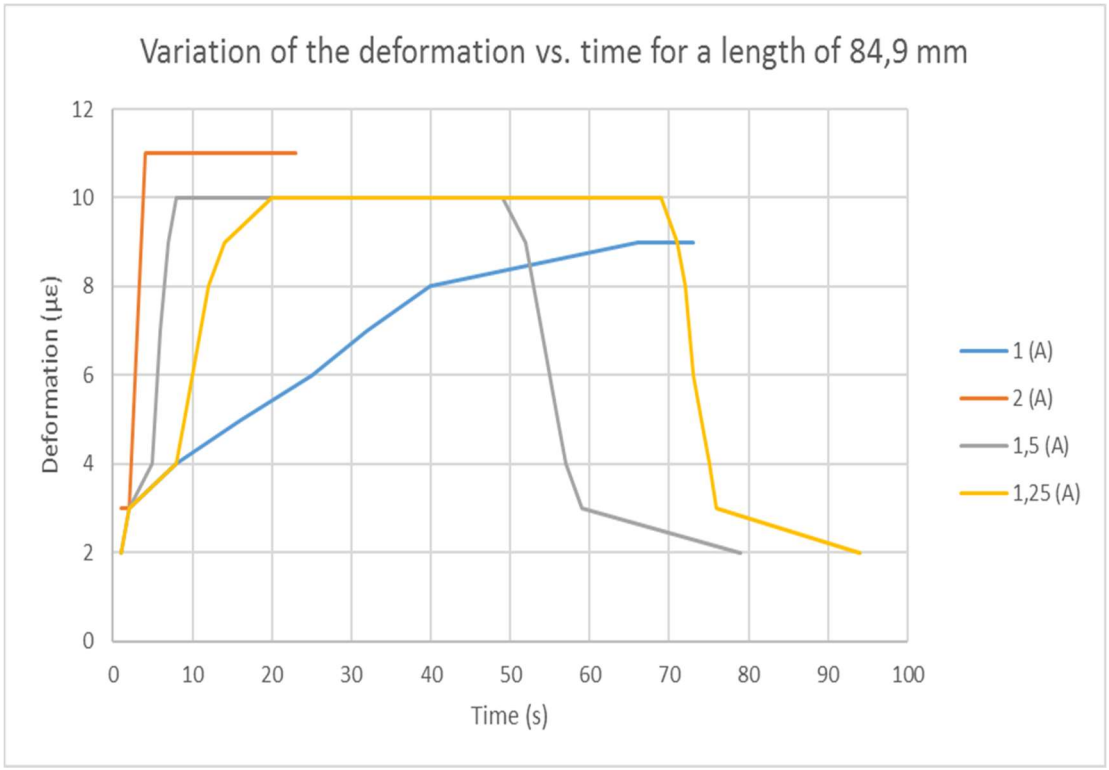

Fig. 88. Variation of the deformation in the load cell with the time for a length of spring 4 of 84,9 mm for different currents

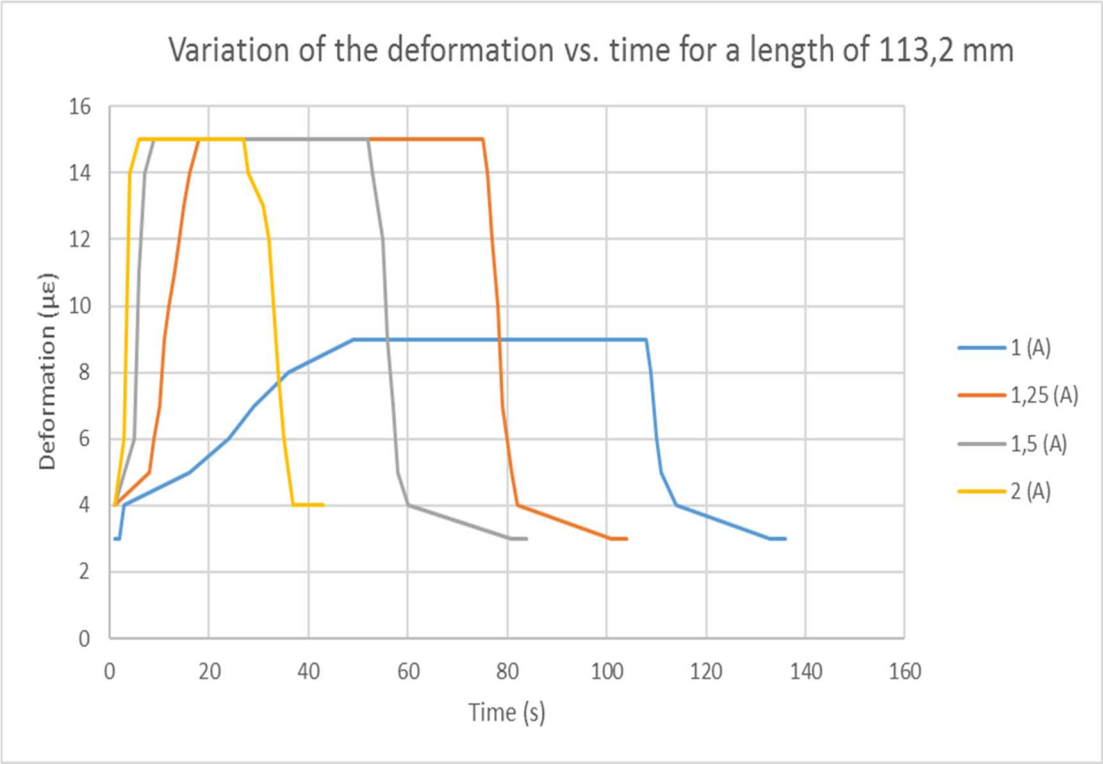

Fig. 89. Variation of the deformation in the load cell with the time for a length of spring 4 of 113,2 mm for different currents

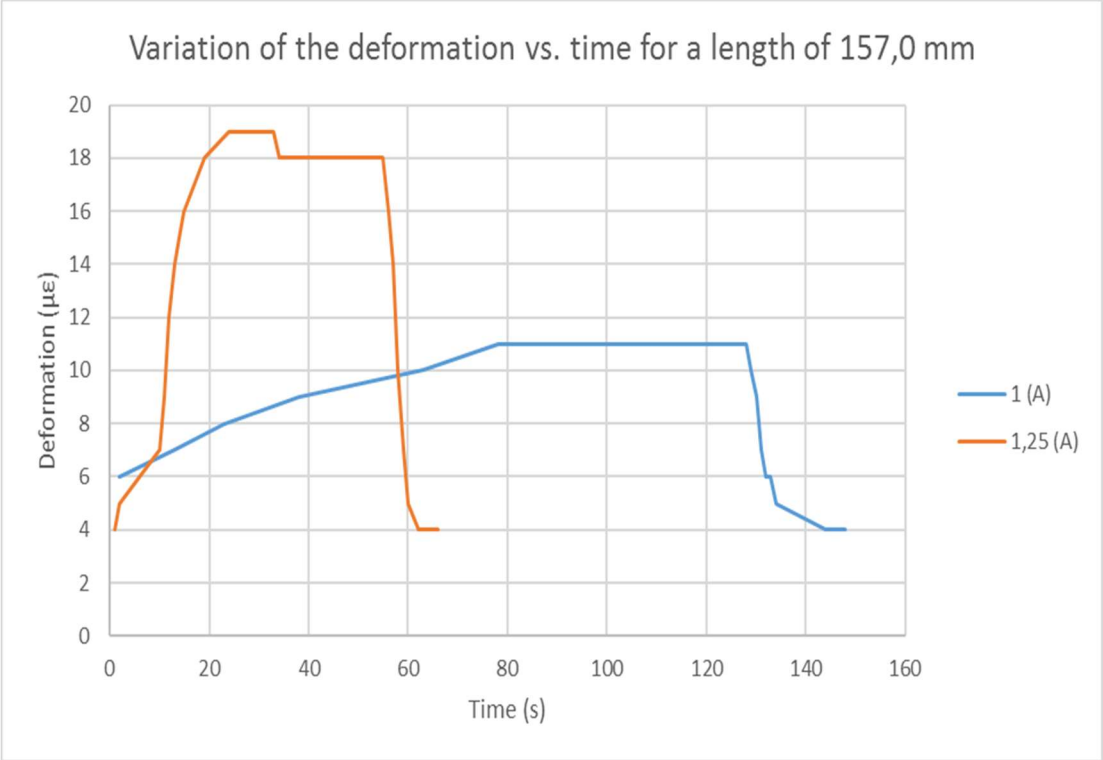

Fig. 90. Variation of the deformation in the load cell with the time for a length of spring 4 of 157,0 mm for different currents

From the figures above, the first fact that can be noted is that the time to reach the maximum deformation (and consequentely, the maximum force) decreases when the current applied is higher, existing an important difference when the current applied is 1 A, for which the time to get to the maximum deformation is significantly higher comparing to the tests where the other three levels of current are applied. It is not notable dependency of the time to reach the maximum deformation on the level of strain at which the spring is subjected.

It can be also noticeable that the maximum deformation is moreless constant for the different currents applied, except for 1 A, for which the maximum deformation is significantly lower. These two variations, in maximum deformation and time to obtain it, of the current of 1 A with respect to the other levels of current may be due to the fact that 1 A is not enough to perform the complete transformation from detwinned martensite to austenite and then pure austenitic state is not achieved. Therefore, we may be working in a transition state with a "mixture" of martensite and austenite and the maximum force is not reached. So, if considering the activation current as 1,25 A, the transformation temperature A_f for the level of stress corresponding to a spring elongation of 84,9 mm is around 80˚C (which is the mínimum temperature registered in the spring during the austenitic state with the thermocamera).

Another fact to point out is that the maximum force obtained is higher for higher elongations of the spring. The larger strain it is applied to the spring, the larger the force it is able to exert, since the deformation it tries to recover is higher.

Concerning the shape of the individual graphs, the lines are not smooth and some steps can be noticed. The reason is the lack of accuracy of the load cell for our small range of deformation (0-19 με). Therefore, the graphs showing multiple tests have been made cutting the plateaus.

2.2.6 Results of test 1 for spring 5

Before starting the test with spring 5, we need to calculate the initial length of spring 5 for our set up, as we previously did for spring 4. Moreover, spring 5 will be stretched three different lengths: first, the value corresponding to the length when the load was released in test 0 (L2); second, the length when the load was applied (L1); and third, 4/3 of this last length. The references are taken from the fifth cycle in test 0. To calculate the equivalent elongations for our set up, we proceed as we did with spring 4.

	Nº of spires	*Initial length L0 (mm)*	*L0/nºspires (mm/spire)*	*L1 (mm)*	*L1/nºspires (mm/spire)*	*L2 (mm)*	*L2/nºspires (mm/spire)*
Test 0	21	17,5	0,833	68,9	3,281	41,9	1,995
Current set-up	17	14,2	0,833	55,8	3,281	33,9	1,995

Table 15. Calculation of the different lengths spring 5 will be stretched in the current set-up

Thus, as explained before, spring 5 will be subjected to three different lengths: 33,9 mm (L2); 55,8 mm (L1); and 74,4 mm (4/3 of 55,8 mm). In each of the three elongations, several levels of current will be applied.

<u>TEST 1:</u>

Because of a human error, the emissivity of these tests is 0,96; the value set by default.

Length (mm)	33,9
Current (A)	1
Voltage (V)	2,8

Maximum deformation, reached at t = 62 s: $16\ \mu\varepsilon$

Maximum force: $198{,}51\ g$

Cooling starts at t = 147 s

As a remark for this test, when the highest value of the deformation was achieved, the current decreased slightly, oscillating around 0,97 A.

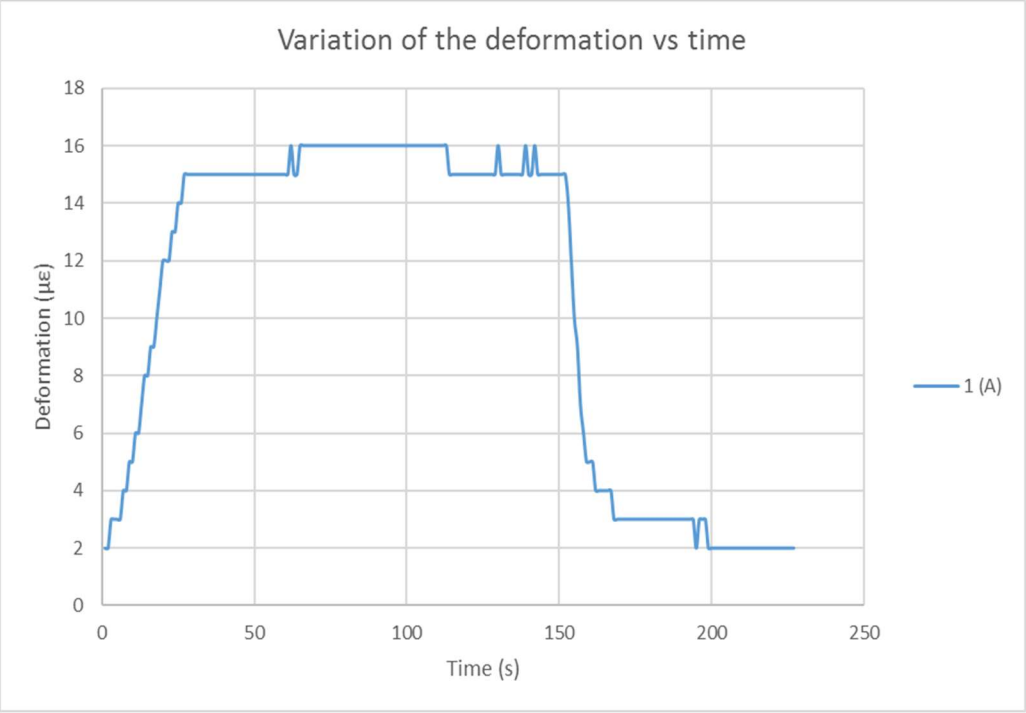

Fig. 91. Variation of the deformation with time for a constant current and elongation of spring 4, 1 A and 33,9 mm, respectively.

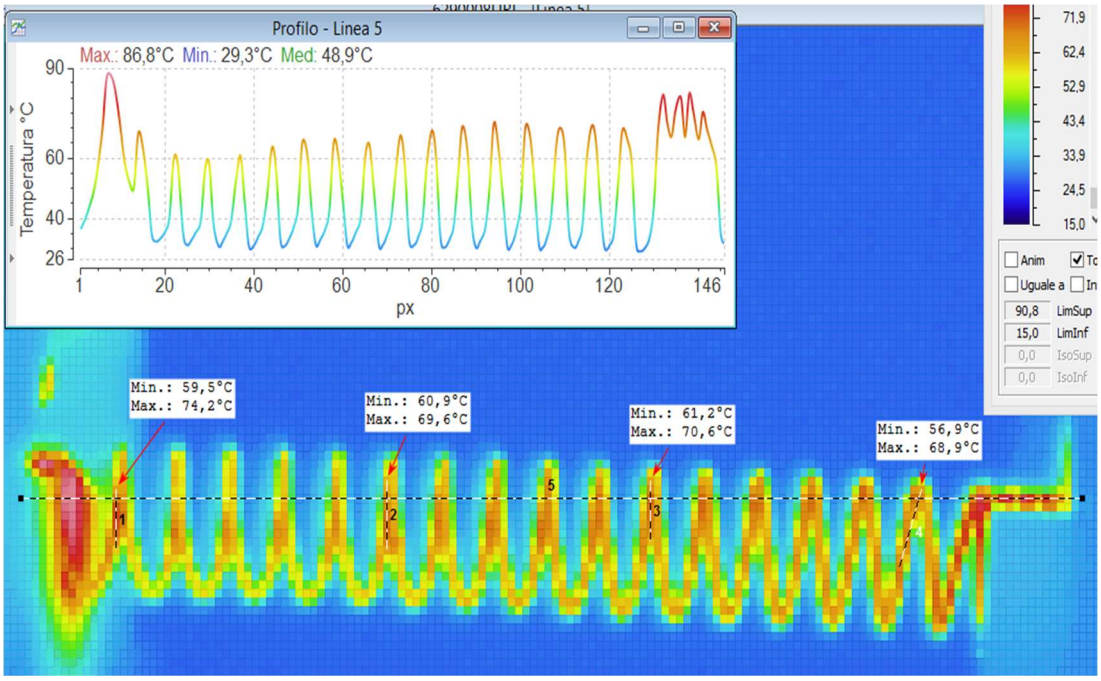

Fig. 92. Thermocamera image of test 1 when spring 5 is in complete austenitic state and at its maximum temperature.

Line	T_{max} (°C)	*Emissivity*
1	74,2	0,96
2	69,6	0,96
3	70,6	0,96
4	68,9	0,96
5	86,6	0,96

Table 16. Temperature values for Fig. 91.

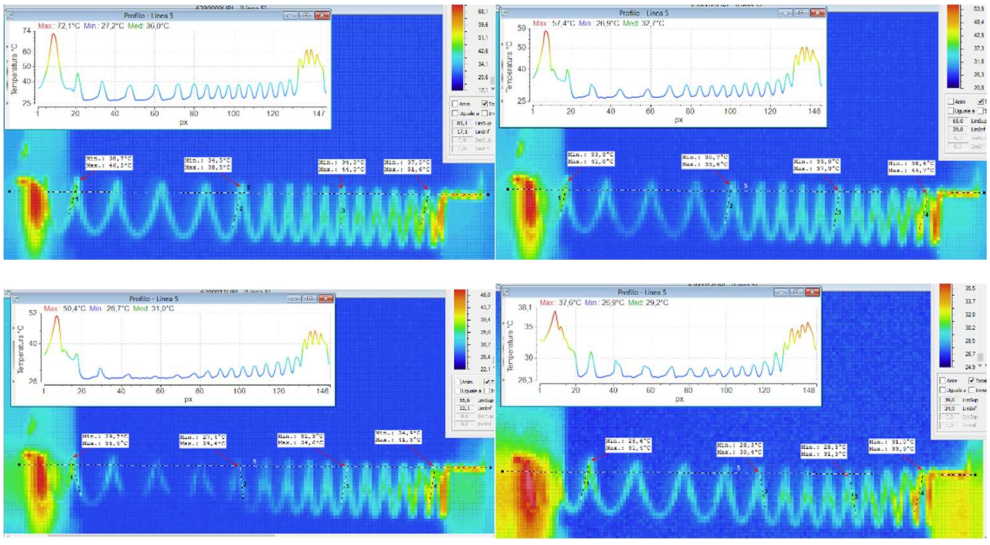

Fig. 93. Cooling process of spring 5 in test 1

From the previous table, we can observed that now the maximum temperature is detected in the ends of the spring.

TEST 2:

Length (mm)	33,9
Current (A)	1,25
Voltage (V)	3,5

Maximum deformation, reached at t = 96 s: $15\ \mu\varepsilon$

Maximum force: $186{,}10\ g$

Cooling starts at t = 122 s

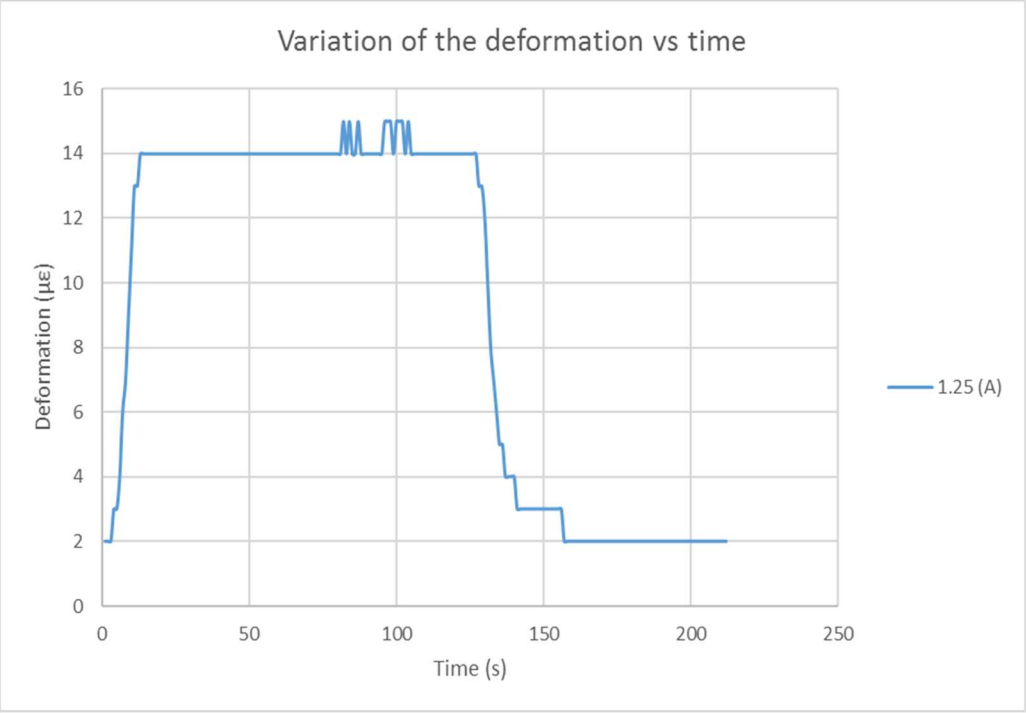

Fig. 94. Variation of the deformation with time for a constant current and elongation of spring 5, 1,25 A and 33,9 mm, respectively.

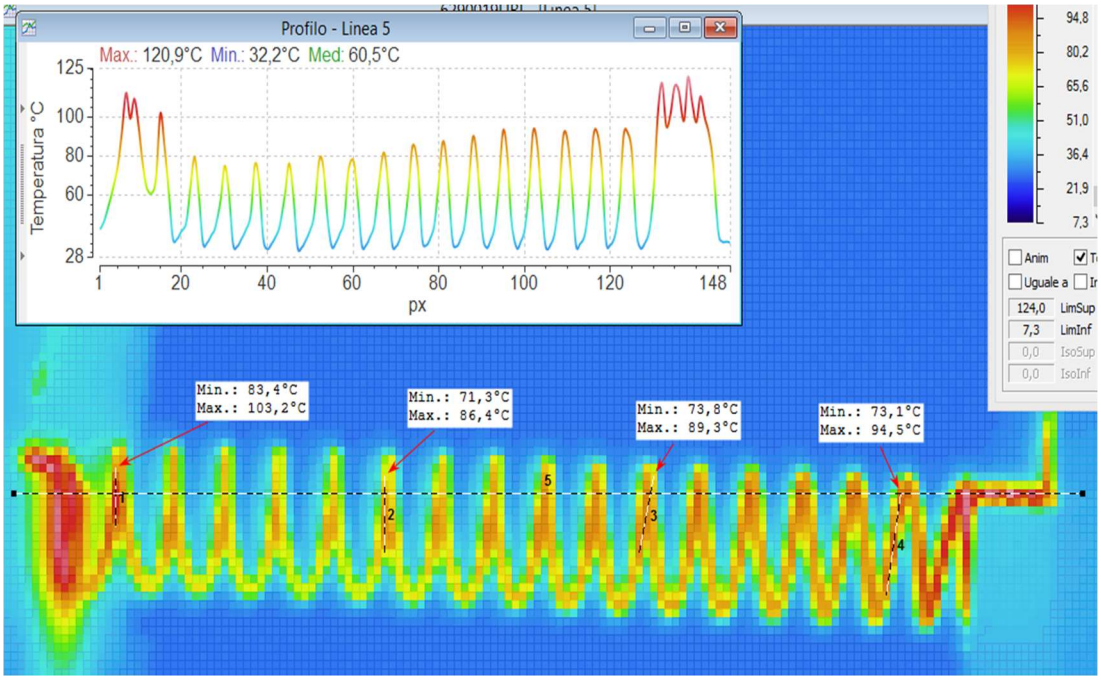

Fig. 95. Thermocamera image of test 2 when spring 5 is in complete austenitic state and at its maximum temperature

Line	T_{max} (°C)	*Emissivity*
1	103,2	0,96
2	86,4	0,96
3	89,3	0,96
4	94,5	0,96
5	120,9	0,96

Table 17. Temperature values for Fig. 95.

In this case and as usual, the maximum temperatures are registered in the ends of the spring.

TEST 3:

Length (mm)	33,9
Current (A)	1,5
Voltage (V)	4,3

Maximum deformation, reached at t = 7 s: $15\ \mu\varepsilon$

Maximum force: $186{,}10\ g$

Cooling starts at t = 35 s

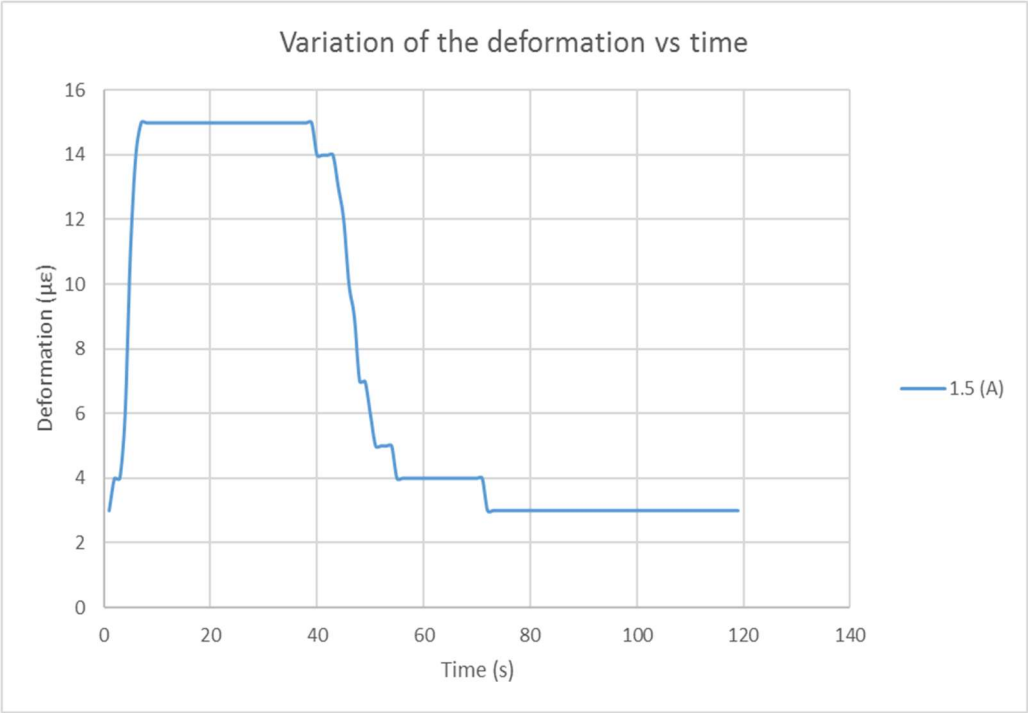

Fig. 96. Variation of the deformation with time for a constant current and elongation of spring 5, 1,5 A and 33,9 mm, respectively.

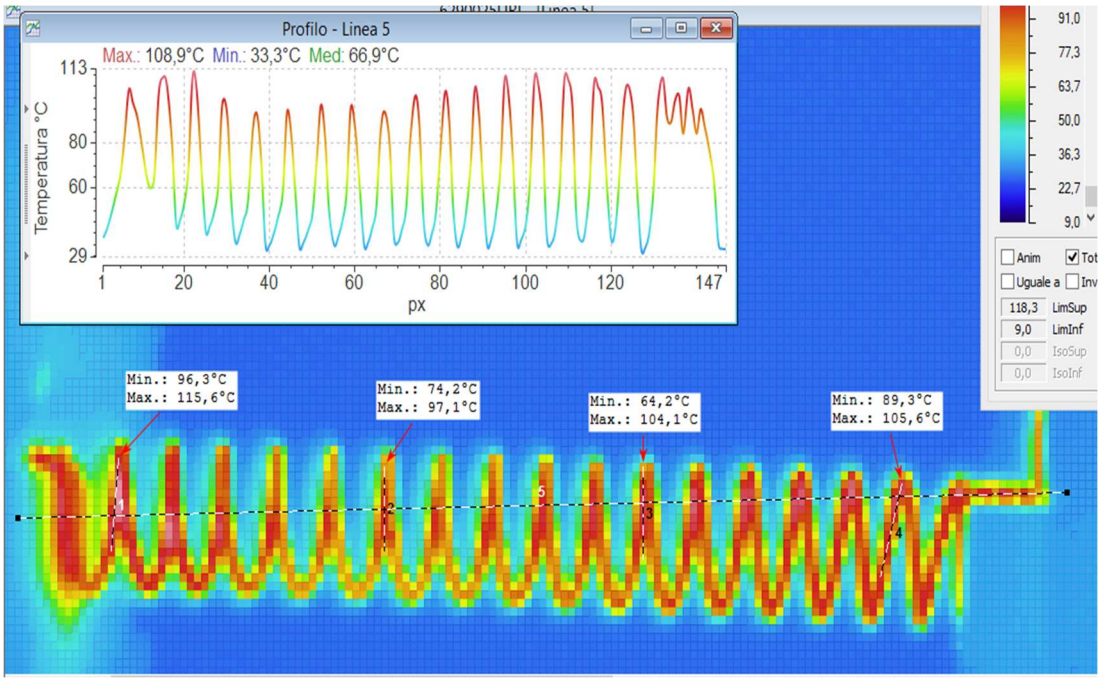

Fig. 97. Thermocamera image of test 3 when spring 5 is in complete austenitic state and at its maximum temperature

Line	T_{max} $(°C)$	*Emissivity*
1	115,6	0,96
2	97,1	0,96
3	104,1	0,96
4	105,6	0,96
5	108,9	0,96

Table 18. Temperature values for Fig. 97.

TEST 4:

Length (mm)	33,9
Current (A)	2
Voltage (V)	5,7

Maximum deformation, reached at t = 6 s: $19\ \mu\varepsilon$

Maximum force: $235{,}73\ g$

Cooling starts at t = 45 s

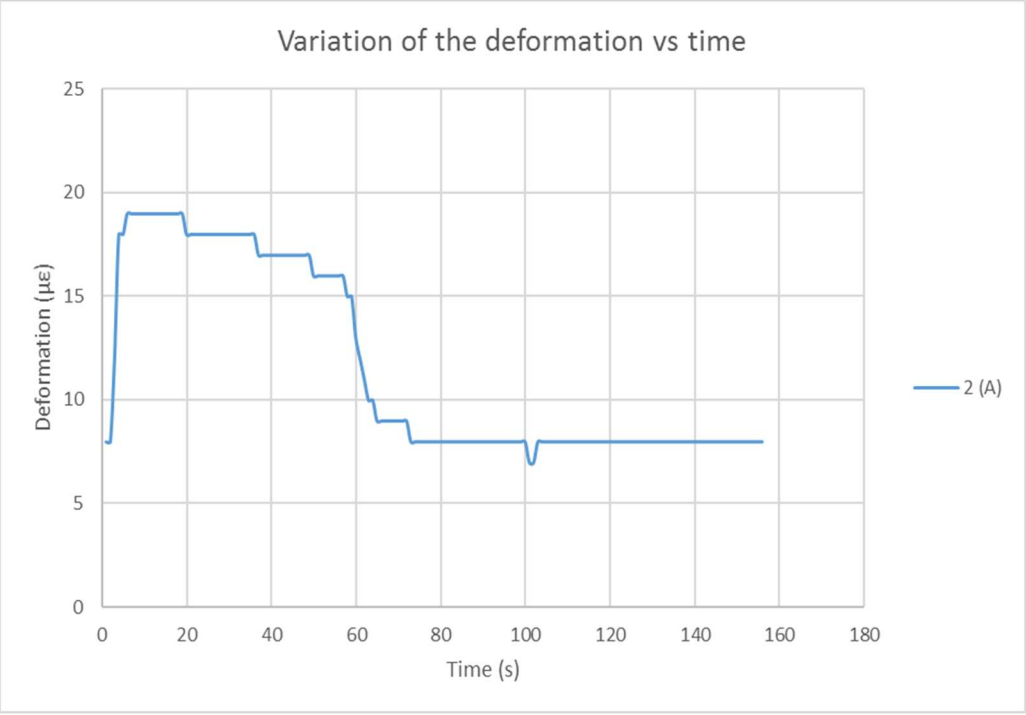

Fig. 98. Variation of the deformation with time for a constant current and elongation of spring 5, 2 A and 33,9 mm, respectively.

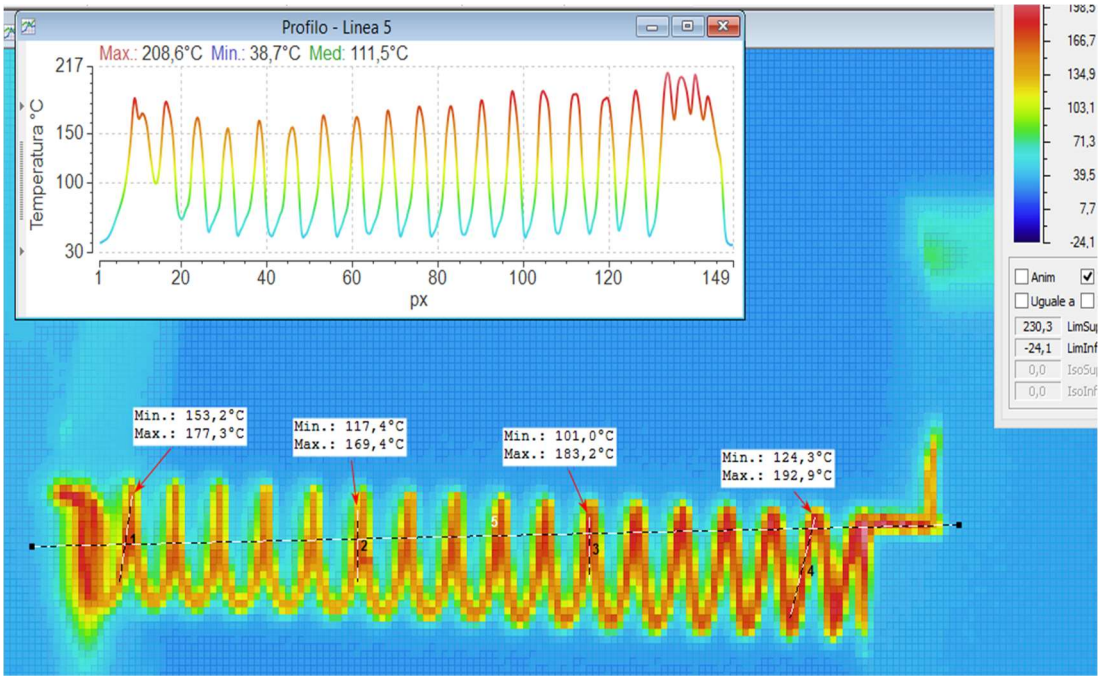

Fig. 99. Thermocamera image of test 4 when spring 5 is in complete austenitic state and at its maximum temperature

Line	T_{max} (°C)	*Emissivity*
1	177,3	0,96
2	169,4	0,96
3	183,2	0,96
4	192,9	0,96
5	208,6	0,96

Table. Temperature values for Fig. 99.

In this test, it can be noticed that the higher temperatures are displaced to the right side of the spring.

<u>TEST 5:</u>

Length (mm)	33,9
Current (A)	2,5
Voltage (V)	7,3

Maximum deformation, reached at t = 3 s: $15\ \mu\varepsilon$

Maximum force: $186{,}10\ g$

Cooling starts at t = 46 s

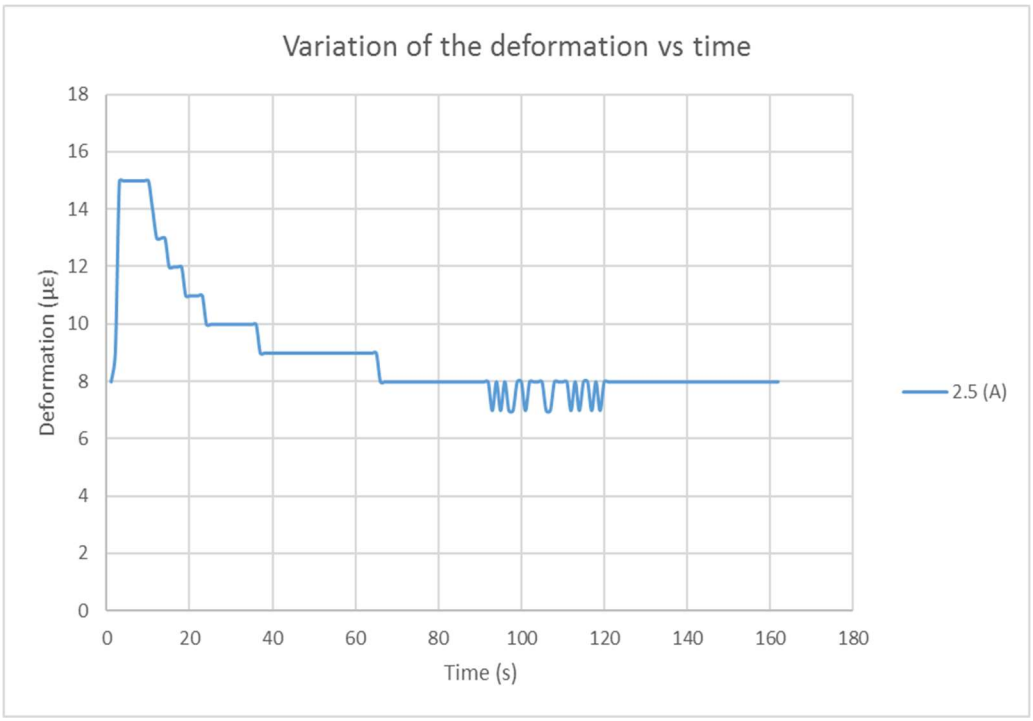

Fig. 100. Variation of the deformation with time for a constant current and elongation of spring 5, 2,5 A and 33,9 mm, respectively.

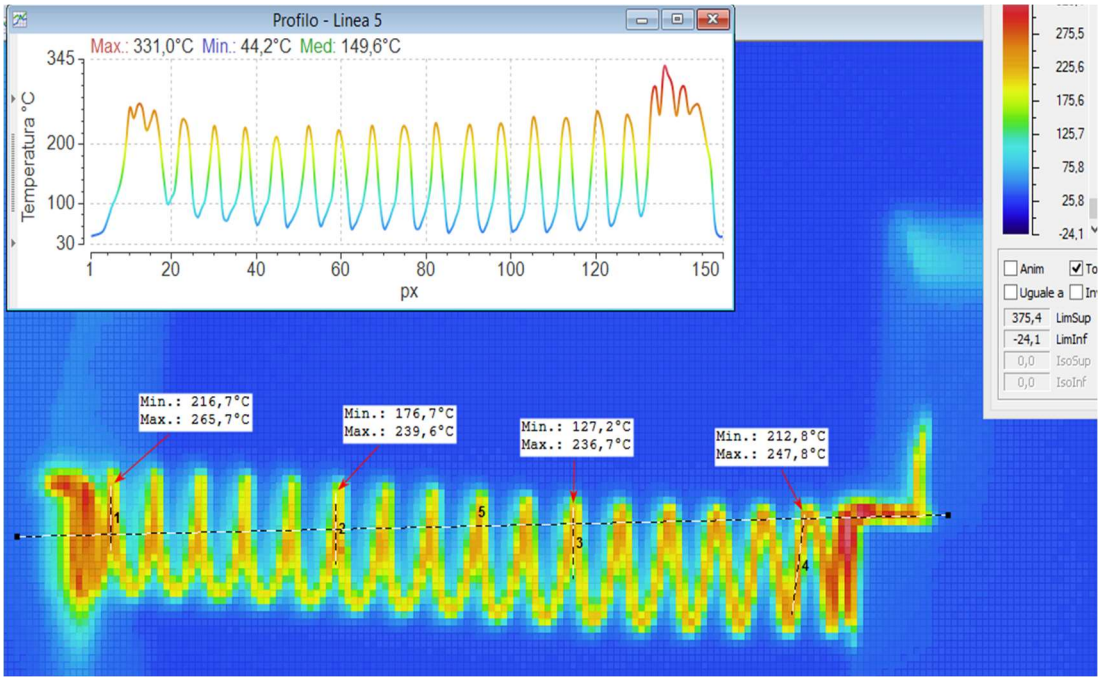

Fig. 101. Thermocamera image of test 5 when spring 5 is in complete austenitic state and at its maximum temperature

Line	T_{max} $(°C)$	*Emissivity*
1	265,7	0,96
2	239,6	0,96
3	236,7	0,96
4	247,8	0,96
5	231,0	0,96

Table 20. Temperature values for Fig. 101.

Very high temperatures are reached in this test. This fact causes the relaxation of the teflon since temperatures very closed to its melting point are obtained. Therefore, we can observe a drop in the deformation of the load cell right after getting to the maximum value. This effect can be also noticed slightly in test 4. Moreover, this maximum values is significantly lower than the maximum values obtained in the previous tests, also due to the relaxation of the clamping system, which may have been damages for further tests.

TEST 6:

Length (mm)	55,8
Current (A)	1
Voltage (V)	2,8

Maximum deformation, reached at t = 35 s: $23\ \mu\varepsilon$

Maximum force: $285{,}36\ g$

Cooling starts at t = 119 s

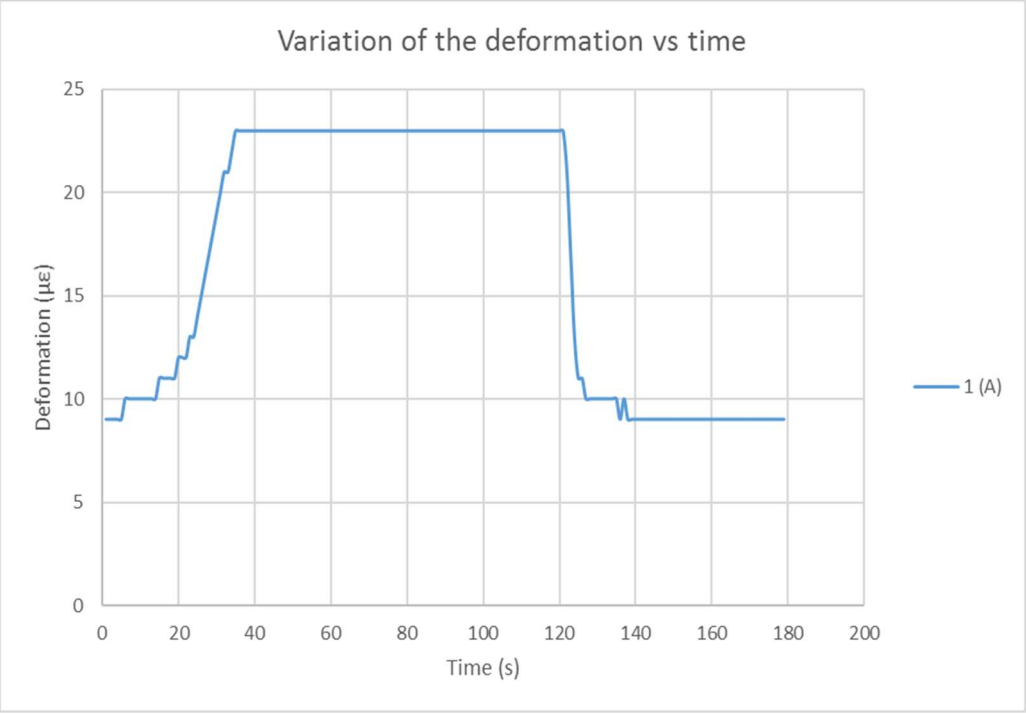

Fig. 102. Variation of the deformation with time for a constant current and elongation of spring 5, 1 A and 55,8 mm, respectively.

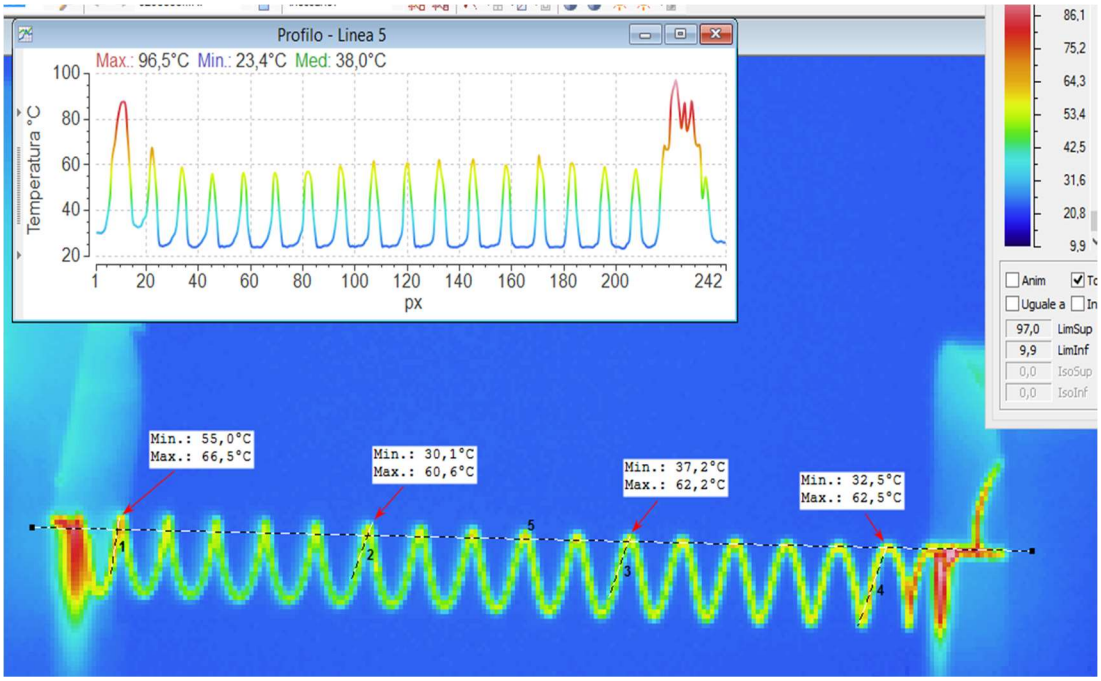

Fig. 103. Thermocamera image of test 6 when spring 5 is in complete austenitic state and at its maximum temperature

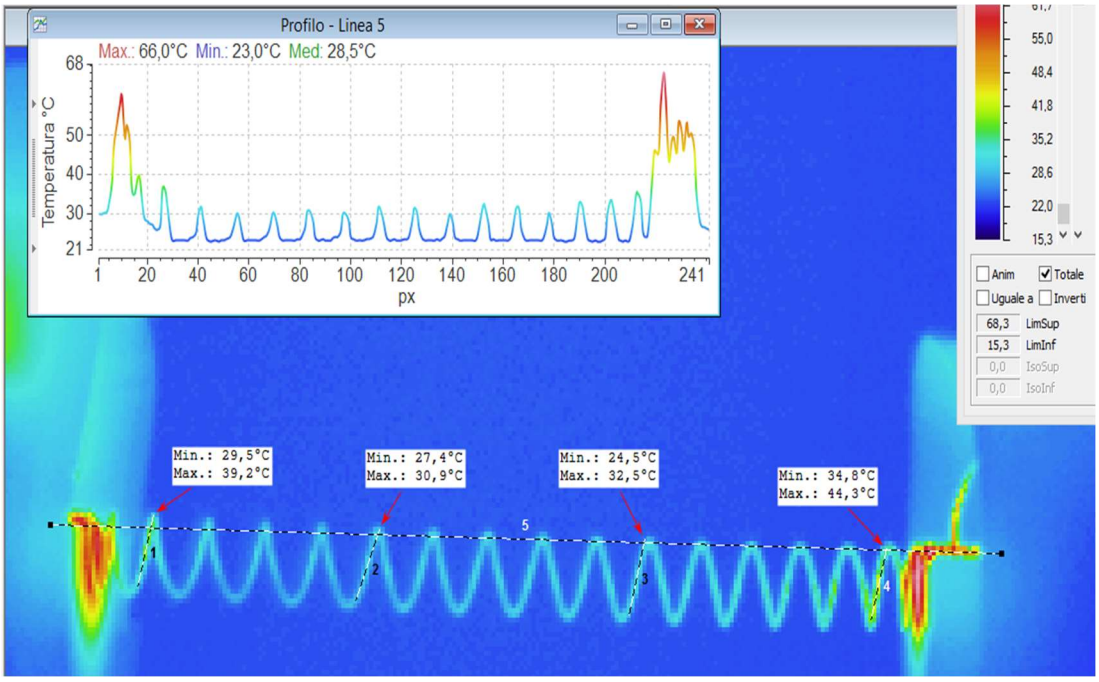

Fig. 104. Cooling of spring 5 in test 6

Line	T_{max} (°C)	*Emissivity*
1	66,5	0,74
2	60,6	0,74
3	62,2	0,74
4	62,5	0,74
5	96,5	0,74

Table 21. Temperature values for Fig. 103.

In this experiment and regarding Fig. 104. it can be pointed out that during the cooling, spring 5 is more uniform than spring 4. While in spring 4, most of the shape recovering was displaced to one side and on the opposite side there was a large strain; in spring 5 the coils are uniformly distributed along the whole length of the spring. This difference may be caused by the different heat treatments we used to shape both springs, since spring 4 was air cooled and spring 5 was cooled by water quenching. Hence, we can think that water quenching provides a more homogeneous microstructure of the material.

TEST 7:

Length (mm)	55,8
Current (A)	1,25
Voltage (V)	3,5

Maximum deformation, reached at t = 17 s: $17\ \mu\varepsilon$

Maximum force: $210{,}92\ g$

Cooling starts at t = 96 s

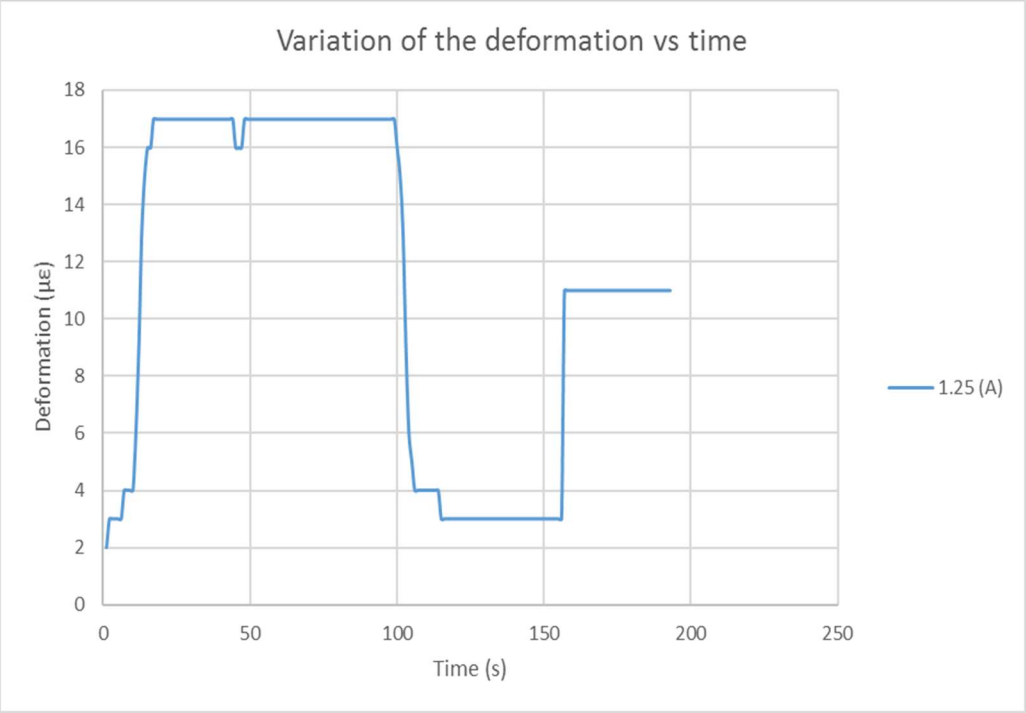

Fig. 105. Variation of the deformation with time for a constant current and elongation of spring 5, 1,25 A and 55,8 mm, respectively.

The results of this test are not consistent since the maximum deformation in notably lower that the deformation in test 1. In addition to this, there is an increase of the deformation at the end of the cooling process which has physical explanation. These effects can be due to the load cell not working properly. Therefore, this test will not be taken into account for futher analysis.

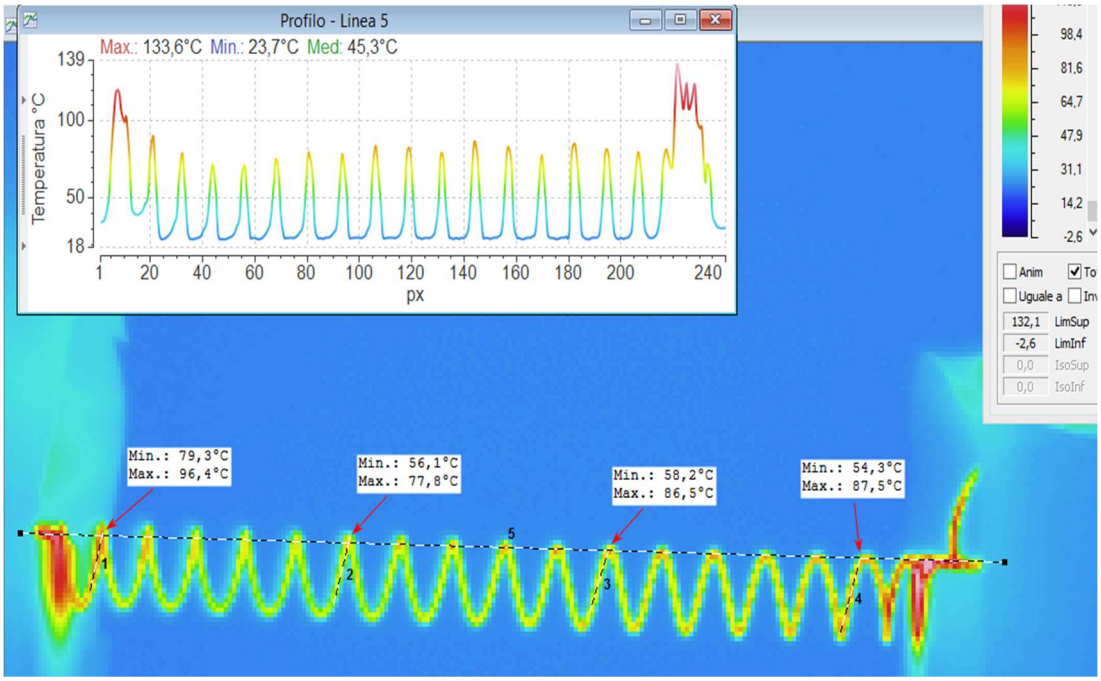

Fig. 106. Thermocamera image of test 7 when spring 5 is in complete austenitic state and at its maximum temperature

Line	T_{max} (°C)	*Emissivity*
1	96,4	0,74
2	77,8	0,74
3	86,5	0,74
4	87,5	0,74
5	133,6	0,74

Table 22. Temperature values for Fig. 106.

TEST 8:

Length (mm)	55,8
Current (A)	1,5
Voltage (V)	4,2

Maximum deformation, reached at t = 8 s: $25\ \mu\varepsilon$

Maximum force: $310{,}17\ g$

Cooling starts at t = 57 s

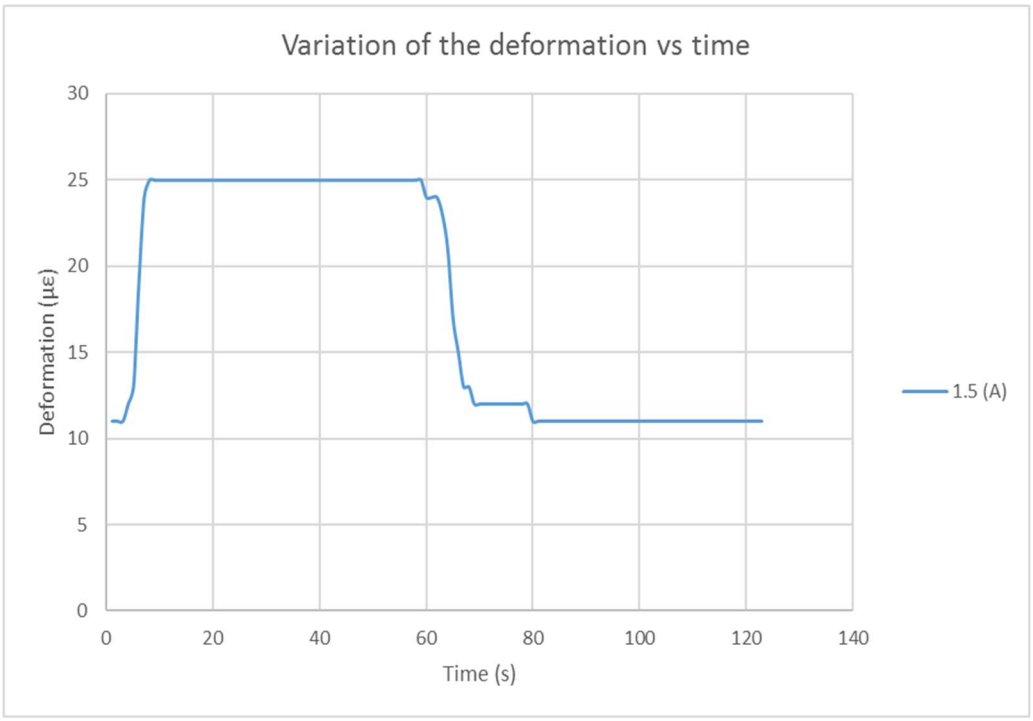

Fig. 107. Variation of the deformation with time for a constant current and elongation of spring 5, 1,5 A and 55,8 mm, respectively.

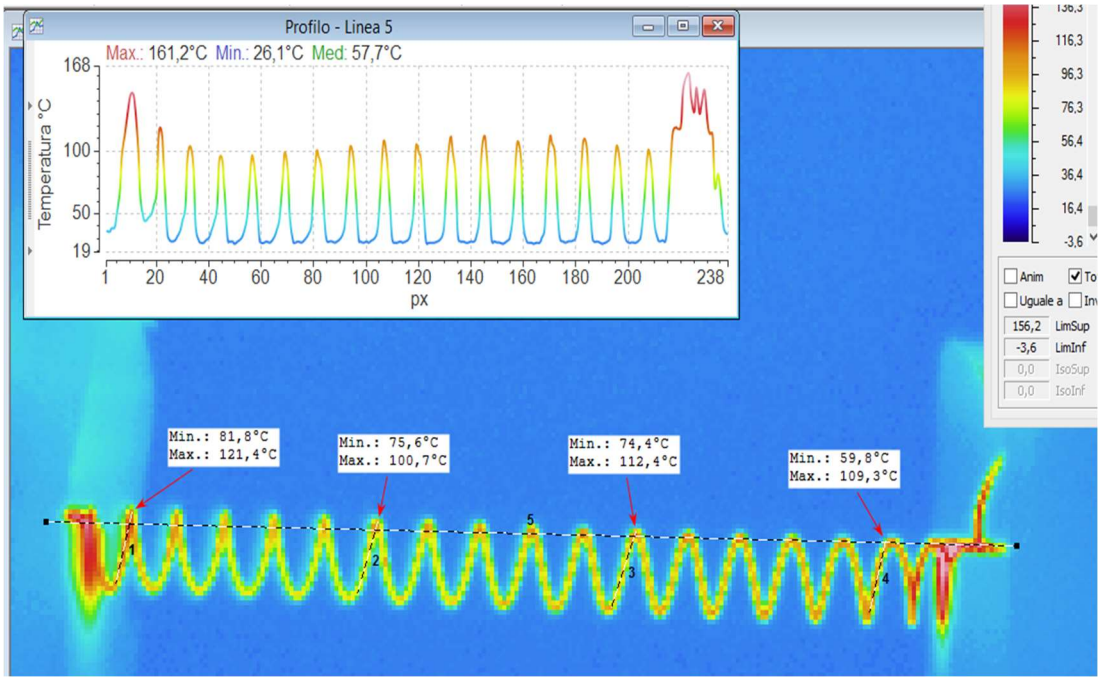

Fig. 108. Thermocamera image of test 8 when spring 5 is in complete austenitic state and at its maximum temperature

Line	T_{max} $(°C)$	*Emissivity*
1	121,4	0,74
2	100,7	0,74
3	112,4	0,74
4	109,3	0,74
5	161,2	0,74

Table 23. Temperature values for Fig. 107.

In the last tests, the temperature is significantly higher for line 5, which is located in the middle right end of the spring.

TEST 9:

Length (mm)	55,8
Current (A)	2
Voltage (V)	5,6

Maximum deformation, reached at t = 5 s: $20\ \mu\varepsilon$

Maximum force: $248{,}14\ g$

Cooling starts at t = 65 s

Fig. 109. Variation of the deformation with time for a constant current and elongation of spring 5, 2 A and 55,8 mm, respectively.

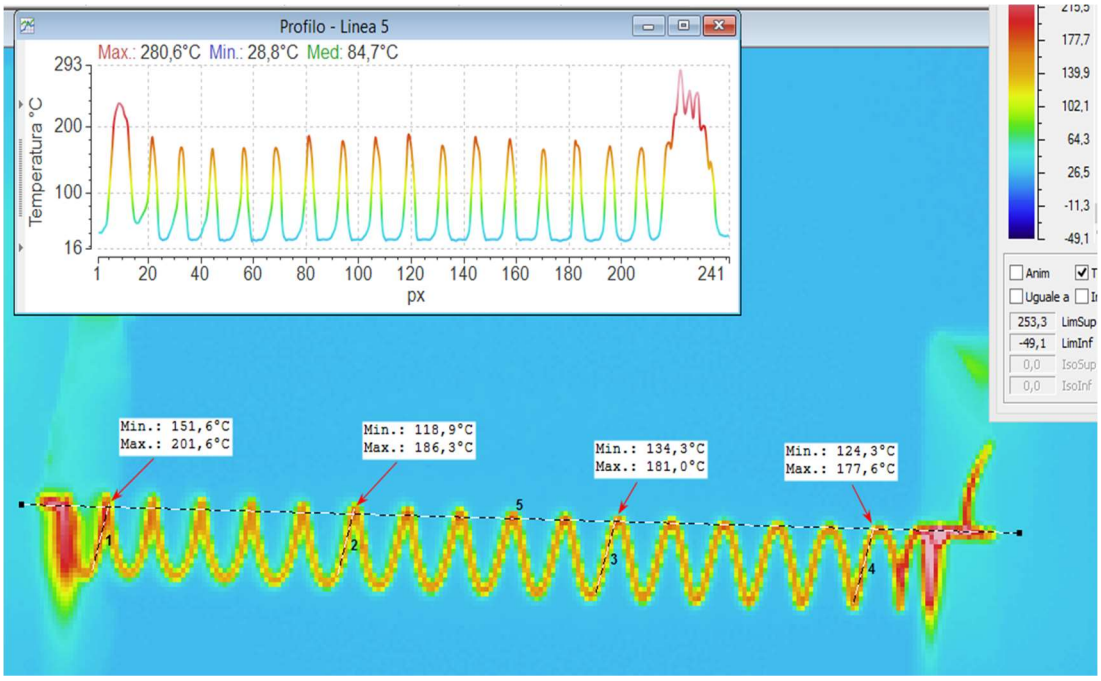

Fig. 110. Thermocamera image of test 9 when spring 5 is in complete austenitic state and at its maximum temperature

Line	T_{max} (°C)	*Emissivity*
1	201,6	0,74
2	186,3	0,74
3	181,0	0,74
4	177,6	0,74
5	280,6	0,74

Table 24. Temperature values for Fig. 109.

TEST 10:

Length (mm)	74,4
Current (A)	1
Voltage (V)	2,7

Maximum deformation, reached at t = 132 s: $16\ \mu\varepsilon$

Maximum force: $198{,}51\ g$

Cooling starts at t = 174 s

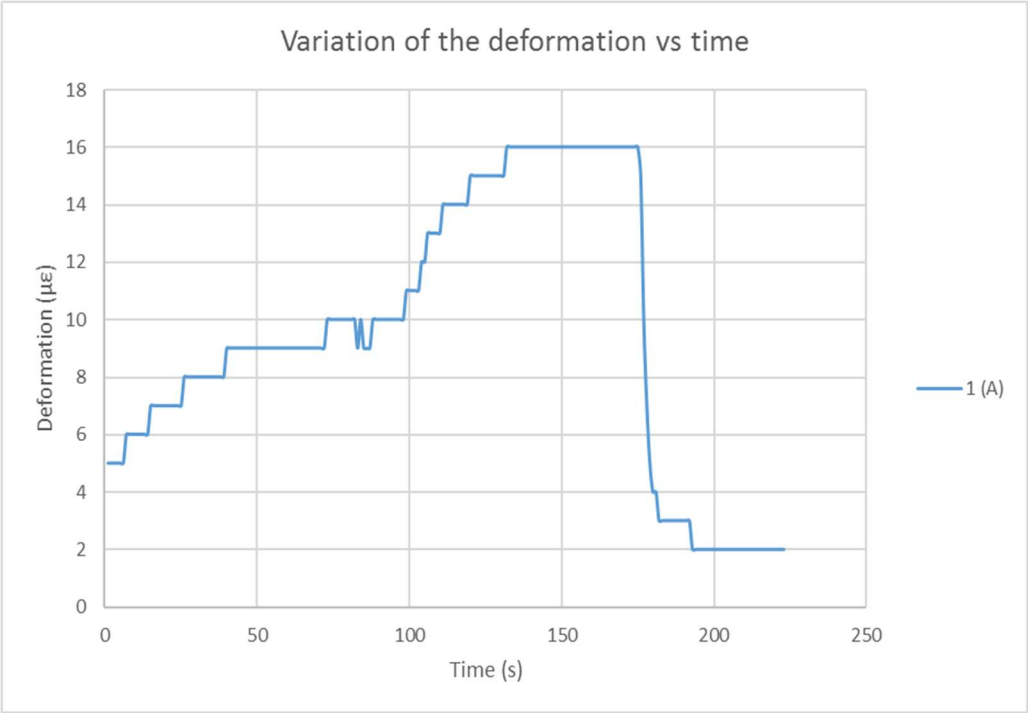

Fig. 111. Variation of the deformation with time for a constant current and elongation of spring 5, 1 A and 74,4 mm, respectively.

TEST 11:

Length (mm)	74,4
Current (A)	1,5
Voltage (V)	4,2

Maximum deformation, reached at t = 12 s: $26\ \mu\varepsilon$

Maximum force: $322{,}58\ g$

Cooling starts at t = 64 s

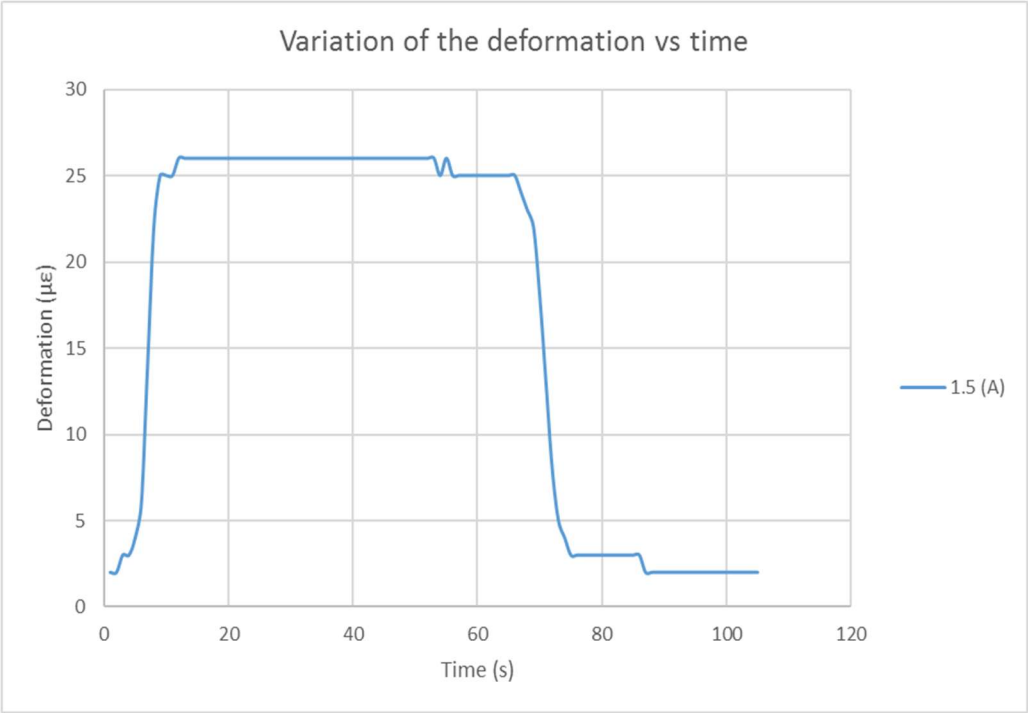

Fig. 112. Variation of the deformation with time for a constant current and elongation of spring 5, 1,5 A and 74,4 mm, respectively.

TEST 12:

Length (mm)	74,4
Current (A)	2
Voltage (V)	5,6

Maximum deformation, reached at t = 10 s: $25\ \mu\varepsilon$

Maximum force: $310{,}17\ g$

Cooling starts at t = 61 s

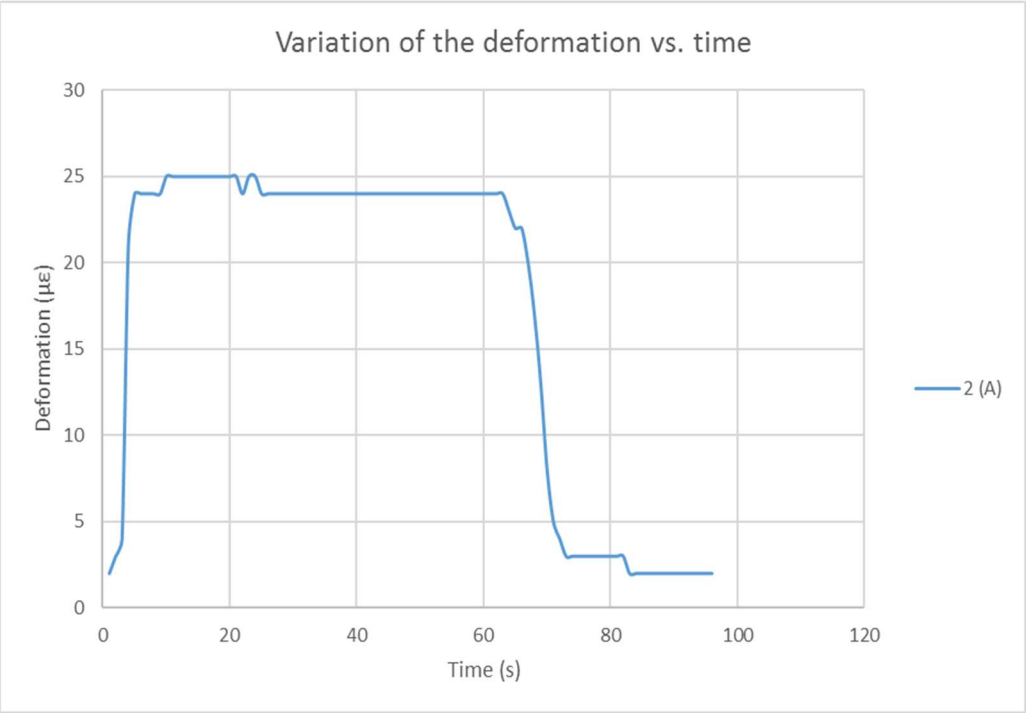

Fig. 113. Variation of the deformation with time for a constant current and elongation of spring 5, 2 A and 74,4 mm, respectively.

TEST 13:

As final test, we decided to prove how much current out set-up i sable to stand. To that aim, we increased the current from 2 to 3 A progresively. We could observe the melting of the teflon parts, since the temperature reached was much higher than the melting point of teflon (327˚C).

Length (mm)	74,4
Current (A)	2-3
Voltage (V)	5,6-9,1

Once it got to the maximum deformation, it started to decrease very fast due to the relaxation of the teflon.

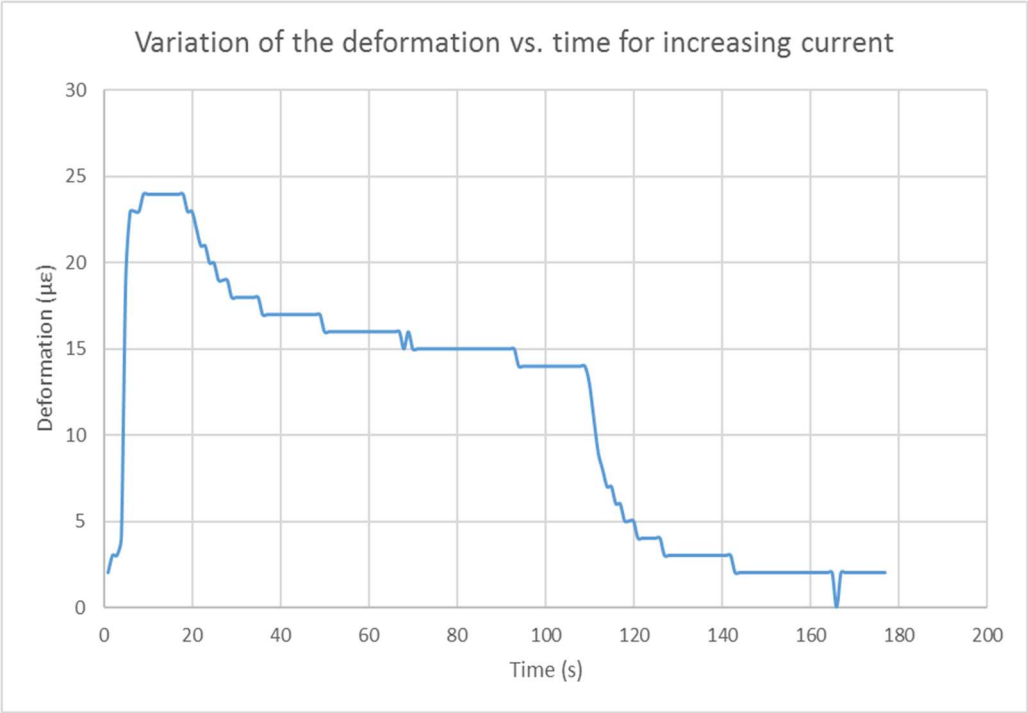

Fig. 114. Variation of the deformation with time for current progresively increased and at constant elongation of 74,4 mm.

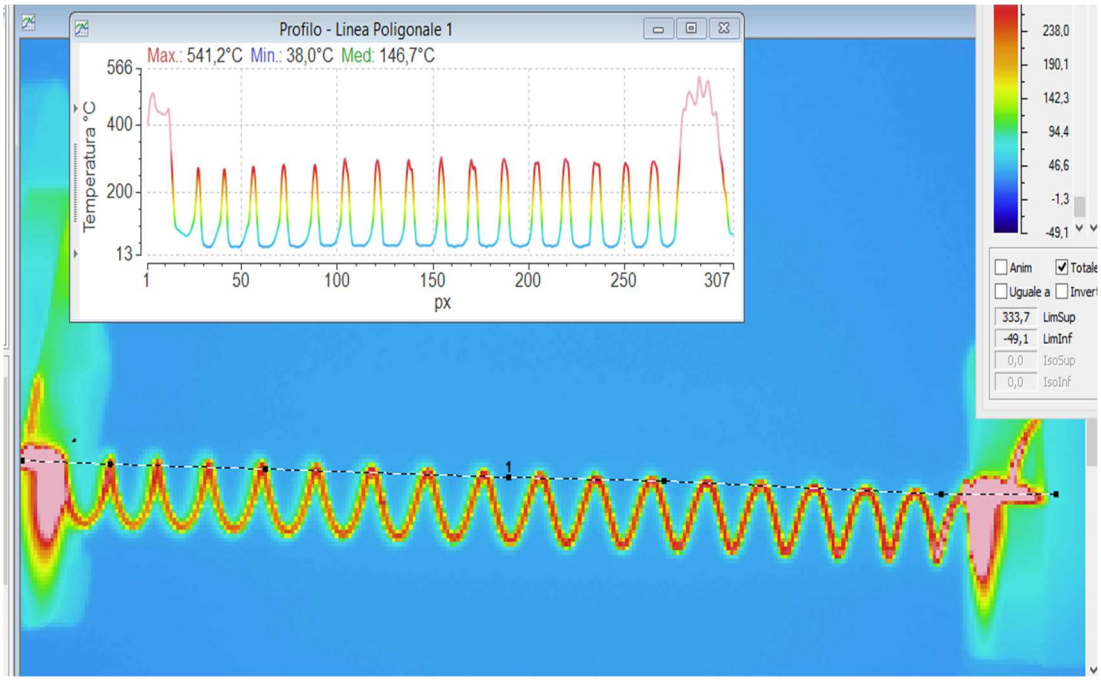

Fig. 115. Thermocamera image of test 13 when spring 5 is at a maximum temperature of 541,2˚C

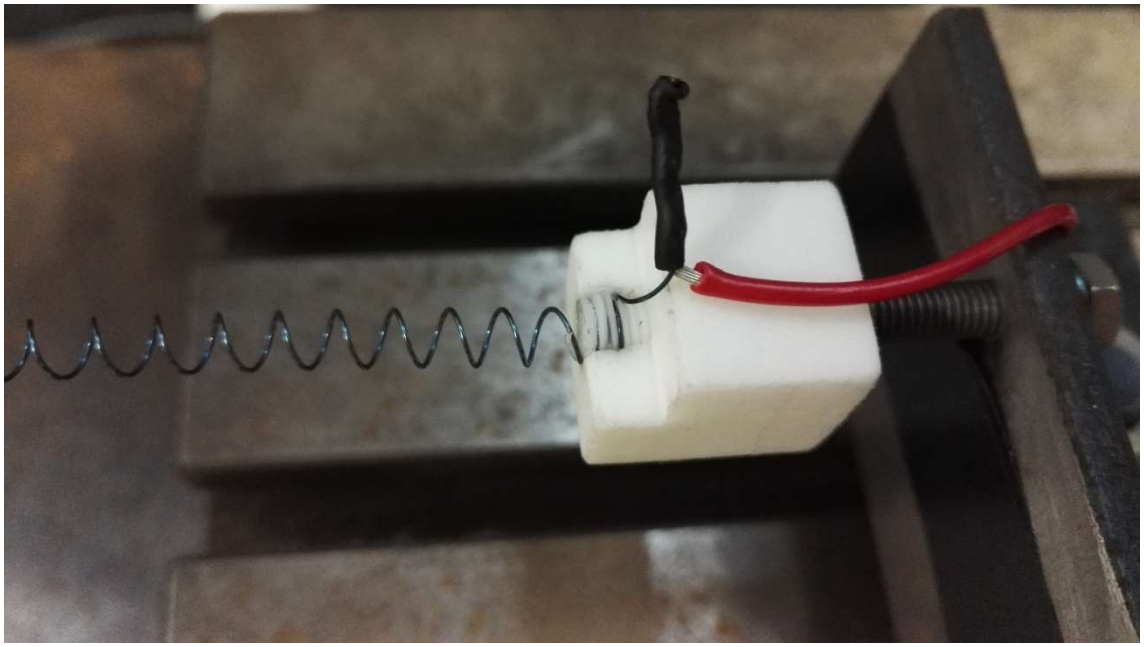

Fig. 116. Close-up of the melting of the clamping system during test 13

2.2.7 Conclusions of test 1 for spring 5

The results of test 1 with spring 5 are collected in the following graphs.

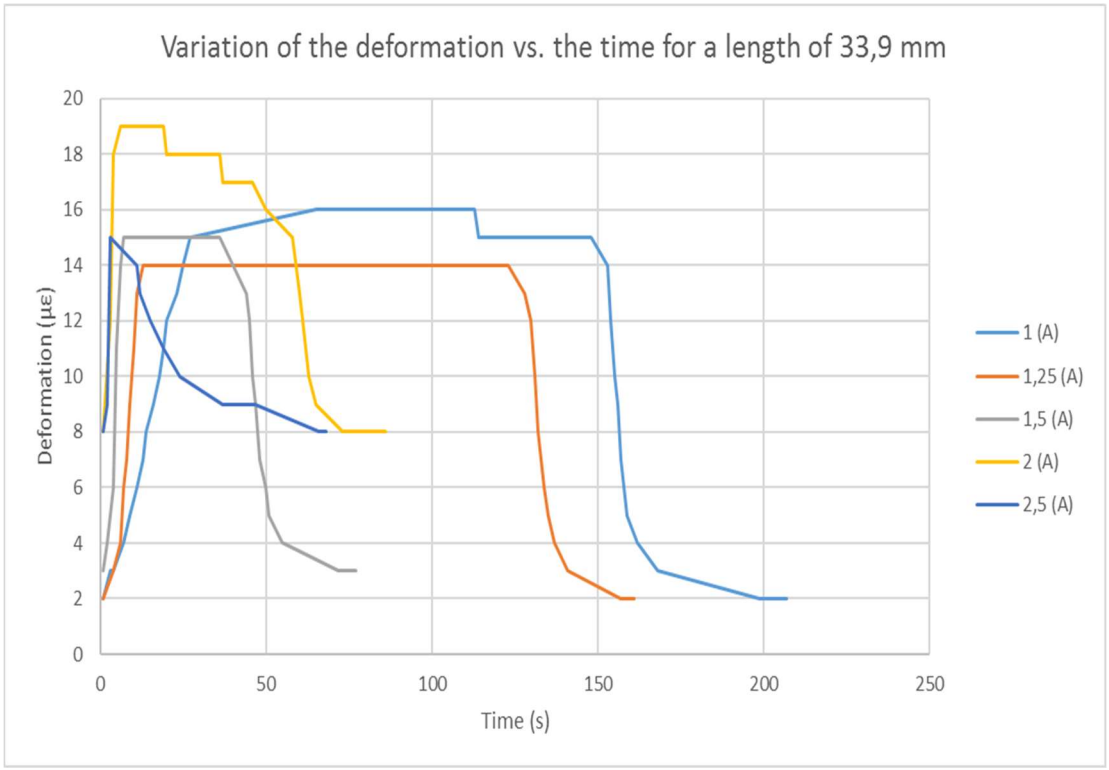

Fig. 117. Variation of the deformation in the load cell with the time for a length of spring 5 of 33,9 mm for different currents.

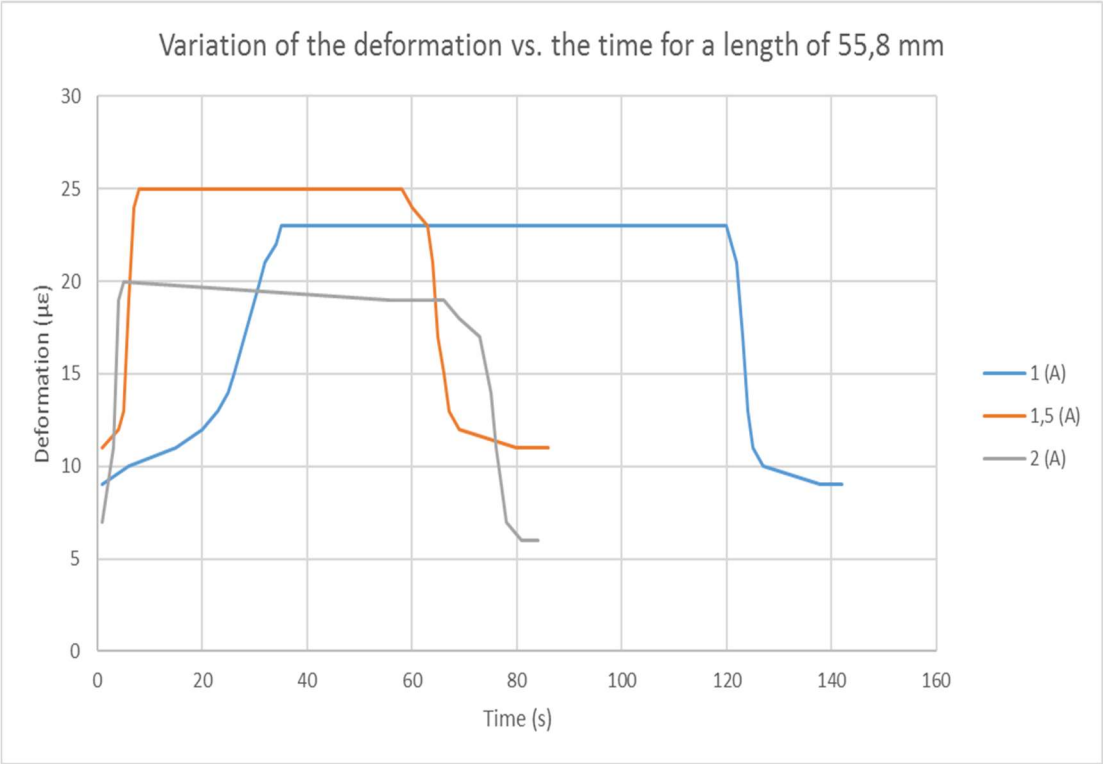

Fig. 118. Variation of the deformation in the load cell with the time for a length of spring 5 of 55,8 mm for diff

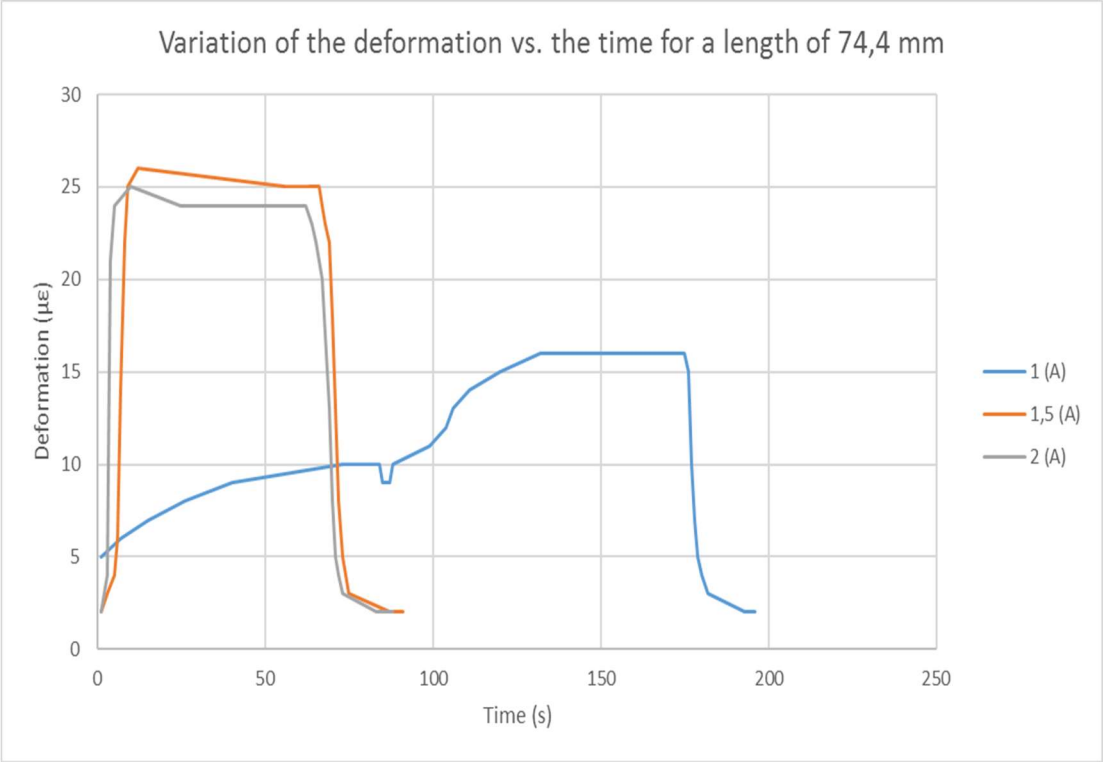

erent currents.

Fig. 119. Variation of the deformation in the load cell with the time for a length of spring 5 of 74,4 mm for different currents.

From the previous figures, we can affirm that the higher the current, the lower the time to reach the maximum deformation, as mentioned for spring 4. There exists, again, a significant difference between the actuation time for 1 A and the other levels of current, which confirms that 1 A is lower than the activation current. Concerning the maximum force, it remains moreless constant for the different values of the current, with the exception of 1 A because, since we do not achieve pure austenitic state, the maximum force cannot be reached. This fact can be clearly noticed in Fig. 119. For Figs. 117 and 118, 1 A gives lower forces but very high currents like 2 and 2,5 A do not allow the deformation of the load cell to achieve its maximum value since, as mentioned before, a relaxation of the teflon has occurred due to very high temperatures. The temperatures in the clamps reached around 331˚C, as seen in Fig. 101. Other inconsistent may be due to damage of the set-up due to the peak temperatures reached during the test with spring 4.

Another fact to point out is that the maximum force increases with the elongation of the spring. The highest forces are obtained for an elongation of 74,4 mm and the lowest for an elongation of 33,5 mm.

With regard to the transformation temperatures, if we consider as activation current 1,25 A, an estimation of the austenitic finish temperature for each of the elongations is: for the length of 33,9 mm, around 86˚C; and for the length of 55,8 mm, around 90˚C. Comparing this results with the stress-temperature diagram of the SmartFlex® wire, the levels of stress applied to the wire respectively are 120 MPa and 170 MPa.

CONCLUSIONS

With this study, we were able to test some of the principal thermomechanical properties of SMA spring actuators, in particular Nitinol springs. Concerning the reshaping of the SmartFlex® wire into a spring, different heat treatments and cooling processes were used. Evaluating the behavior of springs 4 and 5 during experimental test 1, it is noted that spring 5 shows a more uniform distriution of the spires when cooling, what means that it is microstructurally more homogeneous. Therefore, we can conclude that water quenching is a more convenient cooling process with respect to air cooling.

Another issue to remark is the clamping system. Since SMA actuators need to be heated to relatively high temperatures and this is made by means of making a current circulate through them, the clamping system used must be thermally and electrically insulated. These two properties can be achieve by high performance plastics like PEEK. Seeing that the temperatures our springs were going to reach do not exceed 200˚C, we decided to use PTFE (Teflon) as the material for our clamping system, which improved the system used in previous experiments. Another advantage of this clamping regards the fact that the spring is coiled around a bolt. Springs clamped by means of hooks have an irregular distribution of stresses and usually break, when subjected to relatively high level of stress, in the sections of the hooks. Coiling the spring around a more uniform distribution of the stress along it.

Concerning the results of test 0, the lack of accuracy and the possible inconsistency of some results may be due to human errors. Since we used a caliper to measure the different lengths throughout the SME process of our springs, due to the small size of the components, the measurements taken were not very precise.

With regard to test 1, the main issue with respect to the accuracy of the results is the shortage of precision of the load cell. It measures με and we had a maximum range in the deformation of 0-26 με. This is the reason for the graphical representations to show relatively rough steps.

Finally, with reference to the temperature distribution along the springs, the maximum values were registered in the ends. This fact causes that the clamping system is significantly affected by the temperature. This is the reason why, for very high currents and, consequently, very high temperatures close to the melting point of the teflon, the clamping system suffered from relaxation and the values recorded by the load cell were not representative.

REFERENCES

[1] Lagoudas, Dimitris C. *Shape Memory Alloys Modelling and Engineering Applications.* New York: Springer, 2008.

[2] Rao, Ashwin, Srinivasa, A. R. and Reddy, J. N. *Design of Shape Memory Alloy (SMA) Actuators.* Springer, 2008.

[3] Lecce, Leonardo and Concilio, Antonio. *Shape Memory Alloy Engineering for Aerospace, Structural and Biomedical Applications.* Elsevier, 2015.

[4] *Standard Terminology for Nickel-Titanium Shape Memory Alloys,* ASTM F2005-05, 2015.

[5] *Standard Test Method for Determination of Transformation Temperatures of Nickel-Titanium Shape Memory Alloys by Bend and Free Recovery,* ASTM F2082-15.

[6] *Standard Test Method for Tension Testing of Nickel-Titanium Superelastic Materials,* ASTM F2516-14.

[7] Antonucci, V., Faiella, G., Giordano, M., Mennella, F. and Nicolais, L. *Electrical resistivity study and characterization during NiTi phase transformations.* Napoli: Thermochimica Acta, 2007.

[8] Stroz, D., Bojarski, Z., Ilczuk, J., Lekston, Z. and Morawiec, H. *Effect of thermal cycling on as-quenched and aged nickel-rich Ni-Ti alloy.* Journal of Materials Science 26, 1991.

[9] Uchil, J., Mohanchandra, K. P., Ganesh Kumara, K. and Mahesh, K. K. *Study of critical dependence of stable phases in Nitinol on heat treatment using electrical resistivity probe.* Material Science & Engineering A251, 1998.

[10] Hartl, Darren John, Benafan, Othmane and Coda, Alberto. *Standardization of shape memory alloy test methods toward certification of aerospace applications.* Smart Materials and Structures, 2015.

[11] Mammano, G. Scirè and Dragoni, E. *Functional fatigue of Ni-Ti shape memory wires under various loading conditions.* International Journal of Fatigue 69, 2004.

[12] Mammano, G. Scirè and Dragoni, E. *Functional fatigue of shape memory wires under constant-stress and constant-strain loading conditions.* Procedia Engineering, 2011.

[13] Attanasi, Gabriele, Auricchio, Ferdinando and Urbano, Marco. *Theoretical and Experimental Investigation on SMA Superelastic Springs.* Journal of Materials Engineering and Performance, 2011.

[14] *Teflon PTFE Handbook.* Dupont

[15] Bellini, Alberto and Dragoni, Eugenio. *Mechatronic Design of a Shape Memory Alloy Actuator for Automotive Tumble Flaps: A Case Study.* IEEE Transactions on Industrial Electronics, 2009.

[16] Follador, Maurizio, Cianchetti, Matteo, Arienti, Andrea and Laschi, Cecilia. *A general method for the design and fabrication of shape memory alloy active spring actuators.* Smart Materials and Structures, 2012.

[17] *Standard Test Method for Transformation Temperature of Nickel-Titanium Alloys by Thermal Analysis,* ASTM F2004-05, 2010.

[18] *Standard Terminology for Nickel-Titanium Shape Memory Alloys,* F2005-05, 2015.

[19] Case, Lisa, Kreiner, Zachary, Redmond, John and Trease, Brian. *Shape Memory Alloy Shape Training Tutorial.* Smart Materials and Structures, 2004.

[20] Fernandes, F. M. Braz, Mahesh, K. K. and Andersan Dos Santos, Paula. *Thermomechanical Treatments for Ni-Ti Alloys.* Intech, 2013.

[21] Fumagalli, Luca and Coda, Alberto. *Smartflex NiTi Wires for Shape Memory Actuators.* Journal of Materials Engineering and Performance, 2008.

[22] Norwich, Dennis W. *A Comparison of Zero Mean Strain Rotating Bean Fatigue Test Methods for Nitinol Wire.*

[23] Norwich, Dennis W. and Fasching, Audrey. *A study of the effect of diameter on the fatigue properties of NiTi wire.*

[24] Polinsky, Mark A., Norwich, Dennis W. and Wu, Ming H. *A study of the effects of surface modifications and processing on the fatigue properties of NiTi wire.*